Correlating Structural and Optical Properties in Aromatic Semiconductor Crystals and Heterostructures

DISSERTATION

zur Erlangung des Doktorgrades
der Naturwissenschaften
(Dr. rer. nat.)

dem Fachbereich Physik
der Philipps-Universität Marburg

Philipps Universität Marburg

vorgelegt von

ANDRE RINN

aus

ESSEN

MARBURG, 2017

Vom Fachbereich Physik der Philipps-Universität Marburg
als Dissertation angenommen am: 12.09.2017
Erstgutachter: Prof. Dr. Sangam Chatterjee
Zweitgutachter: Prof. Dr. Gregor Witte
Tag der mündlichen Prüfung: 16.10.2017
Hochschulkennziffer: 1180

"*Science is like sex - sometimes something useful comes out, but that is not the reason why we are doing it.*"
-Richard Feynman

Im Gedenken an Hans Curt Rinn

Contents

List of Abbreviations

BBO barium borate

BDP 1,5-bis(dimethylamino)pentamethinium perchlorate

BSE Bethe-Salpeter equation

CCD charge-coupled device

CMOS complementary metal-oxide-semiconductor

CT charge-transfer

DFT density functional theory

FRET Förster resonance energy transfer

GW Greens function and screened Coulomb potential W approximation

HOMO highest occupied molecular orbital

IR infra-red

LED light-emitting diode

LUMO lowest unoccupied molecular orbital

LPB lower polariton branch

Nd:YAG neodymium-doped yttrium aluminium garnet

OPV organic photovoltaics

OLED organic light-emitting diode

PEN pentacene

PFP perfluoropentacene

PL photoluminescence

PLE photoluminescence excitation

SHG second harmonic generation

TDA Tamm-Dancoff approximation

Ti:Sa titanium-sapphire laser

TRPL time-resolved photoluminescence

UPB upper polariton branch

UPS ultraviolet photoemission spectroscopy

UV ultraviolet

VIS visible

1 Introduction

We live in a world completely dependent on the last 60 years of progress in semiconductor research and technology, pioneered by the invention of the first integrated circuit in 1964 [1]. The computer is indispensable for nearly every profession in the developed world and the revenue of the consumer electronics industry is comparable to the gross domestic product of a small country [2, 3]. Therefore, it is safe to assume that most readers, and this author, spend a great deal of their waking hours with a semiconductor device in hand. While computers and cellphones are the most common examples used in emphasizing the importance of semiconductor technology in every-day live, optoelectronic applications in light-emitting diode (LED) technology and photovoltaics gain increasing significance from year to year [4, 5]. The latter are of significant interest as fossil fuels become increasingly unsustainable and new and renewable energy sources are needed. Today's environmental and political realities impose new challenges on technology and science to increase the efficiency of light harvesting technology as a promising source of cheap and clean energy.

The majority of the technological revolutions of the 'computer age' are carried on the back of silicon-based inorganic semiconductors. Decades of research and technological advances have led to large-scale device production with exceptional quality and a far-reaching theoretical understanding of this material class [6, 7]. In contrast, the emerging organic semiconductor technology, like organic photovoltaics (OPV) and organic light-emitting diode (OLED), is still in its infancy. However, organic semiconductor devices have already found their way on the market, as the most recent generation of smart phones [8] and TV screens [9] are based on OLEDs. On one hand, organic semiconductors excel with their mechanical flexibility, low cost mass production by roll-to-roll printing, and versatile electronic properties due to the shear unlimited possibilities

of synthetic chemistry. On the other hand, the weaknesses of many organic materials, such as their long term stability and quantum efficiency, still form a significant barrier for the competitiveness of organic semiconductors, especially in the field of photovoltaics. Additionally, the theoretical understanding of molecular solids trails behind the inorganic theory by decades of research. Generally, the weak van-der-Waals interaction that hold organic crystals together renders a great part of theory used for predictive calculations of covalently bound inorganic semiconductors unsuitable. This is because inorganic semiconductor theory is based on the assumption of strong covalent or ionic bonds with binding energy orders of magnitude above any photon energies used in optical spectroscopy and comparatively weak phonon interactions. The electronic subsystem can be separated from the atomic cores in the so called Born-Oppenheimer approximation. This is not the case in organic solids: strong vibronic coupling and the relative weakness of the van-der-Waals interaction lead to a breakdown of the Born-Oppenheimer approximation. New complications for theoretical modeling arise in the organic case: atoms as the building blocks of inorganic crystals are themselves isotropic. Hence, all anisotropy introduced to the crystal stems from the crystalline structure. By contrast, molecules themselves are often anisotropic. Hence, anisotropy of molecular crystals can stem from the crystalline packing and the alignment of molecular dipoles within the crystal structure. This is especially important in heterostructures at the interface between two different types of molecules, where the interaction between both species strongly depends on the molecular alignment. As with most semiconductor devices, OLEDs and OPV where such a semiconductor heterojunction is the key component, making interfaces between two different organic molecules subject to immense research efforts [10, 11, 12]. In inorganic photovoltaics absorption of an inciting photon absorbed creates a pair of free carriers, a negatively charged electron in the conduction band, which leaves behind a postively charged hole in the valence band. Both quasiparticles can be guided by internal electric fields to the anode or cathode of the device contributing to the photocurrent. However, as excitonic binding energies are large in organic crystals, most absorbed photons will create electrically neutral free Frenkel excitons in organic solar cells, which do not dissociate into charge carriers at room temperature [13]. Although comprised of charged particles, the net-neutral exciton cannot be extracted, as they cannot be directed to the appropriate cathode/anode via internal electric fields, rendering them unsuitable for current generation. However,

excitons can dissociate at a donor-acceptor interface and therefore contribute to the photocurrent of the solar cell. So called charge-transfer (CT) excitons, where the electron and hole are spatially separated in the acceptor and donor material, respectively, have been shown to be an intermediate step for charge dissociation [14, 15]. The formation efficiency of such states is strongly dependent on the overlap of molecular orbitals at the heterointerface [16].

As previously mentioned, organic molecules often display great anisotropy. Aromatic molecules deserve a special mention here: their delocalized electron systems lead to extended π-orbitals perpendicular to the carbon ring and great charge mobilities in the perylene molecules themselves [17, 18]. Stacking such aromatic molecules face-to-face leads to a significant wavefunction overlap of the out of plane π-orbitals and therefore an increase in CT exciton formation effciency and performance of any conceivable device based on the heterojunction [19]. On the other hand, an edge-to-edge stacking at the interface has the opposite effect. Thus, the exact molecular alignment at the interface is of great interest for device performance and thus crucial for fabrication.

This thesis is dedicated to investigate the influence of the molecular packing of aromatic organic semiconductor crystals on their optoelectronic properties using the example of perylene as well as pentacene (PEN)/perfluoropentacene (PFP) heterostructures. Perylene is an ideal model system due to its strong light-matter interaction and exceptional achievable sample quality with molecularly smooth surfaces [20]. Different crystalline polymorphs are known for bulk crystals: the β-phase with a monomeric and the α-phase with a dimeric basis. At the same time, the molecule itself is relatively small and simple, allowing for theoretical modeling of the system. Therefore it offers a perfect platform for an in depth experiment-theory comparison. Our study on perylene aims to push the theoretical understanding of molecular crystals and correlate these findings directly to their molecular packing by comparing the results for both crystalline phases. To investigate the impact of molecular packing at an organic-organic heterointerface the model system of PEN/PFP will be employed. Both constituents are structurally virtually identical, enabling incorporation in well defined heterostructures. Besides easy structural incorporation, the immense electronegativity of fluorine renders PFP a good, structurally compatible electron acceptor when paired with PEN, which acts as an electron donor [21]. An inverse quadrupole moment of both molecules increases their intermolecular interaction beyond simple van-der-Waals attraction [22]. Thus CT

excitons are formed between neighboring PEN and PFP molecules at the interface of the heterostructure [23]. The actual coupling strength between both molecules depends on their relative molecular alignment. As a consequence, the formation efficiency of any possible interfacial state is strongly influenced by the molecular packing at the PEN/PFP junction.

By exploiting templating effects of the substrate and previously deposited layers [24], well defined crystalline layers of both PEN and PFP can be grown with different molecular alignment with regard to the substrate. Overgrowing those samples with the other molecular species yields an edge to edge or face to face alignment of the molecules at the interface, depending on the initial molecular layer. As face to face aliment will lead to overlapping π-orbitals, a significant difference between both alignments is expected. Both layered heterostacks (edge-on and face-on) are compared to an intermixed PEN/PFP sample, grown by co-evaporation of PEN and PFP at an 1:1 ratio. The resulting crystals exhibit a herring-bone structure where every molecule is neighbored by a molecule of the respective other species. The dynamics of all excitonic species observable in all three samples and the excitation channels of the resulting interfacial exciton state will be investigated. The latter reveals significant deviations from the commonly applied picture of a simple CT exciton with an electron in the PFP and a hole in the PEN layer, respectively.

To lay the theoretical foundation, Chap. 2 will introduce the formation of molecular orbitals and light matter interactions in molecules and molecular solids. All relevant quanta of excitation, as different exciton species and polaritons in the limit of strong light-matter coupling will be discussed. Chapter 3 will introduce the different experiments used to obtain the results discussed in Chap. 4. Finishing this work, Chap. 5 will summarize all results and highlight their contribution to the field and arising questions yet to be answered.

2 Theoretical Background

The main scope of this thesis is to investigate the light-matter interaction in different aromatic molecular crystals and their heterostructures. The particular aim of this chapter is to give a brief yet comprehensive introduction to the topic in a bottom up approach: the first section will deal with the electronic orbitals of a single molecule. The simplest case, the H_2^+, will be used as a simplified example to demonstrate how molecular orbits form from a linear combination of atomic orbitals. The more complex case of fully conjugated carbon rings, the basic building block of aromatic molecules, will be discussed subsequently. The focus will be on the delocalized π-orbitals and their relevance for intermolecular coupling in molecular crystals.
Light-matter interaction will be introduced in the framework of a straight-forward oscillator model. This concept will serve as the basis for the description of light absorption and emission by molecules. Subsequently, vibrational coupling will be discussed. Moving from single molecules to molecular solids, we will introduce the concept of excitons. Besides the most common case for organic crystals, the Frenkel exciton, the discussion will encompass CT-excitons, both intrinsic and across heterointerfaces, self-trapped excitons and excimers. Both singlet and triplet states will be reviewed with a short discussion of intersystem crossing. The chapter will end with a short section on light-matter interaction in the strong coupling limit, which will cover exciton-polaritons and the relevant polaritonic effects observable in latter chapters of this thesis. As more than an introduction is beyond the scope of this work, the interested reader is referred to one of the many available textbooks on the issue [25, 26, 27, 28, 29], on which most of this chapter is based on.

2.1 Electronic States in Single Molecules

In inorganic semiconductors, strong covalent or ionic coupling between the atomic constituents of the crystal fundamentally alters the electronic states of the system with respect to the isolated atom. The periodic rigid crystal lattice of tightly bound atoms leads to the introduction of new symmetries to the system and therefore to the lifting of the k-degeneracy. A band structure forms. Lattice vibrations further complicate the optical properties of the material due to phonon interaction. Essentially, all previous knowledge of the isolated single atom completely loses its relevance when studying the properties of the solid.

This is not necessarily true for organic solids. While strictly speaking there is no qualitative difference between inorganic and organic solids, the magnitude of the effects are dependent on the intermolecular coupling strength. Organic solids consist of covalently bound molecules interconnected by the relatively weak van-der-Waals interaction. In the limit of vanishing intermolecular interaction, the spectra of the organic solid reproduce the spectrum of a single molecule. Thus, the formation of energy bands from the distinct molecular orbitals leads to narrow almost dispersionless bands. As another consequence of weak intermolecular interaction, the influence of lattice vibrations on the optical spectrum of molecular solids is greatly diminished. On the other hand, intramolecular vibrons play an important role, as strong covalent bonds within the molecules increase their energy and intensity.

In a crude approximation, organic solids can be thought of as an oriented gas of molecules. The single-molecular properties remain as a useful first order approximation for the properties of the organic crystal [30, 31]. Of course, this is an oversimplification. Even within the oriented gas approximation, molecular anisotropy is introduced as a deviation from the properties of randomly oriented non-interacting molecules. In reality, dispersion and phonons in organic solids exist: different stacking motives of the same molecule can lead to noticeable deviation from single molecular properties due to enhanced intermolecular interaction resulting from polar bonds or π-stacking. The later will be discussed in Section 2.1.2. Even within the same crystal, anisotropy can lead to noticeable variations in bandwidth along different crystalline axis. However, the usefulness of single molecular considerations as a first-order approximation is evident

from the widespread misuse of technical expression from molecular physics in the context of organic solids: the conduction and valence bands are commonly referred to as lowest unoccupied molecular orbital (LUMO) and highest occupied molecular orbital (HOMO) respectively, even though these terms technically lose their relevance once crystals are considered, as the introduction of crystalline symmetry replaces distinct molecular orbitals with the band-structure of the respective crystal.
In this section, the formation of molecular orbitals will be explained using the H_2^+ molecule as a simple example. Since this work presents results on aromatic molecular crystals, we will expand this knowledge with a brief discussion of aromatic molecules.

2.1.1 The Ionized Hydrogen Molecule

Molecular orbitals will be discussed using the simplest possible case, the H_2^+ molecule. While the simplicity of the system enables a close look at the mechanisms behind molecular bindings, even in this one-electron molecule, a completely analytic solution does not exist. The starting point is the Schrödinger equation for the electron of a hydrogen atom

$$\left(-\frac{\hbar^2}{2m_0}\nabla - \frac{e^2}{4\pi\varepsilon_0 r}\right)\varphi(r) = E^0\varphi(r). \tag{2.1}$$

The solution of $\varphi(r)$ is known to be given by the Laguerre polynomials and spherical harmonics. Bringing a second proton in the vicinity of the hydrogen atom, the electron will feel the attraction of the second proton, introducing new Coulomb terms to Eq. 2.1. With the introduction of r_a and r_b as the distance between the single electron and the proton a and b, respectively and R_{ab} as the distance between the proton of each hydrogen atom, the resulting equation is

$$\left(-\frac{\hbar^2}{2m_0}\nabla - \frac{e^2}{4\pi\varepsilon_0 r_a} - \frac{e^2}{4\pi\varepsilon_0 r_b} + \frac{e^2}{4\pi\varepsilon_0 R_{ab}}\right)\Psi = E\Psi. \tag{2.2}$$

The fourth term on the left hand side describes the energy contribution due to the proton proton interaction of both atoms. As it simply introduces an energy offset to

the electronic system, it disregarded at this time. The ansatz $\Psi = a\varphi_a + b\varphi_b$ is used, a linear combination of the solutions for the hydrogen problem for protons a and b. Inserting this into Eq. 2.2 and subtracting the right hand side yields

$$\left(\Delta E - \frac{e^2}{4\pi\varepsilon_0 r_b}\right) a\varphi(r_a) + \left(\Delta E - \frac{e^2}{4\pi\varepsilon_0 r_a}\right) b\varphi(r_b) = 0. \tag{2.3}$$

Here, $\Delta E = E^0 - E$ refers to the difference of the hydrogen and H_2^+ energy eigenvalues.

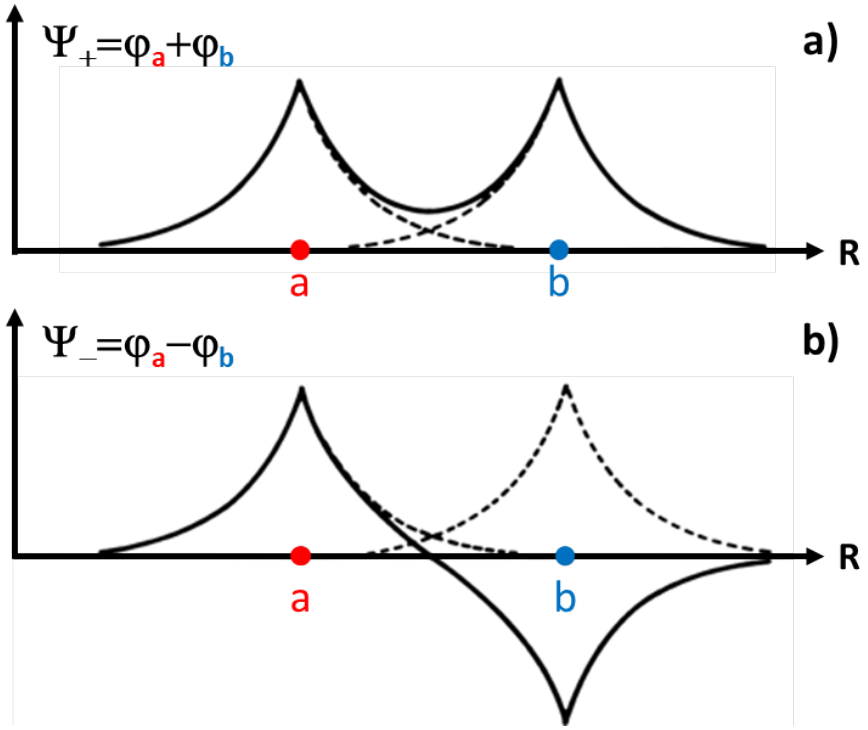

Figure 2.1: The symmetric (a) and antisymmetric (b) electron wavefunction of the H_2^+ molecule. The wavefunction of the isolated hydrogen atoms corresponding to the two protons at position a and b, respectively, are given by the dashed lines. The symmetric wavefunction increases the probability of finding an electron between the two protons, while the antisymmetric one decreases the chance. The former case energetically lowers the total energy due to the presence of the second proton at position b, while the total energy is increased by the second proton in the latter case. After [28].

In order to find an approximated solution to this equation, we treat the electron of the H_2^+ molecule as quasi bound to one of the two protons with the second proton as a slight perturbation to the system. As known from degenerate perturbation theory, multiplying

the equation by both φ_a and φ_b and integrating over the whole volume yields the two equations:

$$\begin{aligned}(\Delta E - A)a + (\Delta E \cdot S - B)b = 0\\ (\Delta E \cdot S - B)a + (\Delta E - A)b = 0,\end{aligned} \tag{2.4}$$

where the abbreviations

$$S = \int \varphi_a \varphi_b \mathrm{d}V, \tag{2.5}$$

$$A = \int \varphi_a \left(-\frac{\mathrm{e}^2}{4\pi\varepsilon_0 r_b}\right) \varphi_a \mathrm{d}V; \qquad B = \int \varphi_b \left(-\frac{\mathrm{e}^2}{4\pi\varepsilon_0 r_a}\right) \varphi_a \mathrm{d}V \tag{2.6}$$

have been made. Both parts of Eq. 2.6 have the form of diagonal and off-diagonal matrix elements. For physical interpretation, one finds A to resemble a charge density $-\mathrm{e}\varphi_a^2$ of an electron bound to the proton a and how it interacts with the potential $\left(-\frac{\mathrm{e}}{4\pi\varepsilon_0 r_b}\right)$ of proton b. B, the so-called exchange integral, has no direct relation to classical physics and is the result of quantum mechanics. It relates to an electron in a superposition of the states φ_a and φ_b. One could speak of an electron exchanged between both states, hence the name.

Equation 2.4 represents a set of algebraic equations for the unknown coefficients a and b. It can only have a none-trivial solution if its determinant vanishes, which leaves us with the condition:

$$(\Delta E - A) = \pm(\Delta E \cdot S - B). \tag{2.7}$$

If we insert this relation back into Eq. 2.4, we obtain $a = \pm b$ and the final result:

$$\Psi_\pm = a(\varphi_a \pm \varphi_b), \tag{2.8}$$

$\Psi_\pm$ are the symmetric and antisymmetric wavefunctions of the H_2^+ molecule as visualized in Fig. 2.1. The magnitude of the parameter a now has to be obtained by normalization within the boundary condition of the system. The total energy of the

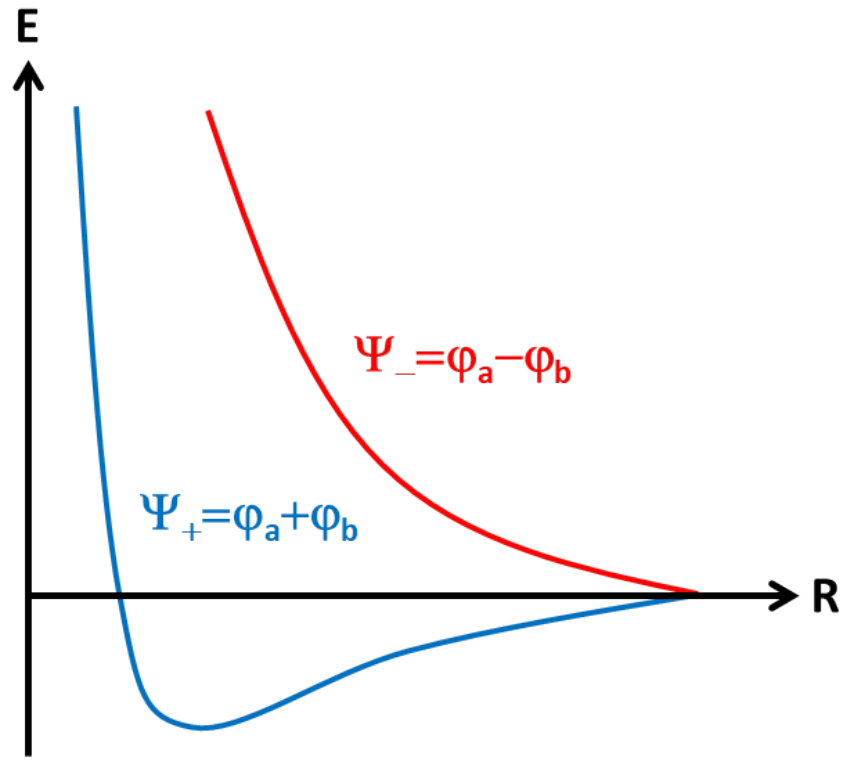

Figure 2.2: The total energy of the symmetric and antisymmetric electron wavefunction of the H_2^+ molecule in dependence of the proton-proton distance R_{ab}. While the symmetric case shows a region of R_{ab} that pushes the total energy below zero and therefore favors the formation of a molecular orbital over isolated hydrogen atoms, the anti-symmetric case is positive for every value of R_{ab}. This is why the symmetric wavefunction is called the bonding orbital, while the antisymmetric wavefunction is called the antibonding molecular orbital. Figure after [28].

system is retrieved from Eq. 2.2, now including the energy from the proton-proton interaction:

$$E_{\pm} = E_0 + \frac{A \pm B}{1 \pm S} + \frac{e^2}{4\pi\varepsilon_0 R_{ab}}. \tag{2.9}$$

The last two terms in this equation correspond to the binding energy of the system. If it has a negative value, the molecule is stable. One can numerically evaluate the binding energy of both wavefunctions. Neither S nor A in Eq. 2.9 can decrease the total energy of the system to reach stable molecular orbitals. The deciding parameter is B, which is

related to the exchange energy of the electron in Eq. 2.6. The results are presented in Fig. 2.2, where the total energy of the molecule is given in dependence of the distance R_{ab} between the two protons. The total energy of the antisymmetric wavefunction never falls below zero. The energy for the antisymmetric wavefunction of the H_2^+ molecule is less favorable in energy for all values of R_{ab} when compared to the energy of the isolated hydrogen atom. As a result, a bond between the two protons will not occur; this orbital is called an anti-bonding orbital. On the other hand, there is a region in the phase space of the symmetric wavefunction where the total energy is negative allowing a stable molecule to form. This orbital is called a bonding molecular orbital.
It is important to note that these results are obtained by treating the second proton as a small perturbation to the isolated hydrogen atom. While reproducing the physics of the system, this description does not provide the correct quantitative values. The binding energy of the bonding orbital is underestimated by close to 1 eV. This example shows that an analytical description of even the simplest molecule requires certain approximations and as such is an imperfect model for the real world interaction. For an exact description of the H_2^+ molecule, numerical methods have to be taken into consideration. While imperfect, this model provides us with a road-map for the construction of molecular orbitals: start with the atomic states of the contributing electrons, use linear combinations of these single particle wavefunctions to construct new molecular wavefunctions (in a way that all symmetry requirements caused by, *e.g.*, Pauli blocking are satisfied) and add corrections to the hamiltonian to account for many-body interactions.

2.1.2 Hybrid Orbitals in Carbon Rings

With regards to its relevance to this work, we will take a look at the binding properties of the carbon atom. As a general rule, only valence electrons contribute to an actual molecular binding. Carbon has four valance electrons. In the groundstate, two of them fill the $2s$ state, while the remaining two fill two of the three $2p$ states: $2p_x$, $2p_x$, and $2p_z$. The exact intermixture of these four different states differ depending on the molecule formed: for a stable molecule the adopted molecular orbitals should be in a minimum of total energy which is always dependent on the full molecular system. For methane

(CH_4), all four states form new bonding molecular orbitals. These molecular orbitals Ψ_{1-4} are constructed from the atomic orbitals φ_x, which correspond to the electron wavefunction in the state x:

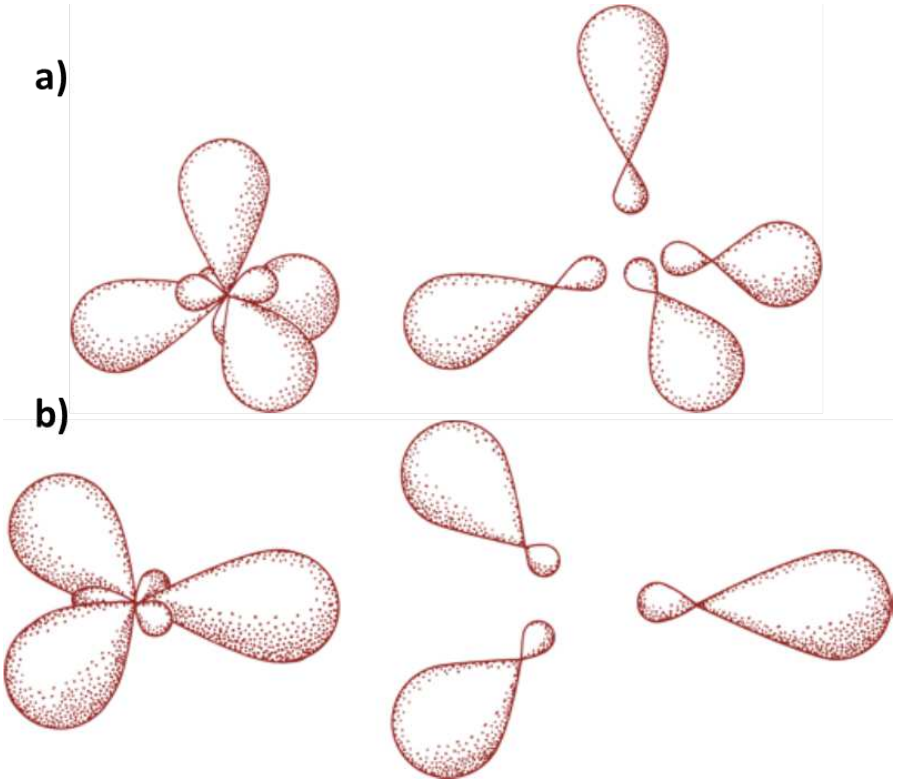

Figure 2.3: The electron densities for the tetragonal sp^3 hybridized molecular orbitals (a) and the planar trigonal sp^2 hybridized molecular orbitals (b). The right side shows a separated depiction of all individual contributing orbitals. Figure after Ref. [28].

$$\begin{aligned}
\Psi_1 &= \frac{1}{2}(\varphi_{2s} + \varphi_{2p_x} + \varphi_{2p_y} + \varphi_{2p_x}) \\
\Psi_2 &= \frac{1}{2}(\varphi_{2s} + \varphi_{2p_x} - \varphi_{2p_y} - \varphi_{2p_x}) \\
\Psi_3 &= \frac{1}{2}(\varphi_{2s} - \varphi_{2p_x} + \varphi_{2p_y} - \varphi_{2p_x}) \\
\Psi_4 &= \frac{1}{2}(\varphi_{2s} - \varphi_{2p_x} - \varphi_{2p_y} + \varphi_{2p_x}),
\end{aligned} \tag{2.10}$$

where φ_x symbolizes the electronic wavefunction in the corresponding state x. These four states are constructed from three p and one s-orbital, hence they are called sp^3

hybrids. Together, these four states form a tetragonal configuration where a hydrogen atom forms a bond to one of the four states at every corner to form the methane molecule in a σ-bond (see Fig. 2.3a). These σ-bonds, defined as symmetric for rotations along the bonding axis, are among the strongest kind of covalent bond.
A different configuration is found in aromatic molecules like benzene, in which six carbon atoms form a planar hexagon typically called a carbon ring. The carbon orbitals form a planar trigonal shape, a sp^2 hybridization as depicted in Fig. 2.3b. However, this leaves the p_z orbitals on the sidelines not contributing to the carbon-carbon σ-bonds. These atomic p-orbitals are aligned perpendicular to the plane of the carbon ring. The proximity of these six p-orbitals leads to a new kind of carbon-carbon bond in which the individual p-electrons couple and form a delocalized π-electron system (see Fig. 2.4). The delocalized nature of this electron system is a major contributor to the high carrier mobility of aromatic molecular solids. Since these orbitals extend beyond the plane of the molecule, they can overlap and interact with a π-electron system of a neighboring molecule, especially within a tightly packed molecular solid, with favorable molecular alignment. The influence of such a π-π stacking on the optoelectronic properties of aromatic molecular crystals will be the addressed in the investigation of perylene crystals in two different configurations and across the PEN/PFP interface. In contrast to inorganic

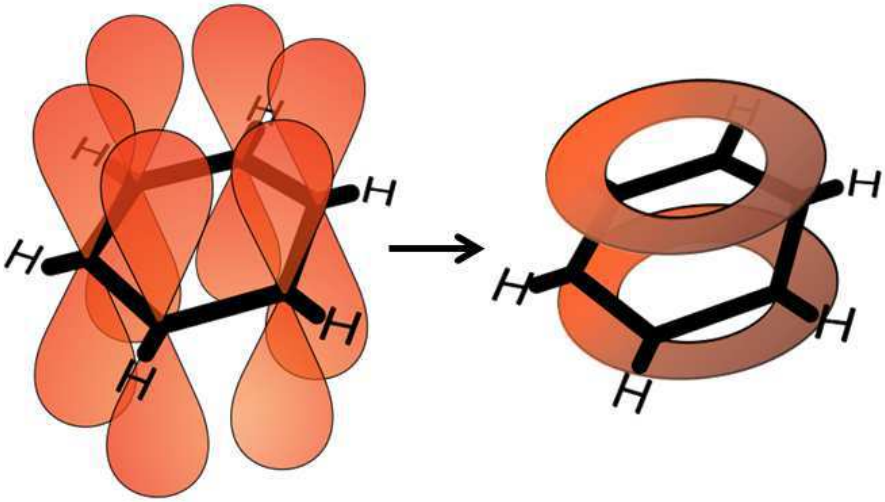

Figure 2.4: Formation of a π-electron system from the six individual p_z orbitals not contributing to the in plane sp^2 hybrids. Taken from [32].

solids, the individual states of the crystals constituents are still intact in molecular

crystals due to weak intermolecular coupling. While the basic optical excitations in these systems are excitons, they are linked to the molecular levels described in this chapter by their excitonic binding energy. The HOMO and LUMO are of special interest, as they dictate the basic properties of the lowest lying optical transitions. As π-bonds are weaker than σ-bonds, electrons contributing to the later occupy lower-energy states than electrons contributing to the former. This makes the π-orbitals (bonding) orbitals the HOMO and the π^*-orbitals (antibonding) the LUMO in aromatic molecular systems. This will become especially relevant as we talk about optical transitions and exciton formation. Note that our current description ignores the spin states of the involved electrons. Considering spins and the fermionic nature of electrons will lead to singlet and triplet orbitals, which will be discussed in Section 2.2.6.

2.2 Light-Matter Interaction in Molecular Crystals

This section covers the basics of light-matter interaction in molecules and organic semiconductors. The first part will provide a short introduction to general light-matter interaction, introducing the dielectric function and discussing how optical properties like absorption and reflection can be derived from it. This discussion will be focused on the single molecular case and will address vibronic coupling. Following this Coulomb interactions in a molecular crystal will be considered in the bounds of weak intermolecular coupling, leading to Frenkel excitons as the fundamental quasiparticles of electronic excitation [33, 34]. This discussion will be extended to more delocalized excited states: namely CT-excitons and excimers. The former are of specific interest as precursors for charge-separation at donor-acceptor heterointerfaces in OPVs [35, 14, 36, 37, 38, 39]. The influence of the optically inactive triplet exciton states on the dynamics of the bright singlet states will be then reviewed. A closer look at the propagation of light through solids with strong light-matter interaction will lead to the concept of polaritons, a mixed state of photons and crystal excitation. Since this thesis focuses on experiments with photon energies in the visible and near ultraviolet (UV) range, optical effects in the infra-red (IR) or deep UV/X-ray range will not be discussed here. The reader is referred to many of the available textbooks and review articles on these topics for further information, *e.g.*, [25, 26, 27, 28, 29, 40, 41, 14].

2.2.1 The Optical Susceptibility: The Oscillator Model

The polarization $\mathscr{P}$ induced by an inciting light field in a dielectric medium is the basic source of light-matter interaction. Defined as induced dipole moments P per volume $V = L^3$ we can write $\mathscr{P}$ for an electric field in x direction

$$\mathscr{P} = \frac{P}{V} = n_0 \mathrm{e} x = n_0 d \tag{2.11}$$

where $d = \mathrm{e}x$ is the electric dipole moment of an electron displaced by the distance x and n_0 is the electron density per unit volume. To calculate the displacement x of an electron from its equilibrium position by a monochromatic light field $E(t) = E(\omega)\mathrm{e}^{-\mathrm{i}\omega t}$ we solve the equation of motion for a set of damped driven oscillators

$$m_0 \frac{\mathrm{d}^2 x}{\mathrm{d}t^2} = -m_0 \gamma \frac{\mathrm{d}x}{\mathrm{d}t} - m_0 \omega_0^2 x + \mathrm{e}E(t) \tag{2.12}$$

where γ is introduced as a heuristic damping constant along with m_0 and ω_0 as the electron mass and resonance frequency of the oscillator, respectively. Equation 2.12 is solved with the ansatz $x(t) = x(\omega)\mathrm{e}^{-\mathrm{i}\omega t}$. In combination with Eq. 2.11 this yields the fundamental relation

$$\mathscr{P}(\omega) = \frac{n_0 \mathrm{e}^2}{m_0} \left(\frac{1}{\omega_0^2 - \omega^2 - \mathrm{i}\gamma\omega} \right) E(\omega). \tag{2.13}$$

These findings are applied to find an expression for the electric displacement field

$$D(\omega) = \varepsilon_0 E(\omega) + \mathscr{P}(\omega) = \varepsilon_0 \varepsilon(\omega) E(\omega) = \varepsilon_0 \left[1 + \frac{n_0 \mathrm{e}^2}{m_0 \varepsilon_0} \left(\frac{1}{\omega_0^2 - \omega^2 - \mathrm{i}\gamma\omega} \right) \right] E(\omega), \tag{2.14}$$

which leaves us with an expression for the dielectric function

$$\begin{aligned} \varepsilon(\omega) &= 1 + \left(\frac{f}{\omega_0^2 - \omega^2 - \mathrm{i}\gamma\omega} \right) = 1 + \chi(\omega), \\ f &= \frac{n_0 \mathrm{e}^2}{m_0 \varepsilon_0}. \end{aligned} \tag{2.15}$$

Here ε_0 is the vacuum permittivity and $\chi(\omega)$ the optical susceptibility and f the oscillator strength of the material. Real matter displays more than a single optical resonance, from optical phonons in the IR to deeper shell excitations in the X-ray regime. The influence of lower lying resonances on the dielectric function of a well separated resonance ω_0 is zero. In contrast, all higher lying resonances sufficiently separated contribute by a frequency independent term

$$\sum_{j;\omega_j>\omega_0} \frac{f_j}{\omega_j^2} = \varepsilon_b - 1 \tag{2.16}$$

Here we introduced the background dielectric constant ε_b, which is useful in rewriting Eq. 2.15 as:

$$\varepsilon(\omega) = \varepsilon_b + \left(\frac{f}{\omega_0^2 - \omega^2 - \mathrm{i}\gamma\omega} \right). \tag{2.17}$$

For the highest lying resonance of the system, ε_b equals unity. The background dielectric function of the next lower resonance with regard to ω_0 is often called the static dielectric constant:

$$\varepsilon_s = \varepsilon_b + \frac{f}{\omega_0^2}. \tag{2.18}$$

In our example of an isolated resonance ω_0, $\varepsilon(\omega) \approx \varepsilon_s$ for $\omega << \omega_0$ and $\varepsilon(\omega) \approx \varepsilon_b$ for $\omega >> \omega_0$, which is used to derive an expression for the complex index of refraction $\tilde{n}$ as:

$$\varepsilon(\omega) = \tilde{n}. \tag{2.19}$$

The knowledge of the complex index of refraction gives us access to a great number of optical properties. For example: the real part of the index of refraction is linked to reflection via the Fresnel equations and to refraction by Snell's law while the imaginary part is linked to absorption by Beer's law. Generally, systems of higher dimensionality can display anisotropy which adds a $\mathbf{k}$-dependence to all equations above. A more detailed investigation is found in the previously mentioned textbooks on the subject.

2.2.2 Optical Transitions in Unitary Molecular Systems

In realistic materials, the oscillator resonances described previously are replaced by the optical transitions of valence electrons. As the electrons are not free in neither a single molecule nor in molecular solids, light-matter interaction can only occur for certain photon energies, matching the gap between an occupied and unoccupied electronic state. In this work, we will stay within the limits of the dipole approximation in which the full optical susceptibility is approximated by considering only the first term in a Taylor-series expansion of the electric field. This establishes a linear relation between the electric field and the material's polarization, similar to the oscillator model described above. This relationship is the definition of linear optics. This first order optical susceptibility for excitation from the ground state is given by:

$$\chi^{(1)}(\omega) = \sum_i \left(\frac{f}{\Omega_i^2 - \omega^2 - \mathrm{i}\omega\gamma} \right), \tag{2.20}$$

where $\Omega_i = \omega_0 - \omega_i$ denotes the energy gap between the ground and excited state i and

$$f_i = \frac{2n_0}{\hbar\varepsilon_0}\Omega_i \left| \langle 0| \widehat{H}^D |i\rangle \right|^2, \tag{2.21}$$

which is the oscillator strength for the $0 \rightarrow i$ transition. $\widehat{H}^D$ is the dipole operator e$\mathbf{r}$, which is generally a 3-dimensional tensor. In isolated molecules, optical transitions in the UV-visible (VIS) regime occur between the molecular states described in section 2.1 and their vibrational sublevels.

The vibrational states of molecules do not necessarily influence the observed optical properties of an electronic transition. With respect to their optical properties, we distinguish between two kinds of vibrational states: IR-active and Raman-active modes, named after C.V. Raman [42]. The former are vibrations of the molecule that create a dipole moment to which the light field can couple. These vibrations are directly excitable by photons, usually in the IR range, hence the name. Raman active modes do not necessarily couple directly to the light field. Such modes modify the polarizability of the molecule. From group theory, it is know that in centrosymmetric systems Raman- and IR-active modes are mutually exclusive. As a result every mode is either Raman or IR active, but never both in the molecules studied in this work. Since polarization is the

source of all light-matter coupling changes in the polarizability modify the absorption and emission spectra of the material. As such Raman active modes are of special interest to this work, as we perform measurements of electronic transition. Raman-active modes lead to a vibronic progression of observed transitions which will appear as satellite peaks in the respective spectra. Since there are no strict selection rules for changes in the vibrational system during an optical transition, a great number of replica are potentially observable with varying oscillator strength. The total transition energy of each feature observed is then a sum of the electronic transition energy and the total energy of all vibrons created or annihilated in the process. The relative intensity of these peaks is governed by the Franck-Condon principle.

To visualize the Franck-Condon principle,the potential landscape created by the electron distribution in the electronic ground and first excited state in dependence of a generalized atomic distance parameter R is depicted in Fig. 2.5. The minima of the potential curves R_e are not necessarily found at the same values of R for different electronic states nor do they have the same shape. The different occupied orbitals change the binding energies between the atoms, which leads to a distinct optimal spatial distribution of atoms. Each electronic state features several vibrational sublevels. The most dominant vibron for each potential curve is depicted as a series of states corresponding to the number of vibrons of this species in the molecule. Since the atomic core cannot follow fast changes in the electronic system, transitions in this scheme are vertical, *i.e.*, the parameter R does not change during an optical excitation/de-excitation. The dipole matrix element $\widehat{H}^D_{eN}$ and the total wavefunction $|J\rangle$ can be divided into an electronic $\left(\widehat{H}^D_e;|j\rangle\right)$ and vibrational $\left(\widehat{H}^D_N;|\nu_j\rangle\right)$, respectively, according to

$$\begin{aligned}\widehat{H}^D_{eN} &= \widehat{H}^D_e + \widehat{H}^D_N \\ |J\rangle &= |j\rangle|\nu_j\rangle.\end{aligned} \tag{2.22}$$

Following Eq. 2.21, the corresponding oscillator strength is therefore dependent on

$$\begin{aligned}\langle I|\widehat{H}^D_{eN}|J\rangle &= \langle i|\widehat{H}^D_e|j\rangle\langle\nu_i|\nu_j\rangle + \langle i|j\rangle\langle\nu_i|\widehat{H}^D_N|\nu_j\rangle \\ &= \langle i|\widehat{H}^D_e|j\rangle\langle\nu_i|\nu_j\rangle.\end{aligned} \tag{2.23}$$

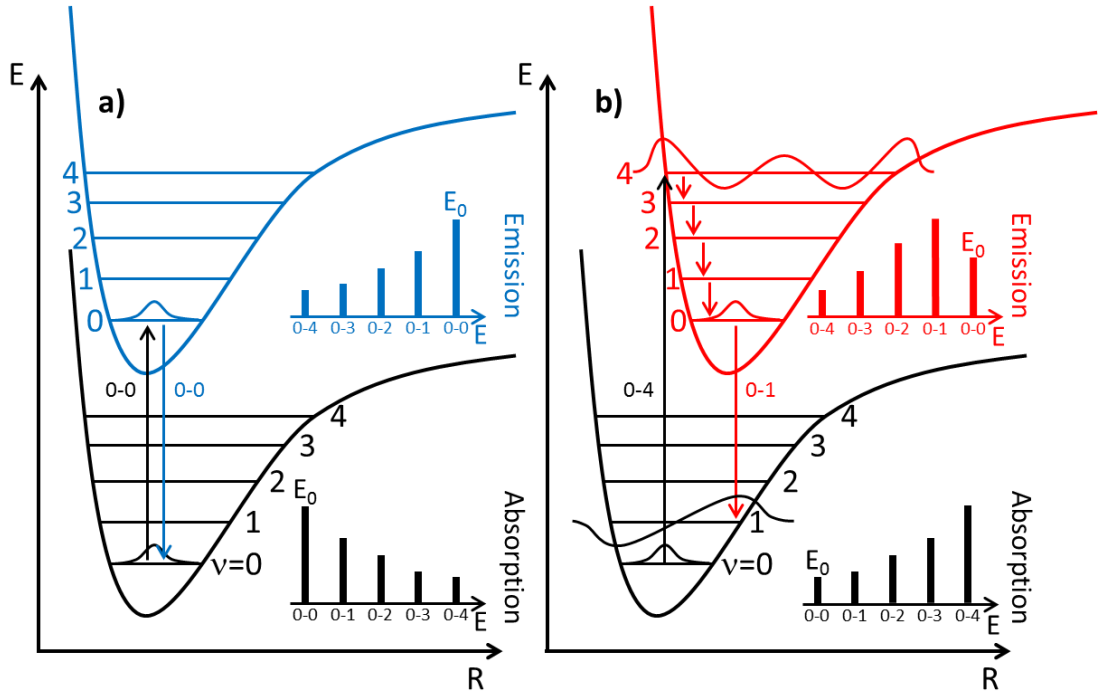

Figure 2.5: Optical transitions in the Franck-Condon picture between two electronic states with similar potential (a) and shifted potentials (b). The four lowest lying vibrational sublevels are depicted in the potential as vertical lines. Their wavefunction is given for the most dominant levels participating in absorption and emission. In both cases, absorption starts from the ν_0 level. In the case of (a), the largest wavefunction overlap is found for the 0-0 transition (black arrow). The resulting intensity distribution for the absorption spectra is shown in the black inlay. The corresponding picture in the shifted case (b) determines the 0-4 transition to be the dominant one. After optical excitation, all carriers relax to the ν_0 state of the excited electronic orbit in (a) and (b). The emission from both potential landscapes is given in the red and blue inlay, respectively. While the 0-0 transition is found at the same energy E_0 in absorption and emission, the transition energies increase in absorption and decrease in emission with increasing vibrational index of the final state. In case of similar potentials (a), this results in a symmetric absorption and emission spectra. However, for shifted potentials (b), the differences in wavefunction overlap lead to deviations from symmetric absorption and emission spectra, as seen by the black and red inlay in subfigure (b).

The second term of the first line of Eq. 2.23 is zero due to the orthogonality of the electronic wavefunctions. Hence, the relative intensity of all vibrational sublevels of a given electronic transition is governed by the total vibronic wavefunction overlap

$\langle v_i | v_j \rangle$, also called the Franck-Condon factor.
Similar to the Born-Oppenheimer approximation from atomic physics, we assume that the heavy atomic nuclei of the molecule cannot follow the fast changes in the electron density, *e.g.*, as introduced by an optical transition. Therefore, transitions in this scheme are vertical, *i.e.*, the parameter R does not change during the absorption or emission of a photon. This has implications on the absorption and emission processes of a photon. The vibrational ground state has its maximum at the center, whereas all other states at the edge of the potential curve. For most materials in equilibrium, especially at low temperatures, only the zero-vibrational mode of the electronic ground state displays any significant occupation. The vibrational ground state of both electronic states has the largest overlap if both electronic states have their potential minimum at the same position. Hence, the 0-0 vibrational transition between both states has the highest oscillator strength. All other transition show diminishing intensity proportional to their decreasing wavefunction overlap. However, electronic transitions are not necessarily between states with similarly shaped potential curves and the observed vibronic substructure varies accordingly (Fig. 2.23b). For a system in the ground state all electrons come from the same initial state and as such the vibronic structure seen in absorption is that of the excited state.
After a broadband optical excitation, a multitude of vibrational states in the excited electronic state will be occupied. Following excitation, those carriers will relax back into the ground state via emission of a photon. However, internal vibrational relaxation within an electronic state is orders of magnitude faster than relaxation back to the electronic ground state. In the majority of cases, all carriers will gather in the vibrational ground state of the excited electronic state before emission relaxes the molecule back to the electronic ground state. As with absorption, emission is governed by the Franck-Condon principle, but now the initial state is the vibrational ground state of the excited electronic state while the final state can be anywhere within the vibrational subsystem of the electronic ground state. As absorption reveals the Raman active vibrational sublevels of the excited electronic state, emission spectroscopy gives information of the corresponding levels of the electronic ground state.
For the simplest case of equally shaped potential curves with equal values of R_e and similar vibrational subsystems, the resulting absorption and emission spectra will mirror each other symmetrically around the 0-0 transition. For both emission and absorption

spectra, the most intense line will be the 0-0 transition. The 0-1 transition will lead to an increase in energy in absorption equal to $(\nu_1 - \nu_0)$. However, in emission, the 0-1 transition will be red-shifted by the same amount. Since both transitions are constructed from the same wavefunctions, the Franck-Condon factor would be the same and both lines would have the same relative intensities when compared to the respective 0-0 lines. Deviations from this simple mirror image are indications of differences in electronic potential and vibronic substructure between the electronic ground and excited states. Increasing the spectral resolution of the experiment reveals an underlying substructure within every vibrational replica. These features are due to molecular rotations or librations in the solid state. Since these need sub μ eV energetic resolution to resolve their treatment is neglected in this work.

2.2.3 Optical Transitions in Molecular Crystals: Frenkel Excitons

As this works studies organic semiconductors with exciton binding energies of several 100 meV, most of the optical features investigated stem from excitonic resonances. Therefore, the treatment of electronic band to band transitions in organic solids will not be discussed here. The vanishing dispersion in molecular crystals further reduces the necessity of introducing a full electronic band structure. The interested reader is referred to the available literature on this topic in which a full band-structure investigation is discussed [29, 27, 43].

This section starts with a review of excitons from the HOMO-LUMO levels described in Section 2.1. In contrast to single molecules, the excited carriers in a crystal, electrons and holes alike, can move freely within the solid. As both quasi particles have an opposite charge, they can interact via Coulomb interaction. Similar to a proton and an electron, this can lead to the formations of a whole system of bound states. For protons and electrons, this is known as a hydrogen atom. In solids of any kind, the correlated electron-hole pair is called an exciton. Since such a bound state lowers the total energy of the system by its excitonic binding energy, the excitonic resonances are found within the bandgap of the material in absorption and emission. In inorganic materials, where the Born-Oppenheimer approximation is justified, the shape of the

excitonic wavefunction does not differ qualitatively from the solution of the hydrogen problem. These kinds of excitons are called Wannier excitons. Their excitonic binding energy is usually lowered by three orders of magnitude when compared to the binding energy of a hydrogen atom. This is due to the difference in effective mass of the participating particles and due to dielectric screening mitigating the Coulomb interaction due to the dielectric background of the environment. As a result, Wannier excitons are delocalized across multiple crystalline unit cells. However, the flat bands in van-der-Waals-bound crystals lead to a breakdown in the Born Oppenheimer approximation. Weak intermolecular interaction infers weak Coulomb-screening. Therefore, excitonic binding energies for organic semiconductors range from 100 meV up to several eV. Strong binding in turn leads to the localization of the exciton down to a single molecule. These excitons are called Frenkel excitons. Of course, as with every approximation, there is no distinct parameter value which can be pinpointed as the dividing line between Frenkel and Wannier excitons. This work will demonstrate how even in organic solids, intermolecular interactions can be increased by stacking the π orbitals of aromatic molecules, leading to noticeable dispersion. For a theoretical treatment of Frenkel excitons, the Hamilton operator for an extended molecular crystal is considered

$$H = \sum_{m\alpha} H_{m\alpha} + \sum_{m\alpha} H_{m\alpha<n\beta} V_{m\alpha;n\beta}. \tag{2.24}$$

$H_{m\alpha}$ is the Hamilton operator of a single molecule at the lattice site m and position α in the crystalline unit cell. $V_{m\alpha;n\beta}$ describes the interactions of all molecules in the crystal with each other. The indexes m and n sum over all crystal sites where α and β sum over all molecules in a single unit cell. With no optical excitation, the wavefunction for the crystalline ground state is a superposition of the single-molecular wavefunctions φ

$$\Phi_G = \mathscr{A} \prod_{m\alpha} \varphi_{m\alpha}, \tag{2.25}$$

where the operator $\mathscr{A}$ is introduced which ensures the total wavefunction to be anti-symmetric. Correspondingly, the wavefunction for a single excited molecule localized to the crystal site at the $n-\alpha$ position is given by

$$\Phi_G^* = \mathscr{A}\varphi_{n\alpha}^* \prod_{n\alpha \neq m\alpha} \varphi_{m\alpha}, \tag{2.26}$$

which corresponds to a completely localized excitation. However, this set of wavefunctions is not an eigenfunctions of the Hamiltonian in Eq. 2.24, since it does not fulfill the required symmetry criteria of the periodic potential of the crystal lattice. These properties are satisfied by a Bloch-wave ansatz resulting in

$$\Psi_\alpha(\mathbf{k}) = \frac{1}{\sqrt{N}} \sum_n \Phi_{n\alpha}^* \mathrm{e}^{\mathrm{i}\mathbf{k}\mathbf{R}_{n\alpha}}, \tag{2.27}$$

where the sum over all possible positions $\mathbf{R}_{n\alpha}$ of the excited molecule within the volume of interest is taken. These are the basic excitonic wavefunctions of the crystals. Within the limit of no intermolecular coupling, all different $\mathbf{k}$-states would be energetically degenerate. Indeed, the width of exciton bands is very narrow in organic solids in congruence with their weak intermolecular binding. However, they are not zero: molecular interaction leads to a splitting of the exciton bands, especially for differently aligned molecules within one crystalline unit cell due to an exchange of excitation between two molecules. This effect is known as Davydov splitting, named after A.S. Davydov for his pioneering work on excitons in molecular crystals [44].
This effect is investigated by considering two molecules within a single unit cell, ignoring exchange interactions, based on the publication [45]. If both molecules are in the ground state, the total energy is given using the hamiltonian from Eq. 2.24 in a two molecule one unit cell limit by

$$E_G = \langle \Phi_G | H | \Phi_G \rangle = E_\alpha + E_\beta + \langle \varphi_\beta | V_{\alpha\beta} | \varphi_\alpha \rangle, \tag{2.28}$$

$$V_{\alpha\beta} = \frac{\mathrm{e}^2}{|\mathbf{r}_\alpha - \mathbf{r}_\beta|} = \frac{\mathrm{e}^2}{|\mathbf{R}|}. \tag{2.29}$$

The wavefunctions chosen are those constructed in Eq. 2.26, where the index of the unit cell for the single molecular wavefunctions is omitted due to our current restriction on

a single unit cell. $\mathbf{r}_\alpha/\mathbf{r}_\beta$ denote the position of the molecule with the index α and β respectively and $\mathbf{R}$ as their respective relative position. The first two terms on the right hand side of Eq. 2.28 represent the ground state energies of each respective molecule. They are identical for identical molecules, while the last term describes the van-der-Waals interaction between both molecules introduced as a small perturbation to the system. The corresponding exited dimer, where one molecule is in the ground state and one is excited, is given by

$$\Psi_{\alpha\beta} = a\Phi^*_\alpha + b\Phi^*_\beta, \tag{2.30}$$

where a and b are coefficients still to be determined. The corresponding energy levels are obtained by solving the Schroedinger equation

$$H(\Psi_{\alpha\beta}) = E\Psi_{\alpha\beta}. \tag{2.31}$$

Multiplying both sides of this equation by Φ^*_α and repeating this process by multiplying with Φ^*_β leaves us with two equations containing the following terms

$$\begin{aligned} H_{\alpha\alpha} &= H_{\beta\beta} = \langle\Phi^*_\alpha|H|\Phi^*_\alpha\rangle, \\ H_{\alpha\beta} &= H_{\beta\alpha} = \langle\Phi^*_\beta|H|\Phi^*_\alpha\rangle. \end{aligned} \tag{2.32}$$

To determine the coefficients a and b the equation

$$\begin{vmatrix} H_{\alpha\alpha} - E_{Exc} & H_{\alpha\beta} \\ H_{\beta\alpha} & H_{\beta\beta} - E_{Exc} \end{vmatrix} = 0 \tag{2.33}$$

is solved. As a result

$$\begin{aligned} E'_{Exc} &= H_{\alpha\alpha} + H_{\alpha\beta}; \quad \Psi^+_{\alpha\beta} = \frac{1}{\sqrt{2}}\left(\Phi^*_\alpha + \Phi^*_\beta\right), \\ E''_{Exc} &= H_{\alpha\alpha} - H_{\alpha\beta}; \quad \Psi^-_{\alpha\beta} = \frac{1}{\sqrt{2}}\left(\Phi^*_\alpha - \Phi^*_\beta\right) \end{aligned} \tag{2.34}$$

is obtained, which combines with Eq. 2.32 yields

$$E'_{Exc} = E^*_\alpha + E_\beta + \langle \Phi^*_\alpha | V_{\alpha\beta} | \Phi^*_\alpha \rangle + \langle \Phi^*_\beta | V_{\alpha\beta} | \Phi^*_\alpha \rangle,$$
$$E''_{Exc} = E^*_\alpha + E_\beta + \langle \Phi^*_\alpha | V_{\alpha\beta} | \Phi^*_\alpha \rangle - \langle \Phi^*_\beta | V_{\alpha\beta} | \Phi^*_\alpha \rangle. \tag{2.35}$$

The first two terms in both equations are the energies of the single excited and unexcited molecule, respectively. The third one corresponds to the van-der-Waals term in Eq. 2.28. It is called the exciton splitting term S, for reasons that will soon become apparent. It describes the exchange of excitation between both molecules. In a point dipole approximation, it can be written as:

$$S = \frac{\mu_\alpha \cdot \mu_\beta}{R^3} - \frac{3\,(\mu_\alpha \cdot \mathbf{R})\left(\mu_\beta \cdot \mathbf{R}\right)}{R^5}. \tag{2.36}$$

This vectorial equation depends strongly on the alignment of the molecules and their dipole transition elements μ_α and μ_β, respectively. To determine the total energy shift due to excitation, Eq. 2.35 is subtracted from Eq. 2.28 to obtain

$$\Delta E = \Delta E_{mol} + \Delta D \pm S. \tag{2.37}$$

The first term describes the energy difference between a single molecule in the ground and excited state. The second term is related to the difference in van-der-Waal interactions in a crystal with and without an exciton. In the case of a crystal with a single molecule in the unit cell, the full energy difference is completely described by both these terms. However, in our example of two molecules in a unit cell, the additional exciton splitting term further influences the energy levels of the crystal and therefore the observable signal in absorption spectroscopy. The influence of the exciton splitting term can intuitively be understood by visualization a dimer of molecules. For two in-plane oscillators, the splitting between the two so called Davydov components at E'' and E' is called Davydov splitting and given by

$$2S = \frac{2|\langle \Phi_G | \mu | \Psi^{\pm}_{\alpha\beta} \rangle|^2}{R^3} \left[\cos(\alpha) + 3\cos^2(\theta)\right]. \tag{2.38}$$

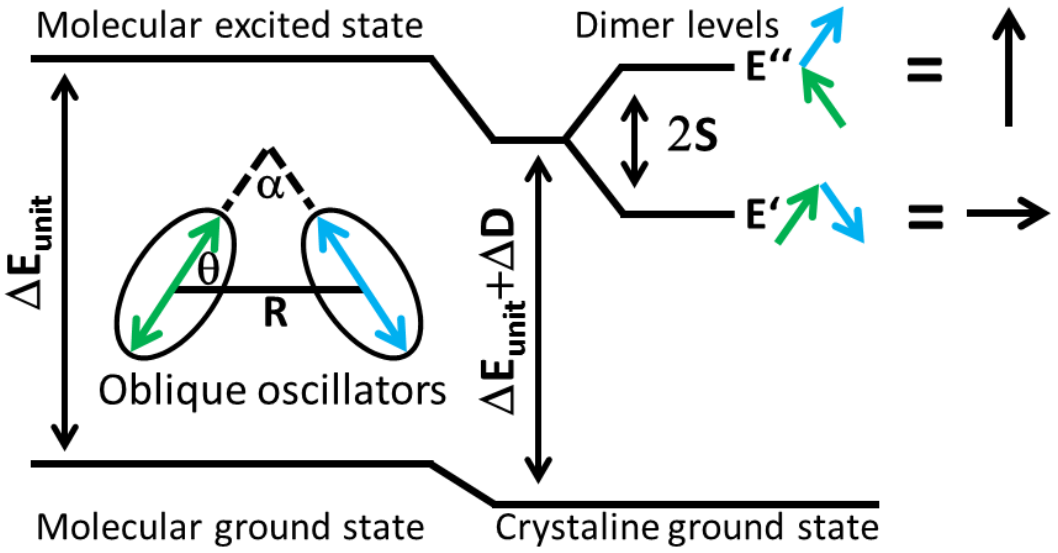

Figure 2.6: Visualization of the Davydov splitting for oblique oscillators. The geometry of both molecules in the unit cell with their relative angles θ and α and separation distance R is given in a small pictogram in the middle. If one tracks the energy levels when going from a single molecular case to a crystal, both the ground and excited state are shifted due to van-der-Waals interactions with their neighbors, however, to a different extend. This adds a shift ΔD to the transition energy between both states. Furthermore, the final energy level in the excited state splits due to excitation exchange interaction between both molecules, the so called Davydov splitting. The polarization and oscillator strength of both Davydov components is constructed by adding the transition dipoles of both molecules for in and out of phase oscillations and evaluating the resulting vectors direction and magnitude. Both components are always polarized perpendicular to each other.

The definition of both angles α and θ in Eq. 2.38 is visualized in Fig. 2.6, which demonstrates the energy levels observed in absorption spectroscopy for two molecules in a unit cell with oblique dipole moments. The oscillator strength and polarization of both Davydov components depends on the coupling oscillator modes of the two molecules involved: different results are obtained for in-phase and out-of-phase oscillating dipoles. By adding the green and blue arrows in Fig. 2.6 which represents the dipole moments of the single molecules, one obtains the excitonic eigenmodes of the crystal (black arrow), the so called 'Davydov components'. The oscillator strength of the transition is represented by the length of the resulting black arrows. As a consequence, for parallel

oscillators, the total dipole moment of the out-of-phase mode reduces to zero (see Fig. 2.7). Therefore, the Davydov splitting is observed in spectroscopy as a static shift, as only one component exhibits non-vanishing oscillator strength.

The whole discussion is simplified in nature. More complicated situations in relative

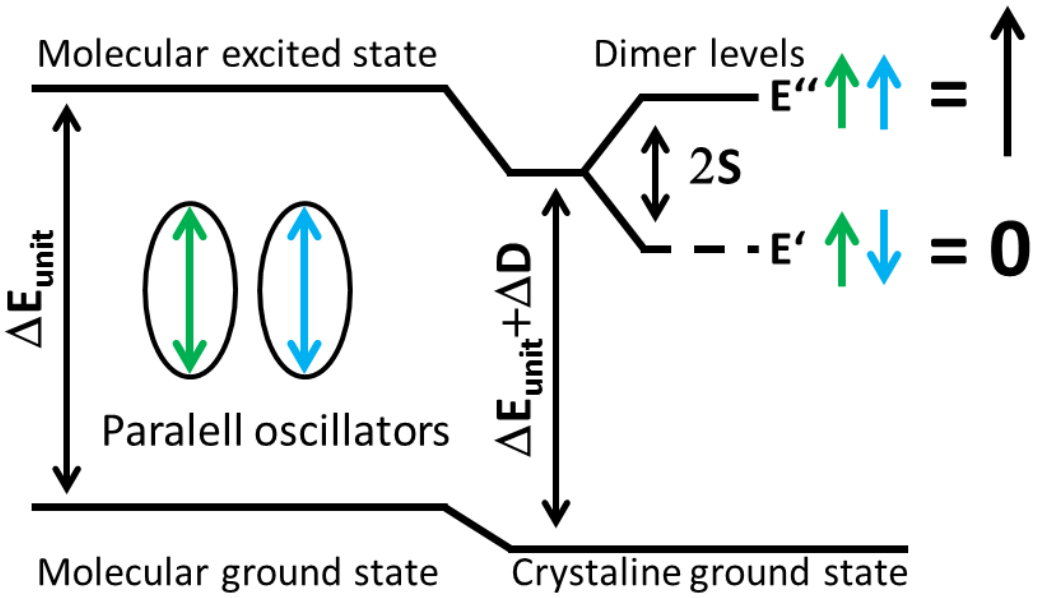

Figure 2.7: Visualization of the Davydov splitting for parallel oscillators, equivalent in construction to Fig. 2.6. With both molecular dipoles parallel to each other, both cancel each other out for out of phase oscillations. Only one transition is observed in absorption spectroscopy.

molecular alignment and positioning are discussed in Ref. [45]. Additionally, the case of two molecules within a unit cell is discussed. However, the physics remain the same for any number of molecules: all Davydov components are constructed by adding up the dipole moments of all molecules in the unit cell with all conceivable combinations of relative phase. This will resolve in Z different Davydov components, where Z is the number of molecules in the unit cell.

2.2.4 Charge-Transfer Excitons and Interface States

Introducing Coulomb interactions between molecules as a weak perturbation leads to the previously discussed Frenkel excitons. These are the neutral excitations in the limit of localization to a unit cell. The other extreme of excitons delocalizes across multiple crystalline unit cells is the hydrogen like Wannier exciton. Both extremes are discussed extensively in text books. However, while these two extremes are easily accessible due to their respective theoretical approach, they do not encompass all observable types of excitons.

Charge-transfer(CT) excitons are found in between Frenkel and Wannier excitons: they are delocalized across only a few, commonly two, molecules. While as a whole a CT-exciton is a charge-neutral quasiparticle, it is polar in nature. If, in a gedankenexperiment, one would fix the hole or electron of such an exciton in place, the respective other particle would show a minimum in its wavefunction at this position. Hence, those particles show distinct ionic contributions to their total energy. The total energy of such a state is given by

$$E_{CT} = I_D - E_A - P_{eh}(\mathbf{r}) - C(\mathbf{r}). \tag{2.39}$$

The first term I_D is the ionization potential of the molecule at the lattice site of the hole. This molecule is called the donor molecule. Accordingly, E_A is the electron affinity of the molecule at the lattice site of the electron. This molecule is the acceptor molecule. The last two terms depend on the electron hole distance $\mathbf{r}$: $P_{eh}(\mathbf{r})$ is the energy stored in the polarization of the lattice induced by the electron and hole and $C(\mathbf{r})$ describes the Coulomb interaction between the hole and electron. Separating opposing charges increases the systems total energy. As the polar nature of CT-excitons infers charge separation, their total energy level is above the energy level of Frenkel-type excitons in the same material. However, they exhibit very low oscillator strength and are rarely observed in linear optical spectroscopy, as they are often lost in the flank of more intense Frenkel exciton resonances. While they are difficult to observe in simple emission or absorption experiments, the polar nature of CT-excitons renders them very responsive to external electric fields. Hence, they are often investigate in electro-absorption or electro-reflection experiments.

It is important to distinguish between two types of CT-excitons. The first kind can

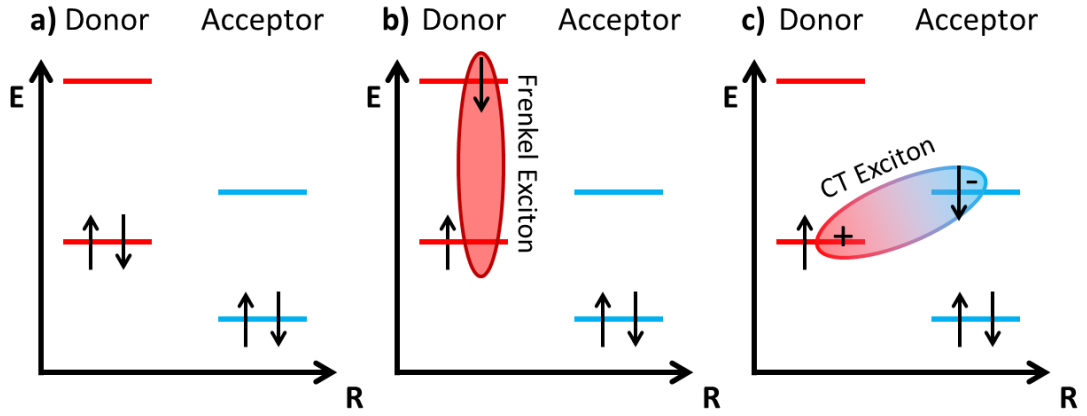

Figure 2.8: HOMO-LUMO levels at a molecular donor-acceptor interface in the ground state (a), with an excited Frenkel type exciton in the donor (b) and for an excited CT-exciton across the donor-acceptor interface (c). Note that in this simplified picture, electronic transitions are shown, with the ovals symbolizing from which electronic orbitals excitons will form. Since they are two-particle states, exciton levels cannot be depicted in these level schemes. In all three subfigures, energy is depicted on the vertical axis, while the horizontal axis depicts displacement in real space. As can be seen, the Frenkel exciton is localized to the Donor molecule (b). No special separation between hole and electron is found. In contrast, the charge transfer exciton shows a polar character, with the hole situated in the donor and the electron found in the acceptor molecule (c). In this example, the CT-exciton represents the lowest lying electronic transition of the whole heterostructure, due to the small donor HOMO to Acceptor LUMO energy offset.

be found in homo-molecular crystals, *i.e.*, crystals that consist of only one kind of molecule. In this case, the first two terms in Eq. 2.39 stem from the same kind of molecule, hence they correspond to the HOMO-LUMO transition energy for that molecule. Such excitonic states are discussed as precursors for singlet fission [46] as described in Section. 2.2.6. The second type of CT-excitons can form across an internal interface or across two different types of molecules in a molecular heterosystem [14]. In this case, the first two terms in Eq. 2.39 define a HOMO-LUMO transition between the HOMO of one material and LUMO of another. Depending on the relative level alignment at the interface, the total energy of this interface CT-exciton can be the lowest lying excited electronic state in the system, including Frenkel-type excitons in the constituent

layers. They are of special interest for applications in OPV, where they are discussed as precursors for charge-separation [35, 14, 36, 37, 38, 39]. The exact nature of this process is still unclear: the role of hot CT states which could provide enough excess energy to overcome the energy barrier to form free carriers as suggested in [47, 15] remains disputed [48]. Such excitons can have significant signal strength in photoluminescence (PL) spectroscopy, as most excitons will relax to the lowest lying available energy state before recombining radiatively. After optical excitation with sufficiently high photon energy, a realistic material would feature a multitude of exciton species: Frenkel excitons in both constituent molecules, CT-excitons restricted to the donor and acceptor layers, and interfacial CT-state in molecular heterostructures, all with their hierarchy of higher lying states and vibronic progressions. Not all of these exciton species can decay via internal conversion into the CT-state. This can be due to spatial separation from the interface for thicker donor and acceptor layers, or due to vanishing electronic coupling to the final CT-exciton. The exact contribution of the different states to the formation of CT-excitons have to be evaluated on a case-by-case basis, *e.g.*, by photoluminescence excitation (PLE) measurements.
Additionally, it cannot be ruled out that the electronic levels of the molecules themselves remain completely unperturbed by their environment, especially in the regime of stronger intermolecular donor-acceptor coupling. Hence, completely new states can form at the interface, which cannot be described in a simple picture of the HOMO and LUMO orbitals of the involved molecules, as has been done in Fig. 2.8. These new interface states have to be evaluated depending on the interface in question.

2.2.5 Excimers and Self-Trapped Excitons in Molecular Crystals

In contrast to covalently bound inorganic crystals, intermolecular interactions in molecular solids are rather weak. In the previous discussion of the Davydov splitting, the influence of optical (or electrical) excitation on the van-der-Waals interaction energies where already encountered in the parameter ΔD. It is easily conceivable that such a shift in energy should distort the lattice of the crystal in the vicinity of such an excitation. This is especially true when the shift is negligible when compared to the magnitude

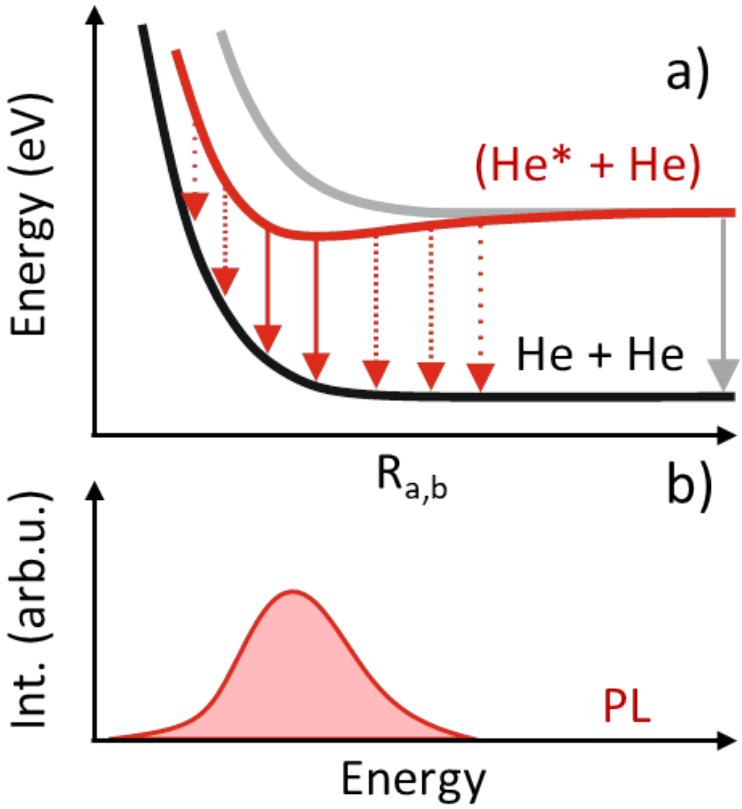

Figure 2.9: Visualization of the total energy of the first excited and ground state during excimer formation of He_2 in dependence of the nucleus to nucleus distance $R_{A,B}$ (a) and the resulting excimer emission (b). The ground state potential is given in black, the exited state energy for separated helium atoms in grey and the excimer potential is given in red. The minimum for the excimer potential is found at very low values of $R_{A,B}$. The eventual emission is symbolized by the red arrows and visibly red shifted when compared to the energetic separation of the ground state and excited state for bigger values of $R_{A,B}$, which would correspond to emission from the monomeric excited state (grey arrow). Hence, the excimer emission is broadened and red shifted to the monomer emission. Vibrational and rotational sublevels are committed in this depiction. Adapted from [49].

of the van-der-Waals interaction in the crystalline ground state. In a self-consistent way, every shift in the lattice constant will influence the magnitude of intermolecular interactions and therefore further change the energy levels of an excited state. The new state created this way is highly localized by its own lattice distortion as it cannot

exist in the unperturbed crystal. Should the excitation lead to the formation of an exciton, we call such a state a self-trapped exciton [50]. Emission from these states is necessarily very slow. The ground and excited state exist at different lattice parameters and a transition between both has to be accompanied by a lattice relaxation witch can only happen over longer timescales with decay times of several nanosecond. For the same reason, self-trapped exciton states are generally not visible in absorption as absorption is quasi instantaneous on the timescale of any possible lattice deformations direct excitation of self-trapped exciton states are impossible in solids. Such states form after excitation of higher lying states and subsequent exciton relaxation.
The excimer is a bound state of two molecules, which would be repulsive in the ground state. However, once one of the two molecules is excited, the interaction orbital between both molecules switches from anti-bonding to bonding (see Section. 2.1) allowing both molecules to form a stable bond. Excimers have been observed for organic systems like such as pyrene in solution [51], the vapor phase [49] and multiple molecular crystals [52, 53]. They share many properties with the self-trapped exciton. The long lifetimes of excimers are exploited for easier population inversion in excimer lasers, as first demonstrated in 1970 [54]. These found widespread commercial applications in the medical and lithographic sector. A textbook example for an excimer is the He_2 molecule. Its electron configuration in the ground state is given by $2s\sigma^1 2s\sigma^{*1}$. In total, the antibonding character of the σ^* orbitals outweighs the attractive force of the bonding orbitals. In contrast, after excitation, the new electron configuration is $1s\sigma^2 2s\sigma^1 1s\sigma^{*1}$ which has a negative total binding energy and therefore a bonding character. A bond is formed. Figure 2.9 displays the potential landscape in dependance of the average distance between the two helium nuclei for a helium excimer and the resulting emission signal. It becomes immediately apparent that an excimer is only stable for very short intermolecular distances. While this is easily achievable in solution where molecules are free to move, the rigidity of the crystal lattice in the solid state might hinder excimer formation. As the ground state is purely repulsive, carrier relaxation from the potential minimum of the excimer state results in a featureless broadband PL signal, as shown in Fig. 2.9. Similar to the self-trapped exciton, such states will not be visible in absorption spectroscopy in molecular crystals. Excimer formation is always accompanied by a lattice distortion to achieve the necessary low molecular distances. Changes in the electronic system of the crystal due to optical excitation are too fast to allow for movement

of the much heavier molecules. However, such states can form after excitation and influence the properties of the visible emission. Their increase in binding energy renders excimers exceptionally stable with very weak optical coupling to the ground state. As a result, huge red-shifts of several 100 meV are observed when compared to the monomer signal and carrier lifetimes increases by many orders of magnitude.

2.2.6 Singlet and Triplet States and Intersystem Crossing

As spin-orbit coupling between atoms grows with the atomic mass squared, spin remains a good quantum number for molecules containing only relatively light atoms. This is the case for the acenes and perfluorinated acenes who are subject of this work. These molecules are comprised of fluorine, hydrogen and carbon atoms. In these molecules, the HOMO levels are occupied by two electrons. The vanishing influence of spin orbit coupling allows us to factor the total wavefunction into two parts, a spatial wavefunction $\varphi(\mathbf{r})$ and a spin wavefunction$\chi(\sigma)$:

$$\Phi_S(\mathbf{r},\sigma) = \varphi(\mathbf{r})\chi(\sigma). \tag{2.40}$$

To take into account their fermionic nature, this wavefunction needs to be antisymmetric under exchange of the electrons. Should both the spatial and the spin wavefunction be antisymmmetric or symmetric, the resulting total wavefunction is always symmetric. Hence, either the spin or the spatial wavefunction need to be symmetric, the respective other antisymmetric to achieve an antisymmetric total wavefunction. The ground state of such a system displays a symmetric spatial wavefunction with both electrons in the ground state φ_1 and an antisymmetric spin wavefunction. These state is called a singlet states, as there is only one way to construct such a state:

$$\Phi_S(\mathbf{r},\sigma) = \varphi_1(1)\varphi_1(2)\left[\chi_\uparrow(1)\chi_\downarrow(2) - \chi_\downarrow(1)\chi_\uparrow(2)\right], \tag{2.41}$$

where $\varphi_i(j)$ denotes the spatial part of the wavefunction and $\chi_\uparrow(j)$ or $\chi_\downarrow(j)$ the spin wavefunction with upwards and downwards spin of the electron j, respectively. The next higher levels are occupied by the triplet states, where the spatial wavefunction is

antisymmetric with one electron in the excited state φ_2 while the spin wavefunction is symmetric. There are three different ways to construct such a state:

$$\begin{aligned}
\Phi_T^1(\mathbf{r},\sigma) &= [\varphi_1(1)\varphi_2(2) - \varphi_2(1)\varphi_1(2)]\,\chi_\uparrow(1)\chi_\uparrow(2),\\
\Phi_T^2(\mathbf{r},\sigma) &= [\varphi_1(1)\varphi_2(2) - \varphi_2(1)\varphi_1(2)]\,\chi_\downarrow(1)\chi_\downarrow(2),\\
\Phi_T^3(\mathbf{r},\sigma) &= [\varphi_1(1)\varphi_2(2) - \varphi_2(1)\varphi_1(2)]\left[\chi_\uparrow(1)\chi_\uparrow(2) + \chi_\downarrow(1)\chi_\downarrow(2)\right],
\end{aligned} \tag{2.42}$$

hence the name triplet. In first approximation, the Hamiltonian of the system is not spin dependent. Hence, these three triplet states are energetically degenerate. However, in reality, even with negligible spin orbit coupling, some interaction is found, especially spin dipole-dipole interaction [55]. It is of notice that for transitions between singlet and triplet electronic orbitals and their respective exciton states, a spin flip is required, which is forbidden as long as the spin remains good quantum number. While this means such intersystem transitions are extremely rare for the molecules studied here, they are not completely ruled out. This holds true for absorption and emission. Hence, emission from the lowest-lying triplet state displays multiple orders of magnitude longer lifetimes than emission from the first excited singlet state, as the former requires an extremely rare spin flip and the later does not. Emission from triplet states is called phosphorescence, while singlet emission is called fluorescence for historical reasons [56, 57]. Nevertheless, the triplet states still play an important role in the optical properties of many molecular crystals, even when triplet states are uninvolved in direct light-matter interaction. This is due to singlet to triplet conversion, also called singlet exciton fission, where one singlet exciton is converted into two triplet excitons. This process conserves the total spin. As no spin flip is necessary, exciton conversion by singlet fission can be quiet fast and efficient. However, a prerequisite of efficient singlet fission is a suitable level alignment: to avoid violating energy conversion the energy of the triplet state needs to be similar to half the energy of the first excited singlet state. The mechanism of singlet fission was introduced in 1965 [58] to explain the photophysics of anthracene, this process is especially interesting for applications in photovoltaics. One exciting photon creating one singlet exciton can subsequently be responsible for the creation of two triplet excitations. This enables quantum yields above the Shockly-Queisser limit [59]. A comprehensive review of the effect is found in [55, 41]. The process of singlet fission and its reverse process triplet fusion is displayed in Fig. 2.10.

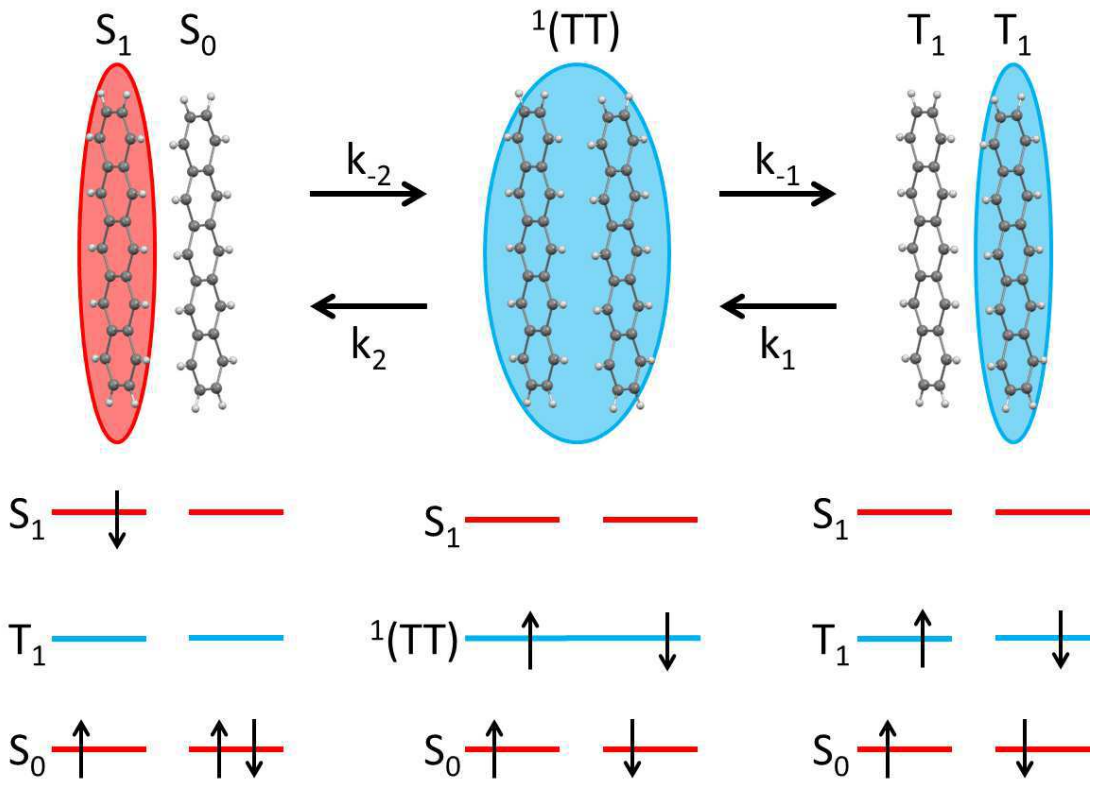

Figure 2.10: A schematic overview of singlet fission and its reverse process triplet fusion in three steps. The initial singlet state (left) delocalizes and forms a correlated triplet state $^1(TT)$ (center) across both involved molecules with the rate k_{-2}. This state dissociates into two independent triplet excitons (right) with the rate k_{-1}. k_2 and k_1 represent the respective reverse processes. All involved states are shown in the bottom half in a simple level scheme, with the electron depicted as arrows according to their respective spin. Every state but the correlated triplet is localized on one molecule. When evaluating the total spin of the correlated triplet state $^1(TT)$, we find it to be zero. Therefore $^1(TT)$ as a whole is a singlet state.

Two molecules need to interact for singlet exciton fission to be possible: one in the ground state S_0, one in an excited singlet state, S_1 in the case depicted in Fig. 2.10. Intermolecular interaction is key for singlet fission. As the initial excitation is localized on only one molecule, a delocalized CT-exciton state has to form as a first step towards two separated triplet states [46]. Such an intermediate step is neccesary due to Pauli blocking, which prohibits two excitons from coexisting on the same molecule. Once delocalized, intersystem crossing leads to a correlated triplet pair $^1(TT)$, which can

separate into two unique triplet states T_1. The intermediate state $^1(TT)$ is a coherent superposition of all possible triplet states of both molecules with a resulting total spin of zero. Thus, $^1(TT)$ is a singlet state if evaluated as a whole. The transition rate $S_1S_0 \rightarrow ^1(TT)$, and its ratio to the rate of the corresponding reverse process k_{-2} is usually the bottle neck for efficient singlet fission.

$$\varepsilon = \frac{k_2}{k_{-1}} \tag{2.43}$$

is referred to as the branching ration, describing the likeliness of the correlated triplet to separate into two triplets opposed to one singlet exciton.
The simplest requirement for singlet fission is an energetic one. No intersystem crossing will be observed for $E_{S_1} < 2E_{T_1}$ without sufficient vibrational contribution. The reverse holds true for triplet fusion. Special attention needs to be taken for $E_{S_1} \approx 2E_{T_1}$ as both singlet fission and triplet fusion can occur in the same material system. A more intricate parameter for fission or fusion is the molecular packing within the crystal: the efficiency of exciton conversion is strongly dependent on the wavefunction overlap of the interacting molecules. Molecular crystals are often anisotropic with strongly varying wavefunction overlap of the next nearest neighbor molecules depending on the crystalline axis. Thus, singlet fission can be strongly anisotropic [60].
The influence of singlet fission can be seen in time-resolved photoluminescence (TRPL) measurements of the singlet state. With suitable crystalline structure and energy level alignment, singlet fission can occur with effective conversion times in the sub picosecond range. Hence, efficient singlet fission depopulates the singlet state rapidly after an optical excitation. Radiative recombination is in direct competition with singlet fission and will be heavily quenched when fission occurs. In this case the observed radiative lifetimes are significantly shortened as fission time is the leading factor in depopulating the excited state. Triplet fusion, on the other hand, is observable as delayed fluorescence. The triplet subsystem acts as a shelf state for singlet excitons. The weak coupling to the light field results in an almost decay free triplet state on the timescales of the fluorescence. Sufficient population of the triplet state leads to a feeding of the singlet exciton state by triplet fusion, even after all of the initial singlet population has relaxed back to the ground state. Hence, a long lived fluorescence tail is observed, with time dynamics governed by the usually long-lived triplet states and

intersystem-crossing efficiency. In most cases, this effect cannot be observed after an optical excitation as direct triplet excitation is dipole forbidden. However, should both fission and fusion be energetically possible in the same material, the resulting constant energy transfer between singlet and triplet states in competition with radiative relaxation can result in a PL spectra with fast initial decay governed by fission, followed by a long lived PL tail, with decay dynamics governed by a complicated convolution of radiative decay, singlet fission and triplet fusion rates. Delayed fluorescence has found a possible application for increasing the yield of electrically pumped OLED, as it can convert the dark triplet states populated by electronic excitation into bright singlet excitons, increasing the fluorescence yield in the process [61, 62].

2.2.7 Propagation of Light in the Strong Coupling Regime: Polaritons

Different types of excited matter states and optical resonances observable in spectroscopic measurements have been discussed in previous section of this thesis. All of these have been introduced in the weak coupling regime where an optical transition is excited by a photon, creating an excited state, which can decay back into the ground state by emitting a photon. Besides the occasional creation or annihilation of a photon, the light field itself is unperturbed by the excited state and *vice versa*. This is an oversimplification well justified for weak coupling between the light field and the material. However, every excited state is coupled to the light field by a polarization in the material, which itself couples back to the light field. In energetic regions of strong light-matter coupling, the propagating photon and the respective excited state are basically indistinguishable. The self-consistent treatment of this feedback loop leads to the formation of a new quasi particle, the polariton, which is a mixture of the matter excitation and a photon. Polaritons are further classified according to the resonance responsible for the light-matter interaction, *e.g.*, exciton-polaritons, phonon-polaritons, plasmon-polariton. Even though such polaritons arise for many different reasons, their properties can all be treated in the same way. Additionally, polaritons can be classified according to the nature of their photonic half. This is typically a free photon with a linear dispersion relation according to the dielectric background of the medium it

travels in. This is not always the case, especially in the coupling of excitons to cavity photons. These so-called cavity exciton polaritons have been of great interest in the last decade due to their applications in polariton lasers [63, 64]. As all optical measurements performed for this thesis have been made outside a cavity with free photons, cavity modes will not be taken into account here. To investigate the propagation of a polariton through a medium, the polaritonic dispersion relation has to be determined. The wave vector of a photon in vacuum is connected to the wave vector in a medium by

$$k^2 = \tilde{n}^2(\omega)k_v^2, \tag{2.44}$$

where the squares have been taken to eliminate the vector character of the wave vectors. Equations. 2.17, 2.19 and $k_v^2 = (\omega/\mathrm{c})^2$ are used to obtain

$$\frac{\mathrm{c}^2k^2}{\omega^2} = \varepsilon(\omega) = \varepsilon_b + \left(\frac{f}{\omega_0^2 - \omega^2 - \mathrm{i}\gamma\omega}\right), \tag{2.45}$$

the so called polariton equation. This is an implicit expression for the dispersion relation of the system. In the following, the real part of the dispersion relation for two different optical resonances will be discussed: a dispersionless optical phonon and an exciton with parabolic dispersion. Both examples are given with and without light-matter coupling.

The dispersion relation of the former are discussed first. The non-interacting dispersion relation is shown in Fig. 2.11a: the dispersionless optical resonance is a horizontal line at the resonance frequency ω_0, which will now be referred to as the transversal eigenfrequency of the oscillator ω_T, while $\omega = \mathrm{c}k$ denotes the linear dispersion of a photon in vacuum. Introducing coupling between both systems leads to a splitting of the polariton dispersion into two branches: the lower LPB and the UPB as depicted in Fig. 2.11b. For a better understanding, the course of the dispersion line from low to high energies in Fig. 2.11b will be discussed. Well below ω_T, the polariton behaves like a photon within a medium with a constant dielectric function of ε_s, the static dielectric constant. Approaching the resonance frequency ω_T, the line bends towards the horizontal line of the optical phonon. The bending of the LPB can be understood as the result of the quantum mechanical anti crossing rule for coupled oscillators. Two intersecting dispersion lines avoid crossing once coupling is introduced and therefore establish two

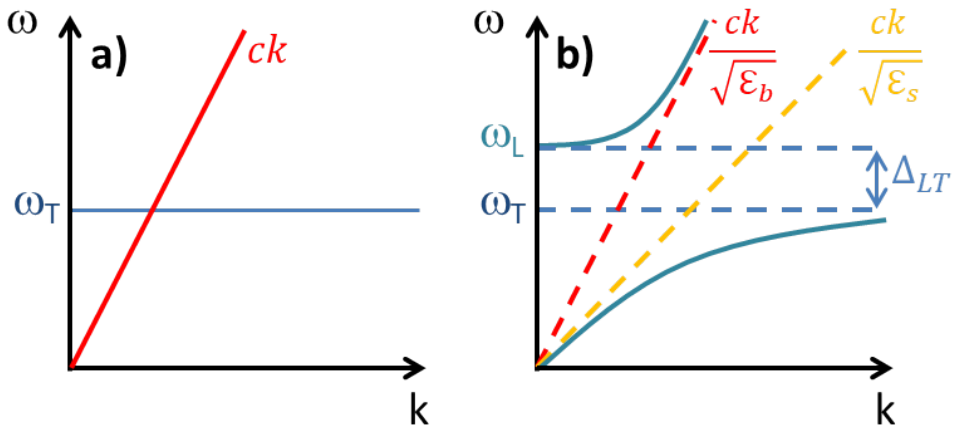

Figure 2.11: Polariton dispersion relation for vanishing (a) and strong light-matter interaction (b) for dispersionless matter resonance, *e.g.*, an optical phonon, for $\gamma = 0$. The dispersion of a photon in vacuum is given as a red line, the dispersion relation of the excited matter state in blue. Without coupling, both lines are unaffected by each other. Light-matter coupling leads to a splitting of the dispersion curve, according to the quantum mechanical anti-crossing principle, where coupling modes of different systems avoid intersections of their dispersion curves. Both the UPB and LPB converge to the photon dispersion far above or below the resonance frequency ω_T, where the LPB mimics the dispersion of the oscillator for high values of k. For vanishing dispersion and no damping of the oscillator, there is no propagating mode between ω_T and ω_L, resulting in total reflection at the material's surface.

new dispersion branches of the system. Without any damping, the dielectric function at ω_T goes to infinity, while no real part of the dielectric function is found shortly above the transversal eigenfrequency of the system, until it recovers at

$$\varepsilon(\omega = \omega_L) = 0, \tag{2.46}$$

with ω_L being the longitudinal resonance frequency of the system. This frequency is connected to a longitudinal pure polarization wave traveling through the system. As a polariton is a mixed state of light and a polarization wave, it must satisfy Maxwell's equations, *e.g.*,

$$\nabla \mathbf{D} = \varepsilon(\omega) \nabla \mathbf{E}. \tag{2.47}$$

Usually, this is used to demonstrate that light is a transversal wave, since this equation is automatically satisfied for $\nabla \mathbf{E} = 0$, *i.e.*, for perpendicular electric field and propagation vector of the electromagnetic wave. However, as shown in Eq. 2.46, longitudinal waves are possible for at $\omega = \omega_L$. The longitudinal nature of these waves add an additional restoring force on the oscillation, hence they are energetically higher than ω_T. The total splitting between the longitudinal and transversal eigenfrequency is given as

$$\Delta_{LT} = \frac{f}{\varepsilon_b \omega_T}. \tag{2.48}$$

For anisotropic materials the that the oscillator strength of a given resonance depends on the angle between the dipole moment of the oscillator and the exciting electric field. Therefore, the observed Δ_{LT} also varies with the angle of the exciting light field. The spectral region between both eigenfrequencies has no propagating light mode. Hence, every incident photon on the sample would be reflected on the surface. This spectral region is called the polaritonic stopband or reststrahlenband. Large-bandgap insulators such as ZnO [65] and organic crystals displaying a characteristic metallic luster [66] exhibit large values of Δ_{LT} due to their immense light-matter coupling. The flat dispersion of optical phonons renders this effect particularly useful for constructing high reflectivity mirrors in the IR regime [67].
The upper polariton branch starts out horizontally at ω_L and bends towards the photon dispersion with a constant dielectric function ε_b. For $\omega >> \omega_L$and $\omega << \omega_T$ the polariton dispersion resembles the dispersion of a photon. These parts of the dispersion are called 'photon like', while the region in vicinity to ω_T is called 'phonon like'. For absorption or emission measurements, a photon in vacuum has to scatter in or out of the polariton dispersion at the surface of the material, *e.g.*, by momentum transfer from the photon to the lattice via acoustic phonons. The likeliness of this event increases with increasing similarity between the polariton dispersion and the photon dispersion. Hence, the total reflection at the surface increases in the vicinity of ω_T, both for incident photons and internal reflection of polaritons.

A different behavior of the dispersion can be seen for the case of an exciton-polariton with parabolic dispersion (fig 2.12). While the UPB remains unchanged, the lower polariton branch extends over the whole energetic spectrum, as it follows the parabolic dispersion of the exciton for high values of k. This results in a propagating mode in the

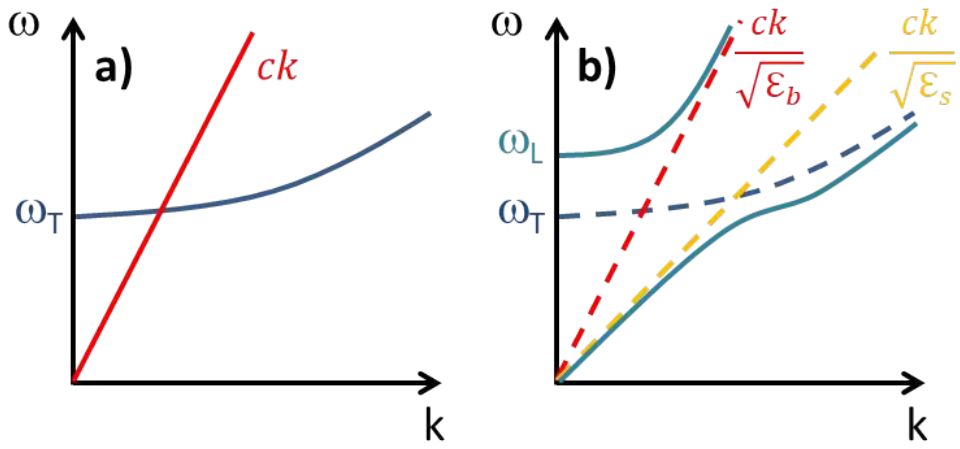

Figure 2.12: Polariton dispersion relation for vanishing (a) and strong light-matter interaction (b) for dispersive matter resonance, *e.g.*, an exciton, for $\gamma = 0$. The dispersion of a photon in vacuum is given as a red line, the dispersion relation of the excited matter state in blue. The LPB at lower values of k and the UPB do not differ from the previously discussed case of a non-dispersive matter interaction. However, there is a propagating mode between ω_T and ω_L, and two propagating modes above ω_L.

polaritonic stopband. Additionally, for $\omega \geq \omega_L$ two propagating polariton modes can be found.

The shape of the exciton-polariton dispersion influences the optical properties of the material, including absorption and emission. For any experiments to be feasible, photons need to scatter from the dispersion curve of a photon in air onto the polariton dispersion at the interface of the material or *vice versa*. This is possible with great efficiency at the photon like parts of the polariton. However, the great differences in momentum in the exciton-like parts of the polariton prevent any polaritons from leaking out of (or photons leaking into) the media. The reflection, internal and external, is strongly increased in those regions. The polariton needs to relax into the photon like parts of its dispersion before any photon can be detected outside of the medium. Near ω_T where the dispersion of the polariton is flat, this relaxation can be achieved by acoustic phonons. Their high momentum combined with low energy are ideal to move horizontally along the dispersion curve. Once the dispersion starts to bend towards more photon like behavior acoustic phonons cannot transport enough energy to follow the steep slope of the dispersion. Optical phonons are needed for further relaxation

to efficiently couple the polariton to the outside world. Since such scattering events are rather rare, it results in a significant bottleneck for polariton emission in the case of strong light-matter coupling, hence the name phonon bottleneck. Furthermore, the polariton is least photon like in the region of the polaritonic stopband. Even though a propagating mode exists, it contributes only weakly to emission and absorption spectra. The reflection remains high, but below unity.

As a consequence, the existence of two propagating modes above ω_L results in two possible transmitted beam paths in the medium, diffracted at different angles. This effect of spatial dispersion, though similar, differs from birefringence as both beams share the same polarization. The energy distribution among both modes varies depending on the photon energy. As a rule of thumb, nearly all photons travel on the UPB for energies ten times Δ_{LT} above ω_L. Since this is not significant for this work, the reader is referred to the available literature for closer investigation, *e.g.*, [27]. The above discussion has completely omitted damping on the system. For increased damping, a propagating mode exists in the stopband even for vanishing dispersion. The reflection consequently decreases with increasing damping. Considering this the total reflection in a polariton stopband is always below unity.

3 Experiments

This chapter will focus on the four experimental setups used to study the optical properties of perylene, PEN, PFP and PEN/PFP heterosystems. The absorption spectra of perylene in the vapour phase are obtained by a set of special gas cells heated to 200° C. A polarization resolved absorption setup with high spatial resolution is used to investigate the excitonic landscape of perylene crystals both in the visible and near ultra violet regimes. The exciton dynamics of all samples are studied via a TRPL streak camera setup with 1.5 ps temporal and 10 µm spatial resolutions to address individual perylene microcrystals. To close out the chapter, the PLE spectroscopy setup used to study the excitation channels of PEN/PFP heterostructures is depicted. As all samples are investigated through a combination of absorption and emission spectroscopy, this chapter is subdivided in two parts addressing the individual absorption and emission experiments, respectively.

3.1 Absorption Spectroscopy

Absorption spectroscopy probes the optical transitions from occupied to higher lying unoccupied electronic states. The investigated transitions are the HOMO-LUMO transition with its vibronic progressions and their corresponding exciton resonances. Hence, all observed signals are in the near IR to near UV region of the electromagnetic spectrum. While absorption can also be calculated from reflection measurements via the Kramers-Kronig relation, all absorption measurements presented here are conducted in transmission geometry. In each case three spectra have to be measured to calculate an absorption spectra: a background spectrum B with blocked beam path at the sample

position to measure ambient light, a reference spectrum R where the transmission of the substrate without the sample is measured to eliminate the spectral shape of the light source and any eventual absorption lines introduced by the substrate, and a transmission spectrum S of the sample itself. In total we obtain the absorption A:

$$A = 1 - T = 1 - \frac{S - B}{R - B}, \tag{3.1}$$

where we background corrected both the R and S by subtracting B. T is the total transmission through the sample. Reflection is neglected in this ansatz as will be discussed later on in chapter 4.

3.1.1 Gas-Phase Absorption Measurements

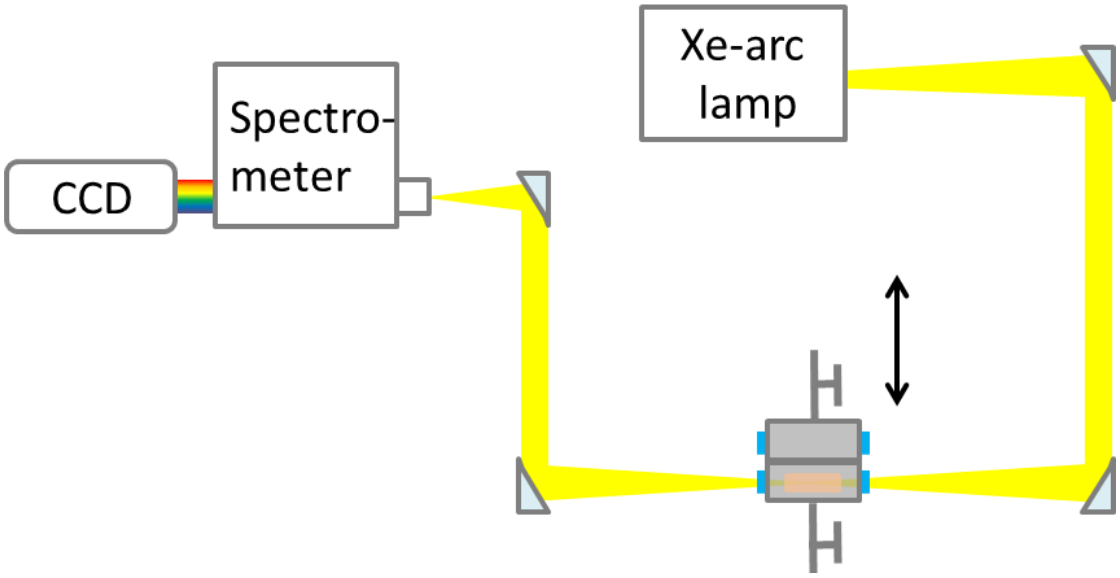

Figure 3.1: The experimental setup used for the absorption measurements of perylen in the vapour phase.

To obtain the single molecular optical properties of any material, one would need to perform spectroscopy on a single molecule or devise experimental strategies to eliminate molecular coupling in an ensemble of molecules, *e.g.*, by incorporating them in a noble gas matrix. Both methods feature enormous experimental challenges. An easy way

to obtain a close approximation of the single molecular properties is by measuring the absorption of the evapourated material. Intermolecular interactions can be disregarded as they are negligible in a diluted gas. However, the spectra will be significantly broadened by the high temperatures necessary for evapouration. As our interest lies in the electronic transitions in perylene and their vibronic progressions, which are well resolvable even at higher temperatures, this tradeoff is of no concern. The experimental setup used is depicted in Fig. 3.1. All focusing optics are reflective in nature (UV enhanced aluminum-coated off-axis parabolic mirrors) to avoid chromatic aberrations and reduce spectral losses in the near UV range. The light of a Xe-arc lamp is collimated and subsequently focused on the gas cell containing the sample. Perylene powder is placed in an aluminum gas cell, which is subsequently evacuated to 10^{-6} mbar to avoid oxidation during the heating process. After evacuation, the cell is sealed and heated to a temperature of 473 K causing The molecules to evapourate. Entrance and exit ports in the cell are equipped with sapphire windows. To avoid resublimation of the sample, the windows are heated separately. For reference, a second identical, but empty, cell is mounted on the same holder parallel to the first. It is possible to move either one into the beam path thus enabling the measurement of accurate reference spectra. The transmitted light is collected and focused on the entry slit of a grating monochromator and detected by a thermoelectrically cooled scientific silicon based charge-coupled device (CCD) camera (Roper Scientific, HAM 1024x128). The data is processed using self-written LabView software.

3.1.2 Linear Absorption Spectroscopy in the Visible and Ultraviolet Range

Figure 3.2 shows a sketch of the setup used for the absorption measurements in the UV/VIS spectral range on the perylene crystals discussed in chap. 4.1. The setup meets the requirement of high spatial resolution for polarization dependent measurements of µm-sized single crystals deep into the UV range. To achieve this goal, all involved focusing optics are reflective in nature thus avoiding chromatic aberration. The only non-reflective components, the sapphire windows of the cryostat and the wire grid beam splitter, show no significant absorption above 250 nm. A pinhole of 100 µm in diameter

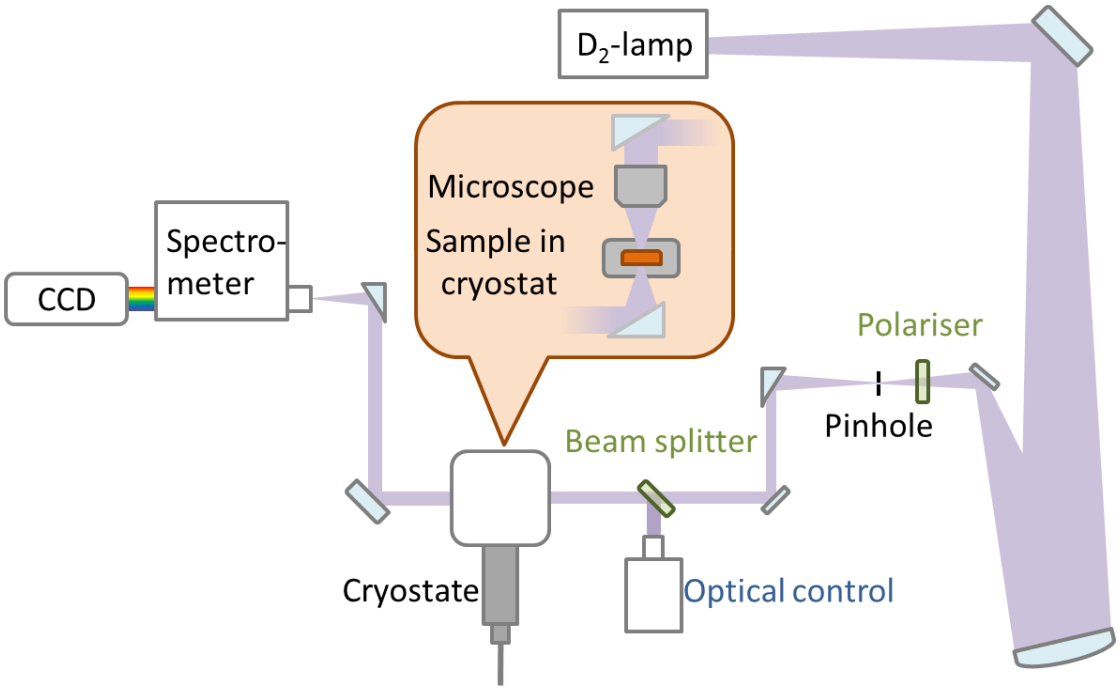

Figure 3.2: Experimental setup for ultraviolet sensitive absorption spectroscopy.

is placed in the focus point of a parabolic mirror to create a homogeneous and point-like light source, increasing the spatial resolution of the experiment. The setup is built on two levels connected by a periscope containing the sample within a helium flow cryostat. The red inlay in Fig. 3.2 shows a schematic depiction of this periscope: the inciting light is focused onto the sample by a Schwarzschild type reflective microscope objective (36 fold magnification). A parabolic mirror collects the transmitted light, which is spectrally dispersed in a grating monochromator and detected by a cooled scientific silicon based CCD camera (Roper Scientific, HAM 1024x128). The data is read out using self-written LabView software. To determine the exact position of the light spot on the sample, an ultra-thin beam splitter deflects the light back reflected from the sample surface into a complementary metal-oxide-semiconductor (CMOS) camera (Microsoft LifeCam Studio, stripped of all optical components) for direct optical control. The beam splitter is removed during the actual measurements.

3.2 Photoluminescence Spectroscopy

PL spectroscopy is a tool used to investigate the relaxation channels and dynamics of the excited states populated by a previous optical excitation, provided that a radiative relaxation channel for those states exists. Additionally, some excited states are invisible in absorption spectroscopy, especially when their creation is connected with a lattice deformation, which is too slow to coherently influence the absorption of a photon. These states may form after excitation and may be visible in the emission spectra in the form of strongly red-shifted PL signals. Time resolved emission measurements compliment these findings with insights in the decay dynamics of all different states. The observed decay is almost always a superposition of different bright and non-radiative decay channels. However, baring time or density dependent decay channels like saturating trap states or exciton-exciton annihilation, the dynamics of the PL intensity is a direct mirror of the occupation density of the excited states investigated. Separating the influence of different decay channels on the observed emission dynamics is not always possible within simple TRPL measurements.

3.2.1 Time-Resolved Photoluminescence Spectroscopy

All time-resolved data presented in this thesis is obtained by the streak camera setup depicted in Fig. 3.3. For optical excitation of the samples, a titanium-sapphire laser (Ti:Sa) system (Spectra Physics 'Tsunami', 78 Mhz repetition rate, $\tilde{1}$00 fs pulse length) [68] tunable from 720 up to 1100 nm and optically pumped by a frequency doubled neodymium-doped yttrium aluminium garnet (Nd:YAG) laser (Spectra Physics 'Milennia X', 532 nm) is used. Pulsing is achieved by self-locking exploiting the Kerr effect [69]: a correctly aligned cavity will cause the laser to start pulsing, increasing the electric field strength in the Ti:Sa crystal during the pulse significantly when compared to continuous wave operation. This elevated field strength changes the local dielectric function of the crystal in a pattern resulting in a focusing effect: the so called 'Kerr-lens'. Focusing the beam to even smaller volumes further increases the local field strength and therefore the stimulated emission during the pulse. Hence, the pulsed mode takes over all gain of the crystal at the expense of the continuous mode, thus stabilizing itself. To compensate

the pulses for dispersion accumulated while traveling through the cavity, two prism pairs are integrated in the cavity.

As all materials investigated in this thesis need to be pumped at wavelengths below

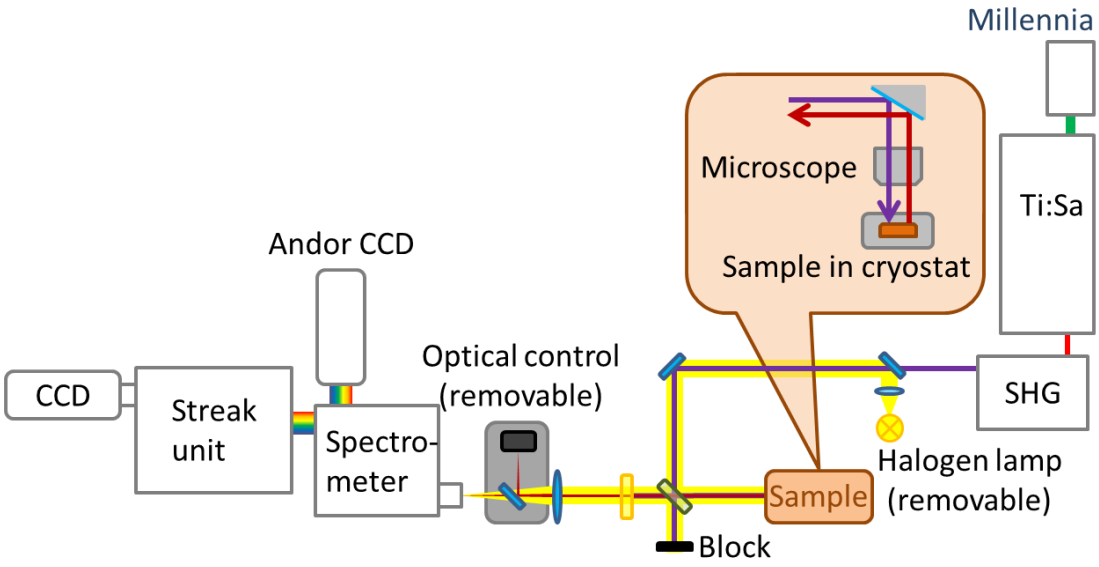

Figure 3.3: A schematic depiction of the streak camera setup for TRPL.

700 nm for one-photon excitation, the non-linear optical properties of a barium borate (BBO) crystal are exploited for second harmonic generation (SHG) of the fundamental Ti:Sa laser light. The laser beam is focused on the BBO crystal by an off-axis parabolic mirror with a focal length of 0.5 inches to achieve high local field strength within the crystal. This is necessary as frequency doubling scales with the local field strength squared. Due to intrinsic asymmetry of the crystal, frequency doubled photons are generated. Within a certain spectral window, the spectral dispersion of the BBO is flat. Hence, the frequency doubled and fundamental laser pulses propagate with the same speed in the same direction. As the fundamental and second harmonic pulse are in phase, all further generated second harmonic light is in phase with previously generated frequency doubled photons, amplifying the SHG pulse along the whole path through the crystal. This is called phase matching. It is most prominent in the used BBO crystal for a fundamental wavelength of 800 nm. For significant deviations from the optimum, phase matching is lost and increasingly destructive interference between previously created frequency doubled photons gradually decreases the conversion ef-

ficiency. For the optimal wavelength of 800 nm, 25 % of the photons are frequency doubled to 400 nm: the main excitation wavelength for all measurements presented in this thesis. The frequency doubled laser passes through an attenuator, if necessary, and is focused on the sample by a Schwarzschild type microscope objective (36 fold magnification). The actual spot size on the sample depends on beam divergence and the diameter of the exciting laser. Usually, a spot size approximately 10 µm in diameter is achieved. Excitation and detection is carried out in confocal geometry: the exciting laser is focused by the same microscope objective used for collimating the emitted photons in a back scattering geometry. To maximize light collection from the sample, the beam splitter is chosen to transmit 70 % of the incident light, while 30 % is reflected. This way a majority of the excitation power is lost, but the majority of the actual luminescence is not. However, 10 mW of power for 400 nm is still measured directly at the sample, which is sufficient for the measurements of PEN and PFP, and enough to damage the perylene crystals if not attenuated. As all emitted photons from the sample have to pass through the beam splitter on their way to the detector, a higher ratio of transmission is preferable to increase detection efficiency.

The PL is separated from residual pump by a long pass filter and focused on the entrance slit of the monochromator (Oriel Instruments MS260i Imaging $1/4$ m Spectrograph) by a low-dispersion CaF_2 lens. Similar to the absorption experiment, a removable mirror can be positioned in front of the monochromator, which deflects the light onto a small CMOS camera (Microsoft LifeCam Studio, stripped of all optical components) positioned in the focal plane of the lens. Therefore, a direct monitoring of the sample and the laser position is possible. Two exit slits of the monochromator are available. One is connected to a cooled scientific CCD camera (Andor DU 440 BU) read out by self-written LabView software for non-time resolved measurements. The other is connected to the streak camera (Hamamatsu G9207-256W, S20 streak tube) for temporal resolution. An in-depth review of the inner workings of a streak camera can be found in Ref. [70]. This setup provides good spectral response between 350 nm and 850 nm and a temporal resolution of 1.5 ps. The data is collected via a PC using Hamamatsu HPDTA v9.1 software and self-written labView software for further evaluation.

The setup can be easily modified for reflection measurements. A removable mirror couples the light of a halogen lamp into the beam path before the beam splitter, enabling

reflection measurements in the visible and near IR range using the same detection path described above.

3.2.2 Photoluminescence-Excitation Spectroscopy

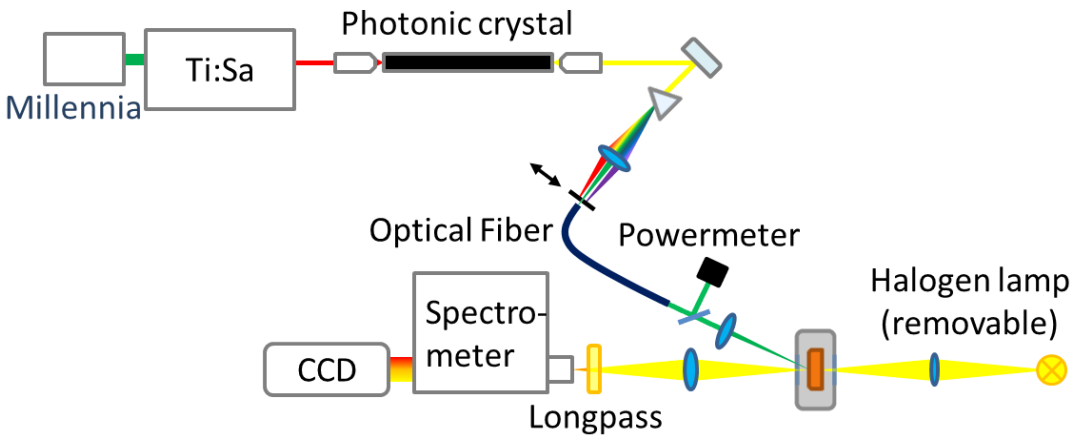

Figure 3.4: The PLE setup used in this thesis to investigate the excitation channels of the interfacial PEN/PFP state.

To gain insight into the excitation channels of the interface state observable in PEN/PFP heterosystems, the PLE experiment depicted in Fig. 3.4 was used. Akin to the TRPL setup, a Ti:Sa laser is used for excitation. However, instead of a BBO crystal for SHG, a photonic crystal fiber (NKT Photonics, Femtowhite 800 PCF) is used for white-light supercontinuum creation. The Ti:Sa beam is focused on the input facet of the photonic fiber using a microscope objective. The fiber itself is mounted on a piezo driven 3D-stage to enable high precision positioning: the photonic crystal in the fiber itself is only 1.6 µm thick [71]. The resulting white-light is collimated by a second microscope objective and guided through a prism, which disperses it into its spectral components. As the multicolored dispersed beam passes through a lens, different wavelengths are focused to a different point in the focal plane of the lens. Hence, a simple movable slit used as a mask can pick a certain wavelength from the white-light spectrum by suitable positioning in the focal plane. The light passing through the slit is captured by an optical fiber, which guides the beam through a focusing lens towards the sample,

which is mounted in a closed cycle helium cryostat. A small portion of the exciting light is deflected by a beam splitter towards a powermeter. This enables us to determine the relative intensity of the different laser wavelengths. This is neccesary to correct the measured PL intensities for the differences in excitation power. The emitted light is captured by a lens and passed through a dielectric longpass filter to eradicated scattered pump light. The light is spectrally resolved by a grating monochromator and measured using a liquid nitrogen cooled scientific CCD camera (Roper Scientific, 1340X100 pixels). The data is read out and evaluated by self-written LabView software. The recorded PL spectra for each excitation wavelength are integrated in the spectral region of the PL signal of interest. The resulting integrated intensity is corrected for the relative intensity of the exciting laser pulse. If this corrected intensity is plotted as a function of excitation wavelength, a clear picture of the absorption peaks, which contribute to the measured PL, is obtained. The signal strength is now determined by the absorption strength of the sample at a specific wavelength multiplied by the coupling efficiency of the absorption channel to the emitting state at the detection wavlength and the quantum yield of this state.

4 Results

Two different acene-based material systems are investigated in this thesis: molecularly smooth perylen single crystals of different polymorphs and PEN/PFP heterosystems with varying molecular alignments at the heterointerface. Both are prime examples for the influence of molecular packing on the optical properties of an aromatic molecular semiconductor. Furthermore, use perylene as a model system to benchmark state of the art calculations, which will contribute to the development of more predictive theory to describe molecular semiconductor systems.
The well defined PEN/PFP structures are ideal for investigations of the nature of the observed interface states, where astonishing deviations from a simple charge-transfer exciton picture are observed (see 2.2.4).
All samples investigated have been grown by the group of Prof. G. Witte. The groups of Prof. L. Kronik and Prof. J. B. Neaton provided calculations of the bandstructure and excitonic system of perylene. TRPL in the infrared region on the PEN/PFP heterosystems are performed in the group of Prof. M. Oestreich. All other optical measurements and the interpretation of the results are the main subject of this thesis.

4.1 The Excitonic System of Perylene Crystals

4.1.1 Molecular Properties and Crystalline Structure

Perylene and its derivatives have a long history of commercial application as color pigments, *e.g.*, in the automobile industry. More recently, perylene related molecules

have become of interest for OPV applications, [72, 73] due to strong light-matter interaction of the perylene core [74, 75, 76, 77, 78]. Being a polycyclic aromatic molecule perylene has four conjugated carbon rings and takes the shape of two naphthalene molecules linked together, as depicted in Fig. 4.1. Fig. 4.1 displays the optical prop-

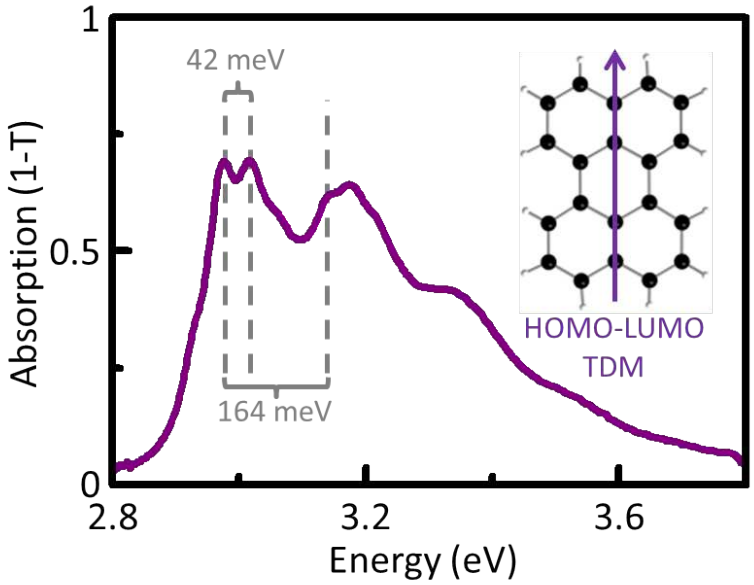

Figure 4.1: Absorption spectra of vaporized perylene molecules at 200°C. The two most pronounced vibronic progressions are labeled in grey. A depiction of the perylene molecule and the transition dipole moment of the HOMO-LUMO transition (purple arrow) is given for further reference.

erties of evapourated perylene. Due to weak molecular interaction, the spectrum is a good approximation for the single molecular properties of perylene. Although the high temperature of 200°C needed for evaporation leads to broad peaks, two pronounced vibronic replica are clearly visible: one at 42 meV and one at 164 meV above the HOMO-LUMO transition at 2.98 eV, as indicated by the gray dashed lines, as known from the literature [79, 80, 81]. Higher vibronic orders and linear combinations of both vibrons are also observed at higher energies. Furthermore, Fig. 4.1 displays the perylene molecules the transition dipole moment for its HOMO-LUMO transition, aligned parallel to the long molecular axis. The later will be important for any discussion of perylene in the solid state, as it dictates the anisotropic response of the crystals.

In the solid state, Perylene exhibits significant carrier mobility [82] and oscillator strength of the excitonic system [83]. Bulk crystals are found in two crystalline polymorphs: the monomeric β and the dimeric α phase. Both are distinguishable by their molecular packing motif and characteristic crystalline shape, as depicted in Fig. 4.2 [20, 84].
Crystals of the α-phase grow almost rectangular in shape, while the β-phase results in

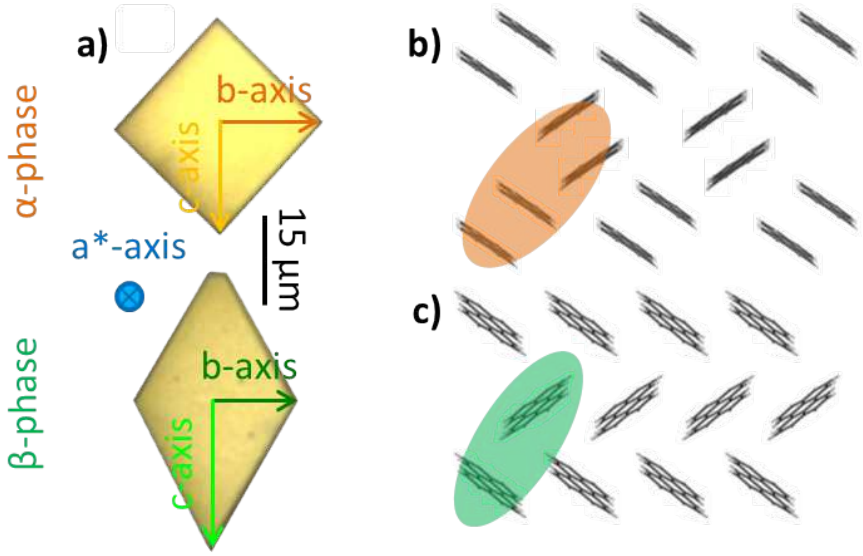

Figure 4.2: Microscope image of both crystalline polymorphs of perylene grown by resublimation [20] (a) and the corresponding crystalline structure of the α (b) and β-phase (c). The colored arrows in subfigure (a) display the respective crystalline axes and are universal for subfigures a-c. The unit cell of the α-phase contains for molecules, marked in orange, while only two molecules are found in the unit cell of the β-phase as marked in green.

clearly distinguishable rhombic shaped crystals, see Fig. 4.2a. The crystaline structure of the β-phase is the simpler of the two: perylene molecules form a herring-bone structure with two molecules in the unit cell, as depicted in Fig. 4.2c. A dimeric herring-bone configuration is found for the α phase. Instead of individual molecules, dimers consisting of two parallel perylene molecules form a herring-bone structure, resulting in four molecules in the unit cell (Fig. 4.2b). The long molecular axis of the molecules in both crystalline phases stands almost upright with regard to the sample [20]. Hence, only a fraction of the actual oscillator strength is addressable in optical spectroscopy as the sample is probed perpendicular to the substrate. More details on the crystalline

structure are found in Ref. [20].
Liquid-mediated growth under ultra-high vacuum conditions yield, depending on the growth parameters, perylene crystals of exceptional quality for both polymorphs [20]. Single-crystalline platelets of over 100 µm in diameter are achievable by this method. Atomic force microscopy reveals them to be only a few 100 nm in thickness and molecularly smooth on the surface [20]. Hence, high-resolution polarization resolved absorption spectroscopy in transmission geometry is possible without any notable influence of defect states. X-ray spectroscopy on those crystals unambiguously correlates the macroscopic crystalline shape and the microscopic crystalline axes (Fig. 4.2). Previously, the high absorbance of the crystals often rendered direct transmission measurements impossible. As such, reflection measurements using Kramers-Kronig transformation had to be used, with all its related limitations [85, 86, 40]. This is not necessary for the thin perylene platelets investigated in this work.

4.1.2 Polarization Resolved Absorption: Experiment vs. Theory

The extraordinary sample quality and the resulting high-resolution absorption spectra allow a thorough investigation of the impact of crystalline polymorphism on the excitonic system through experiment and theory. To this end, *ab initio* calculations have been performed based on the Greens function and screened Coulomb potential W approximation (GW) plus Bethe-Salpeter equation (BSE) to model the excitonic system of both α and β-phase perylene. The GW quasiparticle energies have been computed starting from Kohn-Sham density functional theory (DFT) orbitals and eigenvalues [87, 88, 89, 90]. The resulting orbitals are used to solve the BSE and to compute the optical properties of the excitons [91, 92]. In its full form, the BSE takes the form of a matrix

$$\begin{pmatrix} A & B \\ -B & -A \end{pmatrix} \begin{pmatrix} X^S \\ Y^S \end{pmatrix} = \Omega^S \begin{pmatrix} X^S \\ Y^S \end{pmatrix}, \tag{4.1}$$

where X^S and Y^S are the new eigenstates of the system, Ω^S the exciton energies and A and B are coupling matrices constructed from the GW quasiparticle energies and Kohn-Sham orbitals. The off-diagonal elements B couple excitation to de-excitation. To gain computational efficiency, they are often ignored, resulting in the so called Tamm-Dancoff approximation (TDA). The quality of the obtained experimental results allow a direct comparison on full BSE and TDA calculations.

An overview of the measured and calculated spectra for both perylene polymorphs is given in Fig. 4.3. Following the grey dashed lines in Fig. 4.3 reveals the quality of the calculations: Every peak observable in the experiment not associated with a vibronic progression (marked with a ν, from Ref. [93]) is reproduced with unprecedented accuracy considering the uncertainty of the calculation, which is usually around 100 meV. While both the TDA and the full-BSE results are within this margin of error, a better match between experiment and theory is found for the β-phase (Fig. 4.3d) without the TDA, especially at higher energies. The only significant deviation is the missing peak in the β-phase, label 'sb' in Fig. 4.3b. This peak is assigned to a polaritonic stopband (see 2.2.7), as observable in, *e.g.*, quasi one-dimensional polymer chains crystals and TCNQ crystals [94, 95, 96, 97]. The experimental absorption spectra have been obtained in transmission geometry and are displayed as $1-T$, where T is the transmission measured through the sample. [1] Hence, following the fundamental relation $A+R+T=1$, where A is the absorption and R the Reflection on the surface of the sample, Fig. 4.3a,b display A+R. However, the DFT calculations only show the position of the absorption peaks. A purely reflective signal would be included in neither the TDA nor the full BSE calculations. Hence, the $1-T$ results are compared to $\Delta R/R$ measurements, see Fig. 4.4. To interpret our results, the actual properties measured need to be known. In both cases, the measured quantity is composed from the transmission T_P through the perylene crystal and the reflection on the surface of the crystal R_0 or at the interface between the crystal and the substrate $R_{Q/S}$. Ignoring multiple reflections in the sample, the total measured signal in transmission geometry, as symbolized by the green arrow in Fig. 4.4a, is

$$I_0 T_Q T = I_0 T_Q (1-R_0)(1-R_Q) T_P. \tag{4.2}$$

[1] Ignoring multiple reflection in the sample.

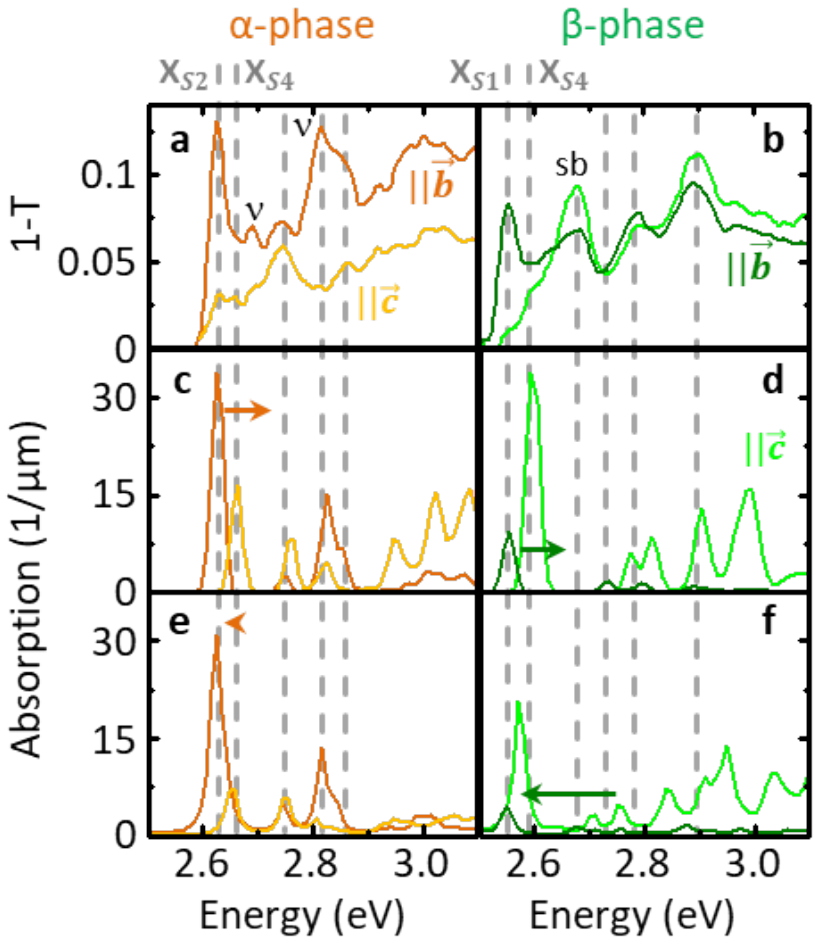

Figure 4.3: Measured (a,b) and full-BSE (c,d) and TDA calculated (e,f) polarization resolved absorption spectra of perylene crystals. All measurements are performed at a temperature of 5 K. The results for the α-phase are given in the left column (a, c, e; orange), while the corresponding results for the β-phase is on display in the right column (b, d, f; green). The gray dashed lines highlight the position of the peaks in the experimental spectra for easier comparison to the calculations. All calculated spectra have been shifted to match the optical band gap determined by the experiment, as indicated by the direction and length of the colored arrows. Curves in darker colors denote the optical response polarized along the b-axis, while lighter colors give the response polarized along the c-axis. Vibronic progressions are marked with a ν. Exceptional agreement of both measured and calculated spectra is found. Only one peak, labeled 'sb' is not reproduced by the calculations, which is assigned to a polaritonic stopband.

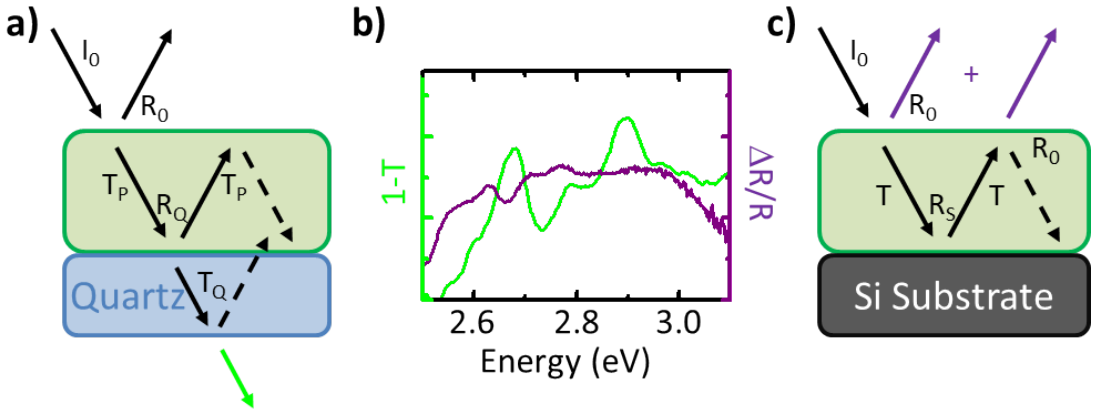

Figure 4.4: Beampath in transmission geometry (a) $1-T$ and $\Delta R/R$ spectra (b) and beam path in reflection geometry (c) for a β-perylene crystal on a quartz or silicon substrate, respectively.

Here, I_0 is the intensity of the incident light field and T_Q the transmission through the whole quartz substrate, including internal reflection. Equation 4.2 is divided by $I_0 T_Q$ obtained in good approximation by a transmission measurement of just the quartz substrate to obtain T. $1-T$ is plotted in Fig. 4.4b and Fig. 4.3a and b as an approximation for the actual absorption of the sample. As $1-T$ increases with decreasing T_P and increasing $R_{0/Q}$, a purely reflective and a purely absorptive feature both result in a peak in the $1-T$ spectra. No distinction can be made.
The corresponding measured signal in reflection geometry, as symbolized by the purple arrow in Fig. 4.4c, is given by

$$I_0 R = I_0 \left[T^2 R_{Si} + R_0 \left(1 + T^2 R_{Si} \left(R_0 - 2 \right) \right) \right] T_P. \tag{4.3}$$

Here, R is the total reflectivity of the whole sample ignoring multiple reflections. R clearly increases with T. The factor $1 + T^2 R_{Si} \left(R_0 - 2 \right)$ now determines if R increases or decreases with R_0. The reflection at the silicon air interface is roughly 0.4 in the visible regime. As the refractive index of perylene is between air and silicon, R_{Si} should be smaller than that. Hence, $T^2 R_{Si} << 0.4$ holds true. As a result $1 + T^2 R_{Si} \left(R_0 - 2 \right)$ is

positive and R increases with R_0. To eliminate the spectral shape of the lamp and the spectral features introduced by the reflection of the substrate

$$\frac{\Delta R}{R_{Si}} = \frac{R_{Si} - R}{R_{Si}} \tag{4.4}$$

is calculated and plotted, which decreases with R_0 and increases with purely absorptive features. As the feature at labeled 'sb' is a peak in $1 - T$, but a clear local minimum in $\frac{\Delta R}{R_{Si}}$ measurements, one can conclude that this feature is mainly reflective in nature. This supports or interpretation of a polaritonic stopband, as this is a region with increased reflection, see chap. 2.2.7.

To further validate our interpretation, the width of the stopband Δ_{LT} is estimated using the Eq. 2.48 by comparing it to known material systems, in this case to the organic molecular crystal 1,5-bis(dimethylamino)pentamethinium perchlorate (BDP) [66]. All relevant values for BDP are found in Ref. [66]: f=3.31, $\Delta_{LT} = 1.09\ eV$, $\varepsilon_b = 1.5$, and $\hbar\omega_T = 3.1\ eV$. Note that f is the dimensionless oscillator strength, which is proportional to the full oscillator strength used in Eq. 2.48. The corresponding values for perylene are: f=0.44 [83], $\varepsilon_b \approx 1.9$ (see Fig. 4.5), and $\hbar\omega_T = 2.55\ eV$. To estimate Δ_{LT} for β-phase perylene, one calculates

$$\frac{f}{\varepsilon_b \omega_T} \tag{4.5}$$

for both BDP and β-phase perylene to calculate the ratio between the width of both polaritonic stopbands, which is found to be roughly 14 %. This leads us to an estimated stopband width of approximately 140 meV, which would reproduce the observed spectra with significant accuracy. With the reflective nature and correct width, there are strong indications that the feature labeled 'sb' is a polaritonic stopband. Such a feature is not observed in the α-phase, as vibronic progressions and new excitonic features are found within the stopband. Hence, it cannot be unambiguously identified.

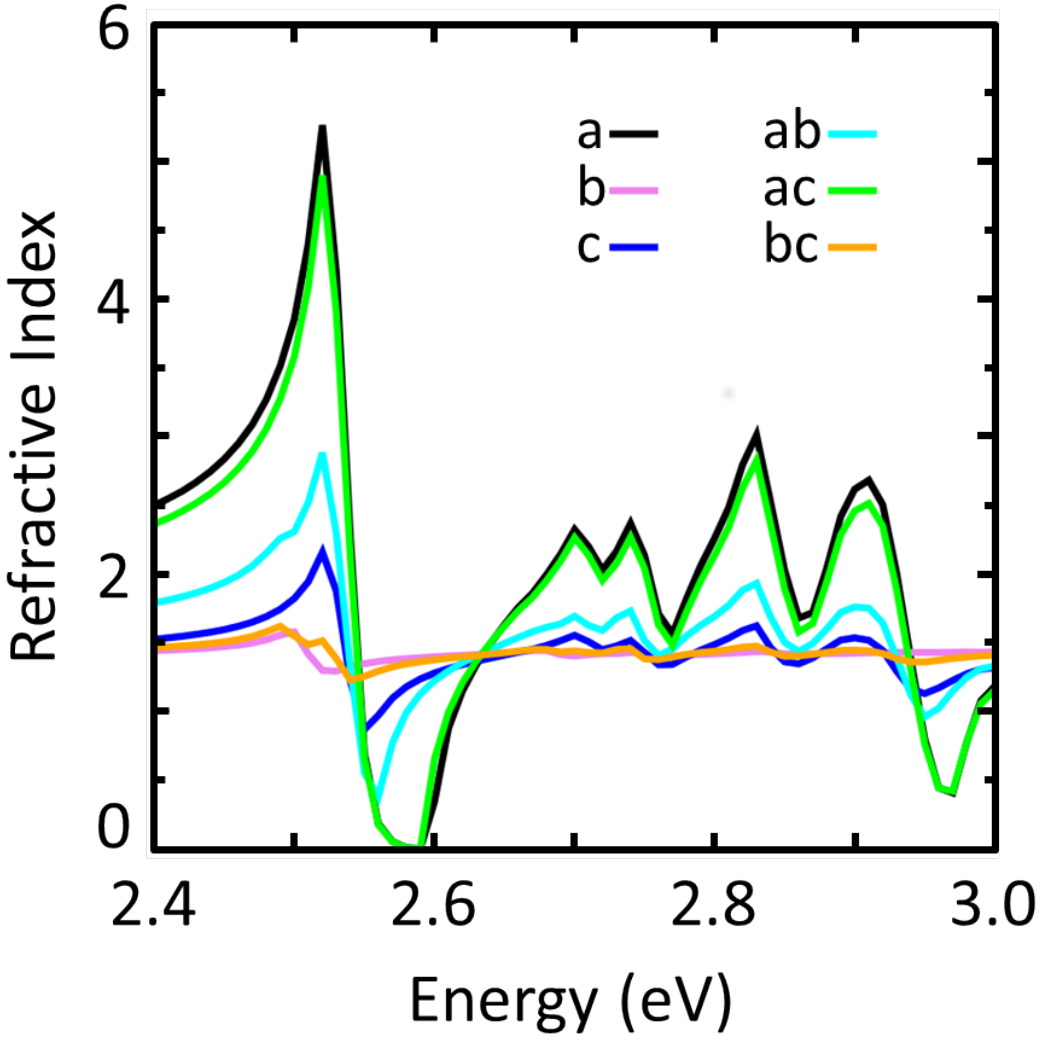

Figure 4.5: Calculated real part of the index of refraction of β-phase perylene along the all crystalline axes and planes. As the multiple excitonic resonances are not well separated, the background dielectric function in the bc-plane can only be estimated using $\varepsilon_b = n^2$ to be 1.9.

4.1.3 Calculated Bandstructure and Exciton Wavefunction

The single particle bandstructure of both α and β-phase perylene is calculated to gain additional insight into the anisotropy of the optical properties of solid-state perylene,

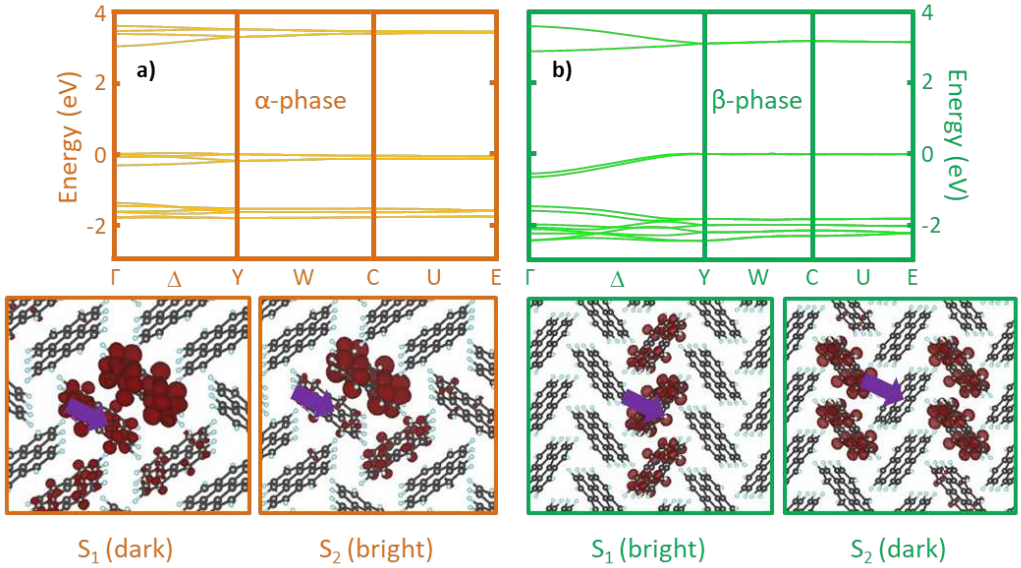

Figure 4.6: Single particle bandstructure and lowest lying exciton wavefunctions S_1 and S_2 for the hole at the fixed position indicated by the purple arrow for α-phase (a) and β-phase (b) perylene crystals. Significant dispersion is only found for the b-axis polarized excitations in the β-phase, due to π-stacking observed in this direction. While the exciton wave-functions are rather localized on a single dimer for the α-phase, the bright exciton state of the β-phase displays delocalization along the b-axis, again in congruence with increased intermolecular interaction in this crystalline direction due to π-stacking.

see Fig. 4.6. Vanishing dispersion is found along most paths through the Brillouin-zone. However, some dispersion is found in the Δ-direction, which corresponds to excitation along the b-axis. This is especially pronounced for the β-phase. These findings are correlated to the molecular packing of the crystals. As displayed in Fig. 4.2c, the smallest separation between face-on stacked parallel molecules is found along the b-axis. As previously discussed in chap. 2.1.2, intermolecular interaction between neighboring molecules is significantly increased by π-stacking, *i.e.*, the overlapping of the out of plane π-orbitals [98, 99]. As band dispersion is a direct reflection of intermolecular interaction, an increased dispersion along the b-axis in the β-phase is expected. Such an unbroken chain of π-stacked molecules is not observed in the α-phase. Due to its dimeric structure, strong molecular interactions are found between neighboring molecules within an unit cell only. This directly translates to diminished

dispersion when compared to the monomeric β-phase.

The distinguished role of π-stacking is also visible in the exciton wavefunctions shown

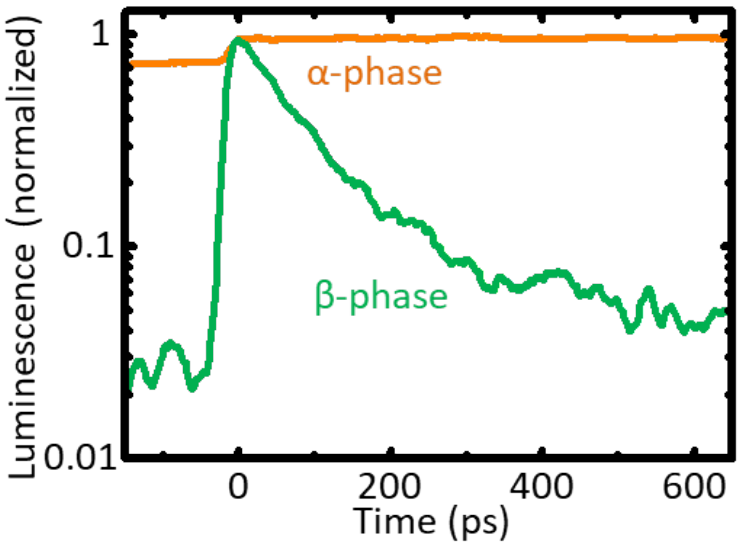

Figure 4.7: Unpolarized TRPL measurements of α (orange) and β-phase (green) perylene crystals performed at room temperature.

at the bottom of Fig. 4.6a and b. Both the dark S_1 and bright S_2 exciton of the α-phase are strongly localized on a single perylene dimer. In contrast, the bright exciton state S_1 in the β-phase shows significant delocalization along the π-stacked b-axis. This has implications on the optical properties of the crystals. Flat bands are linked to long lifetimes by Heisenberg's uncertainty principle. Figure 4.7 shows the unpolarized TRPL measurements for α and β-phase cyrstals. The localized α-phase shows long lived excimeric PL [52, 100], while the exciton lifetimes observed in the β-phase are significantly shorter.

In conclusion, the studies on perylene demonstrated the importance of combining high-quality samples with well known crystalline structure, ab initio calculations and high resolution optical spectroscopy. The measured absorption spectra could be replicated with astonishing accuracy. Vast differences in the crystalline structure of both polymorphs, especially regarding π-stacking along the b-axis, have visible implications on the measured optical properties, the calculated bandstructure, exciton wavefunctions

and by extension, on the exciton dynamics. The presented studies serve as an significant step towards a full understanding of more complex aromatic systems and the general interplay between structure and optoelectronic properties.

4.2 Electronic States at the Pentacene/Perfluoropentacene Interface

The previous section investigated how different polymorphs of the same molecular semiconductor system influence the observed optical properties. This section will demonstrate the impact of molecular packing and orientation on the interface related electronic states in PEN/PFP heterosystems. Using the method of TRPL, seven different samples have been examined, as presented in Fig. 4.8. All samples are grown under high-vacuum conditions by molecular-beam deposition. The unitary samples are 20 nm thick for accurate comparison to the 40 nm thick heterosystems. Both PEN and PFP are grown with upright molecular orientation and lying molecular orientation relative to the substrate. For easier reference, the upright molecular orientation is called 'standing' and the lying molecular orientation 'lying'. Standing PEN adapts the so called thin film phase [101] (Fig. 4.8a), while lying PEN grows in the so called Siegrist phase [102] (Fig. 4.8b) with the long molecular axis of the molecules virtually aligned parallel to the substrate [103]. Similarly, two different polymorphs are observed for PFP: the bulk-phase for the standing samples [104] (Fig. 4.8c) and the π-stacked polymorph for the lying samples [105] (Fig. 4.8d). Additionally, three heterosystems are grown. One is an equimolar intermixture of upright PEN/PFP (Fig. 4.8e). The two remaining samples are layered samples of 20 nm of PEN grown on 20 nm of PFP, which will be referred to as heterostacks. The first is a stack of standing (Fig. 4.8f), the second of lying PEN and PFP (Fig. 4.8g).

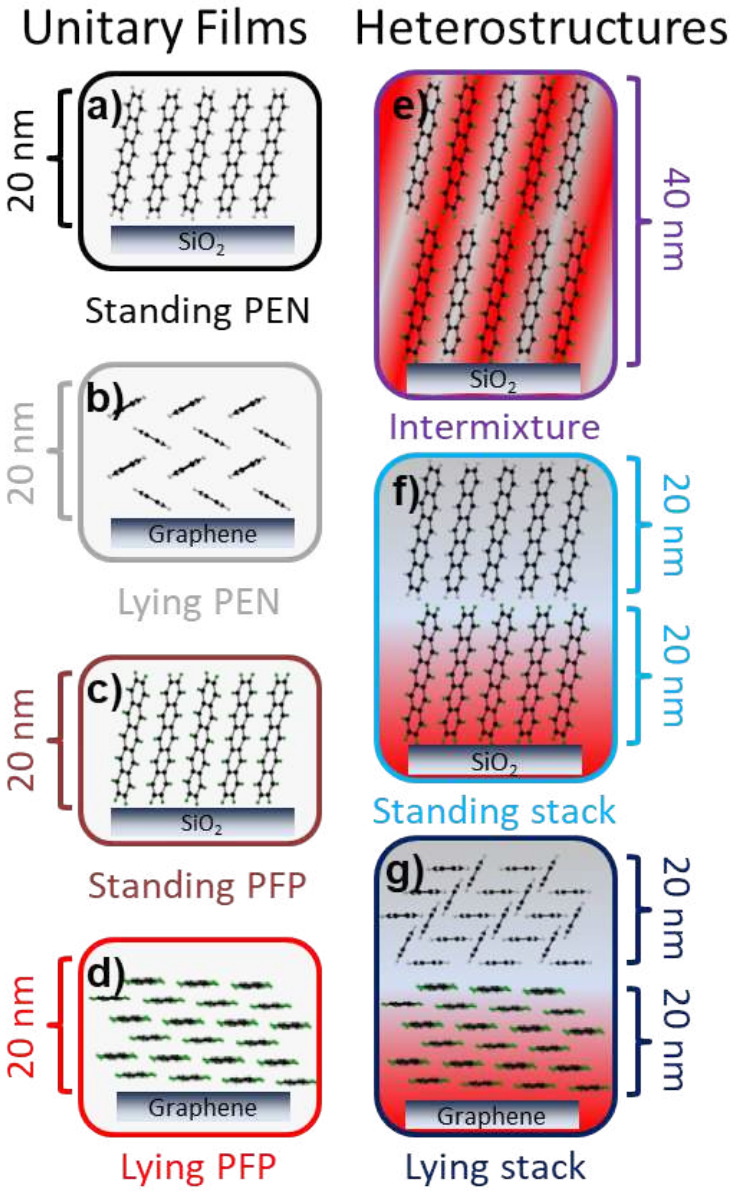

Figure 4.8: Schematic depiction of the investigated unitary PEN and PFP samples as well as the stacked and intermixed PEN/PFP heterosystems. The color code for the seven samples introduced in this figure is universal for the rest of this work.

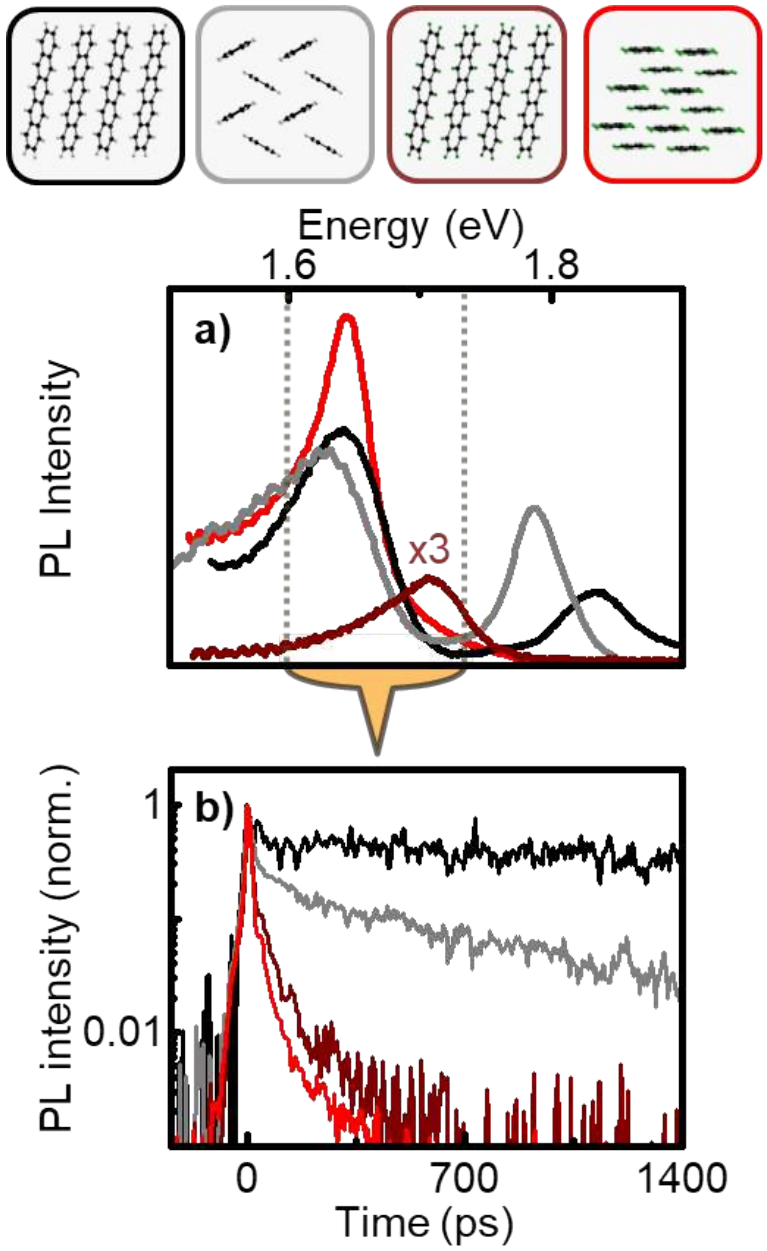

Figure 4.9: Emission spectra (a) and exciton dynamics of the lower energy emission (b) of unitary PEN and PFP films. Small diagrams of the sample structure is given on the top for reference, color coded to match the corresponding curves in subfigures (a) and (b).

4.2.1 Optical Properties of the Unitary Samples

An accurate investigation of the heterosystems requires knowledge of the properties of the constituent layers. Thus, the description of the material system begins with the

unitary films. PL spectra and TRPL transients of these samples are presented in Fig. 4.9. Unless otherwise stated, the excitation wavelength for all emission measurements is 400 nm and all measurements are performed at cryogenic sample temperatures of 5 K. Both PEN structures display two distinct emission peaks: the free exciton emission around 1.8 eV and the self-trapped exciton emission at 1.645 eV [106]. The energy difference of the free exciton line between the standing and lying film is reproduced by absorption measurements in the literature [107, 108]. No self-trapped exciton is found in any of the two PFP samples. The standing film shows extremely weak PL at 1.71 eV, scaled by a factor of three in Fig. 4.9 for better visibility. In contrast, the signal of the lying sample is found at 1.645 eV, more intense by a factor of twelve. The spectral shift between both samples can be reproduced in absorption measurements, see Fig. 4.10. The difference in intensity is attributed to the difference in absorption at our exciting wavelength of 400 nm (3.1 eV): as there is some absorption of the lying sample at this energy (Fig. 4.10), almost none is observed in the standing sample [108, 109]. Interestingly, the PFP emission in the lying sample is energetically degenerate with the self-trapped emission in the PEN samples. As a result, distinguishing PFP and self-trapped PEN related signals in the spectrum of a lying heterostack is impossible.

Thus, time-dependent measurements of the lowest lying emission lines of all four samples are performed. Both PFP samples show fast PL decay, dominated by singlet fission [60]. The slightly faster dynamics of the lying sample (15 ps vs. 20 ps in the standing sample) can be explained by enhanced singlet fission efficiency due to its shorter π-stacking distance and more suitable slip-stacking of the molecules [105, 110]. In strong contrast, the self-trapped emission of both PEN samples approach the nano second regime. This makes the carrier dynamics a useful tool to distinguish between PFP and self-trapped PEN emission, as one almost completely decays within the first 100 ps and the other is still visible after a couple of nano seconds. For a comprehensive summary of all observed exciton lifetimes of all samples investigated in this chapter, see table. 4.1. A depiction of the lowest lying singlet and triplet excitons of both standing PEN and PFP is given in Fig 4.15b.

4.2.2 Emission spectra and Time-Resolved Photoluminescence of the heterosystems

The knowledge on the unitary films enables the investigation of the heterosystems. The emission spectra of all three samples and the absorption of the intermixed sample is displayed in Fig. 4.11. As becomes apparent by comparison with the dashed lines, representing the energetic positions of emission peaks in the unitary films (see Fig. 4.9), emission lines of the unitary samples are observable in the heterostacks. A notable exception is the emission signal of the standing unitary PFP, which is not observed in the corresponding heterostack. This could be a result of its relativly weak oscillator strength, but considering that not the slightest shoulder is found at 1.71 eV, internal conversion to the interface or trap states seems more likely. As previously reported, no corresponding emission is observable for the intermixed sample at cryogenic temperatures [23, 111]. This is congruent with absorption measurements from the literature, where the lowest lying absorption line of both constituents disappear for a perfect

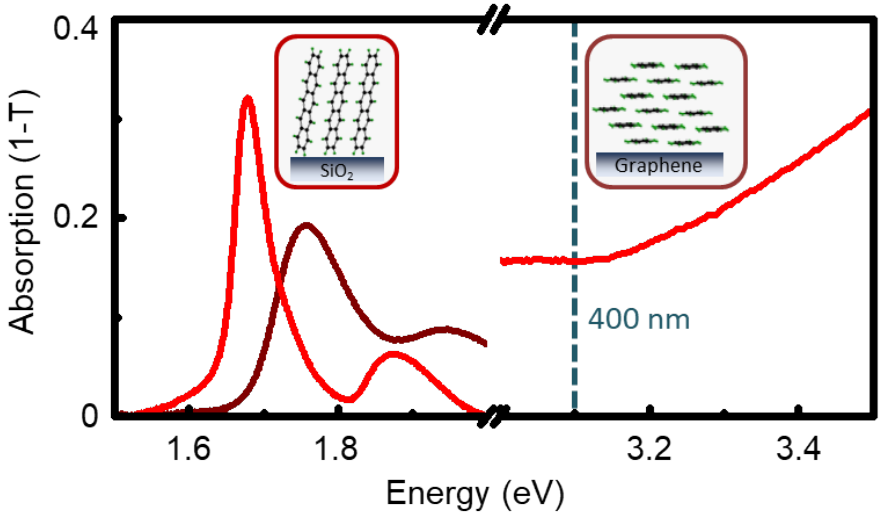

Figure 4.10: Absorption spectra of unitary lying and standing PFP samples. The low energy part shows the lowest lying exciton resonances. Their energetic shift is similar to the split as observed in the corresponding emission spectra shown in Fig. 4.9. The high energy part shows significant absorption of the lying sample for the excitation wavelength used in the all emission spectra presented in this work.

equimolar intermixture [112].

All three samples show two distinct interface related CT-signals. The most pronounced

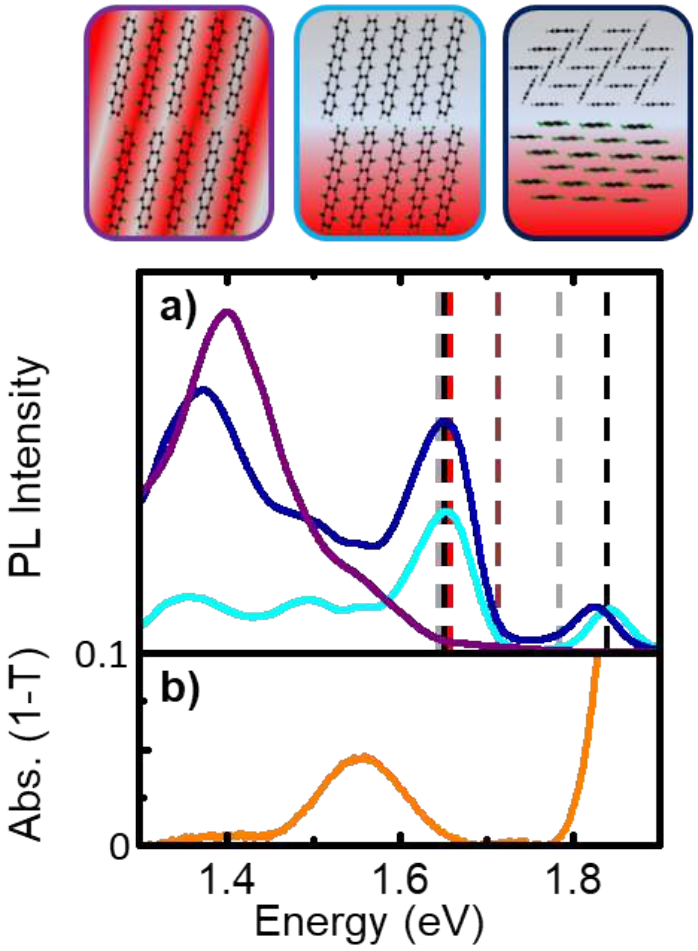

Figure 4.11: Emission spectra of the PEN/PFP heterostructures (a) and the absorption spectra of the intermixed sample (b) taken at room temperature from Ref. [112]. For reference, a schematic depiction of the three samples is added at the top. The energetic position of the emission lines observable in the unitary films is marked by the dashed lines, color coded to match the corresponding sample.

is found for the intermixed sample, as to be expected since an intermixture maximized the interface area between the two constituent molecules. Considering this, the relative intensity of the main CT-signal lying heterostack is unexpected. A comparison between the relative intensities of the standing and lying heterostacks emphasizes the importance of structural control at the interface: CT state formation is increased by a factor of five

for the lying heterostack with π-stacking across the heterointerface when compared to the standing heterostack with edge-on interface alignment. As those states are often discussed as precursors for carrier separation in OPV applications [35, 14, 36, 37, 38, 39, 48], the influence of molecular alignment are important for the creation of highly functional devices. All three samples show a satellite CT-signal at higher energy with rather unclear origin. While contributions from extrinsic so called deep self-trapped PEN exciton states can not be completely ruled out for the heterostacks [113], no such state is possible for the intermixture as no unitary PEN signals are observable in the first place. As shown in Fig. 4.11b, the CT-state is also visible in absorption around 1.6 eV. As there is some spectral overlap between the 1.645 eV emission and this absorption signal, energy transfer between the two systems via reabsorption or Förster resonance energy transfer (FRET) seems possible. This would further explain the pronounced CT-emission in the lying heterostack: higher intensity of the 1.645 eV emission in the lying heterostack when compared to its standing counterpart could increase the relative brightness of the CT-state. Furthermore, the existence of an absorption channel infers that a direct excitation of the CT-state is possible. Indeed, exciting the system directly at 1.6 eV yields strong CT-signal. No significant spectral differences between the spectra obtained for different excitation wavelengths are observed.

To obtain further insight into the emission of the heterosystems, their exciton dynamics are examined, as depicted in Fig. 4.12. A comparison between the free exciton dynamics in PEN and the dynamics of the corresponding emission in the heterostacks (Fig. 4.12a) reveals no significant changes caused by the introduction of the interface. The emission dynamics observable at 1.645 eV in the standing heterostack (Fig. 4.12b, light blue curve) are perfectly recreated by the emission dynamics of the self-trapped PEN emission alone (black curve). Again, no contribution from the PFP layer is observed in the standing stack, as it would result in a fast initial decay unobserved in the heterostack.

The assignment of the corresponding peak in the lying heterostack is more complicated, as both the PEN and PFP layer contribute to the emission. Thus, the sum of the transients of the self-trapped PEN and free PFP emissions before normalization is calculated to obtain the orange curve in Fig. 4.12b. The initial decay is governed by the fast PFP emission, while PEN becomes dominant after a few 100 ps. This superposition of PEN and PFP emissions perfectly reproduces the dynamics of the lying heterostack at this energy range (dark blue curve). The only observed difference is a slight change of the

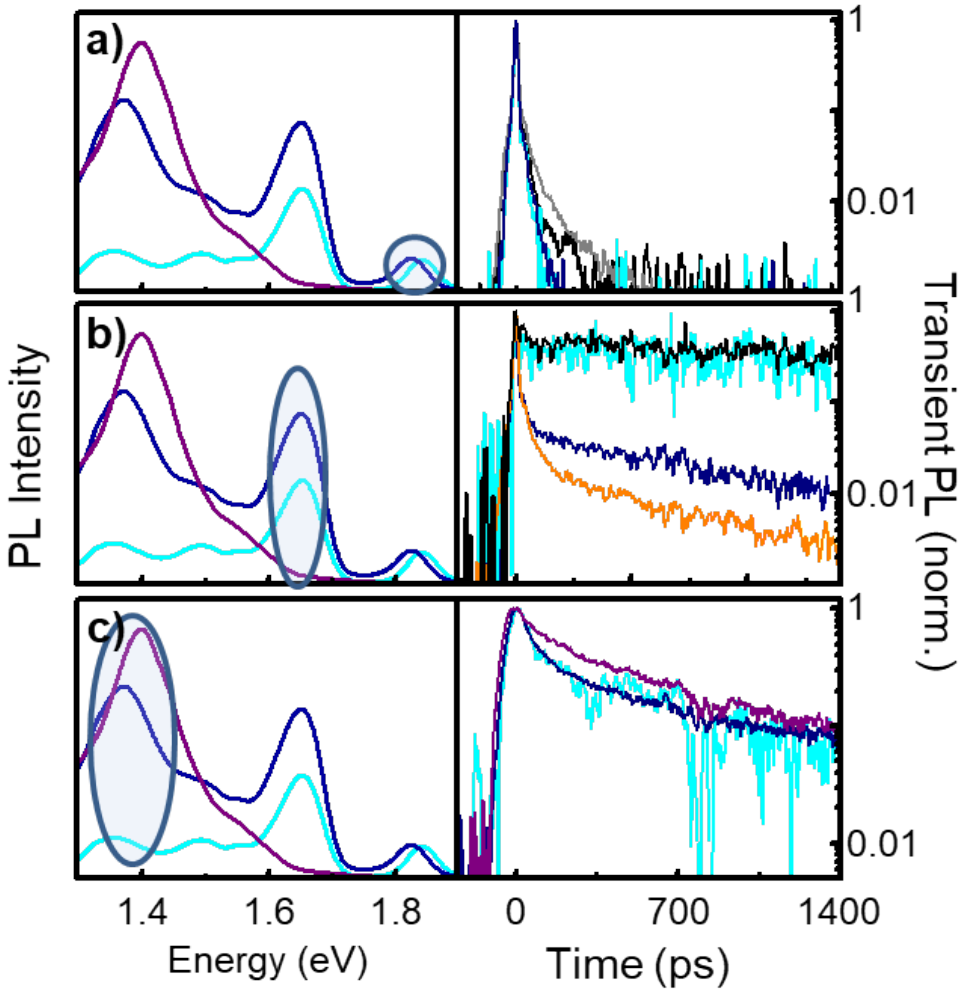

Figure 4.12: Emission dynamics of the PEN/PFP heterosystems in comparison to the corresponding dynamics of the unitary samples. Emission dynamics in the different energy ranges are shown, as indicated by the left half of each subfigure: the free PEN exciton around 1.8 eV (a), the self-trapped PEN and PFP channel at 1.645 eV (b) and the CT channel around 1.4 eV (c). Transient PL curves from the unitary films are shown for comparison when appropriate, following the color code established in Fig. 4.8. The orange curve in subfigure (b) corresponds to an incoherent sum of the PFP and self-trapped PEN emission in the lying unitary films for accurate comparison to the corresponding signal observed in the lying heterostack (dark blue curve).

relative weight of the PEN and PFP contribution, which can be attributed to a mix of self-attenuation of the pump and PEN due to absorption in the top PFP layer and slight

PL source	Short lifetime (ps)	Long lifetime (ps)
Standing PFP	30	–
Lying PFP	20	–
Standing PEN, free exciton	20	–
Lying PEN, free exciton	20	–
Standing PEN, self-trapped exciton	–	3000
Lying PEN, self-trapped exciton	–	800
Standing heterostack 1.8 eV	20	–
Standing heterostack 1.645 eV	–	300
Standing heterostack CT exciton	50	730
Lying heterostack 1.8 eV	20	–
Lying heterostack 1.645 eV	20	800
Lying heterostack CT exciton	50	840
Intermixture CT exciton	80	760

Table 4.1: Measured emission lifetimes of all PEN, PFP and PEN/PFP samples. For bi-exponential decay two lifetimes are given.

variations of thickness in the heterostack. Figure 4.12c displays the dynamics of the CT-state. Compared to the emission from pure PEN or PFP, the emission lifetimes observed in the CT-state are rather long. If those states are indeed CT-excitons with spatial separation of the hole and the electron, a diminished recombination efficiency would be expected. Additionally, the lifetimes rule out singlet fission in the CT-system, as this effect would lead to decay times far below 100 ps, as visible in the PL lifetimes of unitary films. While the dynamics of the two heterostacks are virtually identical, slight deviations from the dynamics of the intermixture are observed, especially in the first 100 ps after excitation. The initial fast decay of the heterostacks is attributed to trap states at the interface, as this decay channel seems to saturate quickly. The bigger impact of defects on the heterostacks infers a relatively defect free blend in the intermixed sample. All measured emission lifetimes are summarized in table 4.1.

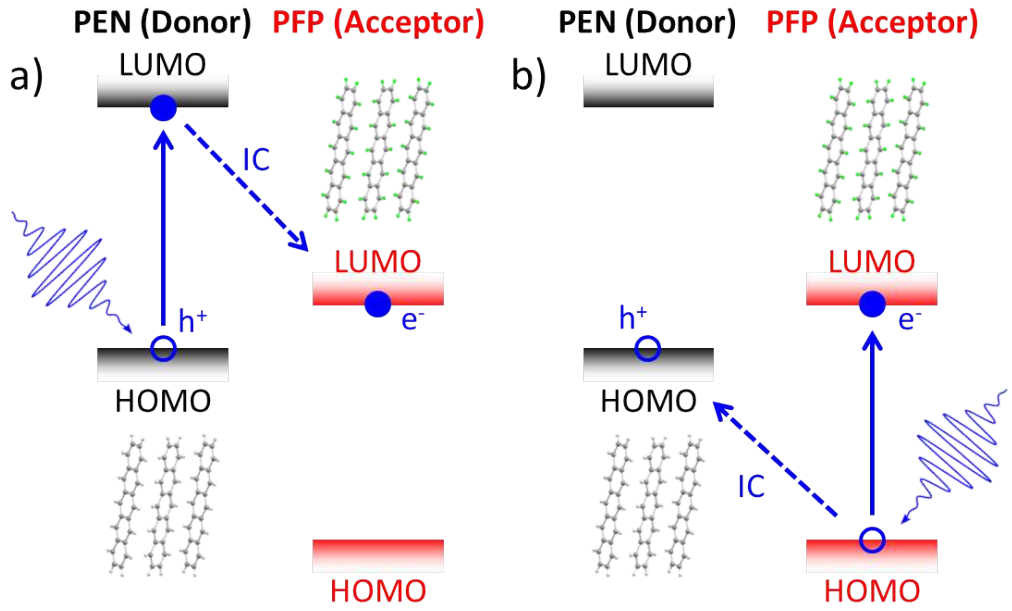

Figure 4.13: Possible indirect excitation pathways of a CT-exciton across a heterointerface, via initial donor (a) and via acceptor (b) excitation.

4.2.3 Excitation Channels of the Charge-Transfer State

As the optical properties of the CT-state are now known, this section will focus on the excitation pathways of the system. Following the classical theory of CT-excitons, these interface CT-states form with an electron located on the acceptor and a hole on the donor molecule 2.2.4 [14, 26]. Besides direct excitation,*i.e.*, excitation with a wavelength matching the absorption signal of the CT-state, primary excitation of the donor or acceptor molecules with subsequent CT across the interface should also be possible. However, the efficiency of each excitation channel is to be determined. The different pathways are schematically displayed in Fig. 4.13. Investigating the excitation pathways will also answer an open question in our above interpretation of the CT-emission from the heterostacks: is the observed increase in signal strength for the lying sample, at least in part, due to the increased absorption of the lying PFP layer or, an actual increase of CT-exciton formation efficiency?

To tackle all these questions, PLE and absorption spectroscopy are performed on the

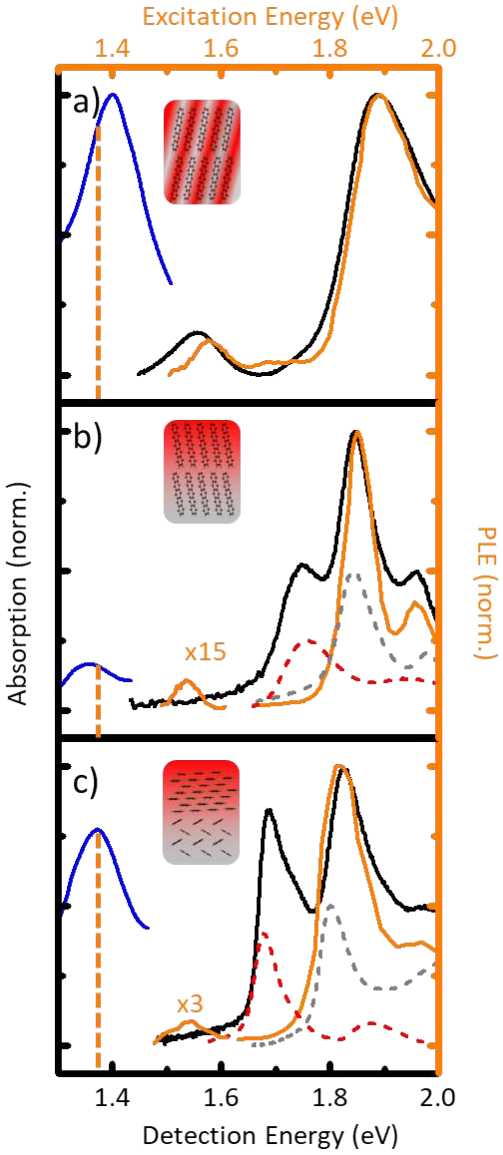

Figure 4.14: Absorption spectra (black curves) and PLE spectra (orange curve) of the intermixed heterostructure (a), the standing (b) and the lying heterostack (c). The central detection wavelength is marked by the dashed line at 900 nm. The emission spectra of the CT-state is given in blue for reference. The absorption spectra corresponding to the unitary constituent layers of PEN (grey) and PFP (red) in each of the heterostacks are given as dashed lines, scaled to half the intensity of the corresponding feature visible in the absorption of the heterostacks.

heterosystems. As described in 3.2.2, the total measured PLE intensity I_{PLE} can be written as

$$I_{PLE}(\omega)(\omega_d) = A(\omega) \cdot \gamma(\omega)\Phi(\omega_d). \tag{4.6}$$

Here ω_d is the detection wavelength, $A(\omega)$ the absorption at the excitation energy ω, $\gamma(\omega)$ the coupling efficiency of absorbed electrons at the excitation energy ω to the radiating state at ω_d, and Φ_d the radiative quantum yield of the emitting state. The quantum yield does not depend on the excitation energy. Hence, it only adds an offset to the whole excitation spectrum, as the detection energy is not changed throughout the experiment. The normalized PLE spectra contain only information on the relative intensities of $A(\omega)$ and $\gamma(\omega)$. If one compares those spectra to a absorption spectra of the same sample normalized to the same peak, one can deduces the influence of the absorption and gain information on the relative coupling strength $\gamma(\omega)$. This comparison is on display in Fig. 4.14. The intermixed sample (Fig. 4.14a) displays a peak by peak matching of the absorption and PLE spectra for all non CT-state related signals. The vanishing of the lowest lying excitons of unitary PEN and PFP previously observed in the literature is reproduced [112]. At lower energies one can observe an absorption lines not related to any of the constituent molecules at 1.55 eV. This is assigned to the CT-exciton system, as it is also observed in the PLE spectra. The broader low energy flank of the absorption could be attributed to defect states with non vanishing absorption, which do recombine non-radiatively and therefore are not observed in the PLE spectra. All observed absorption channels contribute to the CT-emission. Generally, a decrease in PLE intensity when compared to the absorption intensity for increasing excitation energy can be observed. As more energy needs to be dissipated for the excited states to be converted into the CT-state, an increasing amount of lattice interaction is required for relaxation. This increases the chance for non-radiative recombination at defect states and therefore decreses γ. Hence, the relative intensity of the PLE spectrum will be lower than the corresponding absorption, even when all absorptive states couple to the CT-state.

A more complicated picture is observed for the heterostacks. The absorption spectrum of both stacks (Fig. 4.14b,c) clearly displays the lowest exciton levels of both PEN and PFP at 1.84 eV and 1.75 eV, respectively. As previously discussed, the PLE spectra

lose intensity relative to the absorption spectra for higher excitation energies. While all other features are reproduced by the PLE measurements, no PFP related signals are observed. While PFP exhibits significant absorption in both heterostacks, no energy transfer from any PFP to the CT-state is observed independent of molecular orientation at the interface. One can deduce from Eq. 4.6 that $\gamma(\omega_{PFP})$, the coupling strength of excitons or carriers injected at the resonance frequencies corresponding to the PFP layer to the CT-state, is zero. Direct excitation of the CT-state is possible in both heterostacks, as proven by the PLE signal around 1.55 eV. This provides us with astonishingly clear answers to our questions regarding excitation pathways: while direct and indirect excitation via the donor molecule is possible, all excitations of the PFP acceptor layer does not contribute to the formation of the CT-state. This has immediate implication on any possible applications of PEN/PFP heterostructures in OPVs, as the acceptor layer cannot contribute to the photon collection, reducing the efficiency of the device. Additionally, the inactivity of PFP in CT formation allows us to unambiguously claim higher formation efficiency of CT-states in the lying heterostack, as the increase in CT-emission compared to the the standing heterostack cannot be tracked back to better absorption efficiency in the PFP layer.

Besides those immediate consequences, the collective data gathered on the PEN/PEN heterosystems in this work enables us to evaluate the validity of classical CT-exciton theory as known form the literature 2.2.4 [14, 26] when applied to PEN/PFP heterostructures. Equation 2.39 shows us how the energy level of such a classical CT-exciton is calculated. A major part of this equation are the frontier orbital energies of the donor and acceptor molecule directly at the interface, with some corrections necessary due to polarization of the lattice and Coulomb interactions of the separated hole and electron. Those correcting terms need to lower the total energy to create a stable quasi particle. Without this, separated holes and electrons would be energetically favorable and no CT-exciton would be observed. The frontier orbitals of both molecules of a thin standing PEN/PFP heterostack have been measured by ultraviolet photoemission spectroscopy (UPS) [114]. The results are displayed in Fig. 4.15a. As the energy difference between the PEN HOMO and PFP LUMO is only 0.4 eV, classical CT-exciton theory cannot account for the observed CT-exciton absorption at 1.55 eV. Even without these energetic discrepancy, in a classical picture excitation via hole transfer from the acceptor should be possible, yet no such CT is observed in the PLE spectra.

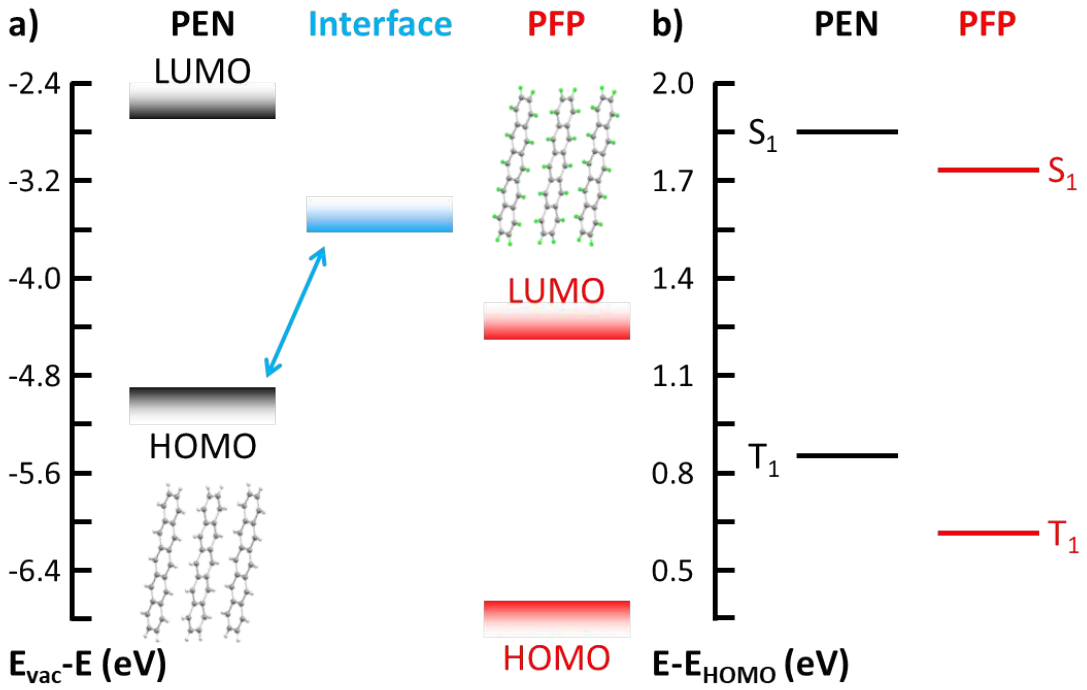

Figure 4.15: Level alignment of the PEN/PFP frontier orbitals at the heterointerface according to Ref. [114] a) and excitonic system of both constituent layers according b). The blue energy level in a) show the most likely energetic position of our observed interfacial CT-state. The energy levels of the lowest lying triplet exctions T_1 are taken from Ref. [115, 116], the lowest lying singlet states from the measurements presented in Fig. 4.14.

As the CT-state is indirectly excitable via the donor levels, one can conclude that a new energy level has to form at the interface about 1.55 eV above the PEN HOMO, as displayed by the blue state in Fig. 4.15. The invalidity of classical CT-exciton theory for the PEN/PFP heterosystem is consistent with the disappearance of the lowest PEN and PFP absorption levels the intermixed sample [112]. It is apparent that completely new frontier orbitals form at the heterointerface, which results in an absorbing interfacial state at 1.55 eV. The exact nature of this state remains unclear: even if it is not described by classical CT-exciton theory, it could still be a polar exciton state across the interface. The unperturbed frontier orbitals of the constituting molecules on which classical CT-exciton theory is built lose their relevance. While this is certainly not valid for all materials systems, classical CT-exciton theory is shown not to be universal either. Instead,

a thorough evaluation of each individual heterosystem on a case-by-case basis seems necessary. More sophisticated *ab initio* theory is needed to gain a more in depth and general understanding of excitonic states at the interface of an organic heterosystems, as highlighted by the results presented in this thesis.

5 Summary and Outlook

In the field of inorganic semiconductors, the importance of molecular alignment within aromatic organic solids is without equal. However, it is certainly among the issues in need of continued investigation to bring the understanding of organic semiconductors to the same level of that achieved in silicon based systems. The results presented in this thesis are a contribution towards this goal. Two different types of material systems are investigated. The influence of polymorphism on the optical properties of bulk crystals are studied in the model system of perylene. Furthermore, the properties of interface specific exciton states in dependence of varying mutual molecular alignment of donor and acceptor molecules in PEN/PFP heterosystems are investigated.

The former, due to the astonishing almost defect free sample quality of the available perylene crystals, presents an excellent opportunity to test state of the art first-principle calculations by a direct experiment-theory comparison. Indeed, excellent agreement of theory and experiment is achieved. Differences in the optical properties of α and β-perylene could directly be observed and correlated to the unique structural makeup of both polymorphs. The α-phase is dominated by strong interaction among molecules forming the perylene dimers which serve as the basic building blocks for the herring-bone structure of α-phase crystals. In contrast, interactions among different dimers are very limited. Hence, strongly localized excitons lead to long carrier lifetimes and flat electronic bands. As an uninterrupted chain of π-stacked molecules along the b-axis of the β-phase leads to a significant increase of molecular interactions in this direction, significant differences between both perylene polymorphs are found. Where the electronic bandstructure is almost dispersionless for both crystal types, the b-axis of the β-phase is a notable exception, displaying increased dispersion in congruence to an increase in molecular interaction strength along this crystalline axis. Consequently, the bright exciton states of the β-phase are delocalized along the b-axis, leading to

significantly shorter exciton lifetimes. Our study of perylene crystals is a splendid example of interplay of optical measurements, structural sample control and high-end calculations to achieve the most comprehensive picture possible of the physics of the excitonic system of perylene crystals.

Such a complete picture could not be achieved for the PEN/PFP heterosystems, as one important building block, first-principle calculations, does not yet exist for molecular donor-acceptor interfaces. In the absence of such calculations, simplified models within the classical CT-exciton theory are used to describe the properties of the interface features observable in organic materials. The breakdown of such estimations further highlights the gaps in our current physical understanding. Indeed, both the measured energetic position and the available excitation channels for the CT-states in PEN-PFP heterosystems are found to be in strong conflict with the picture of a simple CT-exciton. The general belief that organic semiconductors are little more than isolated oriented molecules with only small correction to their energetics and an addition of an excitonic system is demonstrated to be a crude oversimplification. As shown in the case of perylene, intermolecular interaction can be increased by suitable stacking of aromatic molecules to results in significant dispersion of the electronic bands. It seems likely that the intermolecular interaction between PEN and PFP molecules at the heterointerface leads to a perturbation of the original frontier orbitals and therefore a completely new electronic system. Such effects would render all theories relying on the original frontier orbitals at the interface meaningless. Our study provided a thorough experimental evaluation of optical properties of a CT-state for different molecular alignments at the interface, clearly showing the role π-stacking of aromatic molecules plays in increasing the formation of interface state. As both constituting molecules are rather simple in comparison to complicated polymer chains often employed in OPV devices, these results are the ideal starting point to match the experimental results with *ab initio* calculations of CT-exciton states across a heterointerface. This is badly needed to gain predictive understanding of organic semiconductors pn-junctions of any conceivable application.

List of Figures

List of Tables

Bibliography

[1] J.S. Kilby. Miniaturized electronic circuits, 1964.

[2] GfK. Umsatz mit Smartphones weltweit in den Jahren 2013 bis 2016 (in Milliarden US-Dollar). Technical report, GfK, 2017.

[3] World Bank. GDP of Belgium 2015, 2017.

[4] McKinsey and Company. *Lighting the Way: Perspectives on the Global Lighting Market*. McKinsey, 2011.

[5] EPIA. Global Market Outlook for Solar Power / 2016 - 2020. Technical report, EPIA, 2016.

[6] Y. Kolic, R. Gauthier, M.A.Garcia Perez, A. Sibai, J.C. Dupuy, P. Pinard, R. M'Ghaieth, and H. Maaref. Electron powder ribbon polycrystalline silicon plates used for porous layer fabrication. *Thin Solid Films*, 255(1-2):159–162, 1995.

[7] Aj J Read, Rj J Needs, Kj J Nash, L T Canham, P D J Calcott, and A Qteish. First-principles calculations of the electronic properties of silicon quantum wires. *Physical Review Letters*, 69(8):1232–1235, 1992.

[8] Samsung. Galaxy S8 S8+ Specifications, 2017.

[9] LG. IPS 21:9 Curved UltraWide™ Monitor Datasheet, 2016.

[10] Marco Olguin, Rajendra R. Zope, and Tunna Baruah. Effect of geometrical orientation on the charge-transfer energetics of supramolecular (tetraphenyl)-porphyrin/C60 dyads. *Journal of Chemical Physics*, 138(7):074306, 2013.

[11] Alexey V Akimov and Oleg V Prezhdo. Nonadiabatic Dynamics of Charge Transfer and Singlet Fission at the Pentacene / C 60 Interface. *Journal of the American Chemical Society*, 136:1599–1608, 2014.

[12] Youichi Sakamoto, Toshiyasu Suzuki, Masafumi Kobayashi, Yuan Gao, Yasushi Fukai, Youji Inoue, Fumio Sato, and Shizuo Tokito. Perfluoropentacene: High-Performance p-n Junctions and Complementary Circuits with Pentacene. *Journal of the American Chemical Society*, 126:8138–8140, 2004.

[13] M. Knupfer. Exciton binding energies in organic semiconductors. *Applied Physics A*, 77(5):623–626, 2003.

[14] Koen Vandewal. Interfacial Charge Transfer States in Condensed Phase Systems. *Annu. Rev. Phys. Chem*, 67:113–133, 2016.

[15] Askat E Jailaubekov, Adam P Willard, John R Tritsch, Wai-lun Chan, Na Sai, Raluca Gearba, Loren G Kaake, Kenrick J Williams, Kevin Leung, Peter J Rossky, and X-y Zhu. Hot charge-transfer excitons set the time limit for charge separation at donor/acceptor interfaces in organic photovoltaics. *Nature Materials*, 12(1):66–73, 2012.

[16] Sang-Il Choi, Joshua Jortner, Stuart A. Rice, and Robert Silbey. Charge-Transfer Exciton States in Aromatic Molecular Crystals. *The Journal of Chemical Physics*, 41(11):3294–3306, 1964.

[17] Ming L. Tang, Anna D. Reichardt, Nobuyuki Miyaki, Randall M. Stoltenberg, and Zhenan Bao. Ambipolar, High Performance, Acene-Based Organic Thin Film Transistors. *Journal of the American Chemical Society*, 130(19):6064–6065, 2008.

[18] A L Atwood, J E D Davies, D D Macnicol, F Vogtle, T Bein, K Brown, G C Frye, C J Brinker, Y Yan, G A Ozin5, M E Garcia, J L Naffin, N Deng, T E A L Mallouk, J E D Atwood, D D Davies, F Macnic-Ol, and Vogtle. Record Charge Carrier Mobility in a Room- Temperature Discotic Liquid-Crystalline Derivative of Hexabenzocoronene. *Advanced Materials*, 634(9):7640–905, 1996.

[19] Mahdieh Aghamohammadi, Anton Fernández, Malte Schmidt, Ana Pérez-Rodríguez, Alejandro Rodolfo Goñi, Jordi Fraxedas, Guillaume Sauthier, Markos Paradinas, Carmen Ocal, and Esther Barrena. Influence of the relative molecular orientation on interfacial charge-transfer Excitons at donor/acceptor Nanoscale heterojunctions. *Journal of Physical Chemistry C*, 118(27):14833–14839, 2014.

[20] André Pick, Michael Klues, Andre Rinn, Klaus Harms, Sangam Chatterjee, and Gregor Witte. Polymorph-Selective Preparation and Structural Characterization of Perylene Single Crystals. *Crystal Growth & Design*, 15(11):5495–5504, 2015.

[21] Ingo Salzmann, Steffen Duhm, Georg Heimel, Martin Oehzelt, Rolf Kniprath, Robert L Johnson, Jürgen P. Rabe, and Norbert Koch. Tuning the Ionization Energy of Organic Semiconductor Films: The Role of Intramolecular Polar Bonds. *Journal of the American Chemical Society*, 130(39):12870–12871, 2008.

[22] Sean M. Ryno, Stephen R. Lee, John S. Sears, Chad Risko, and Jean-Luc Brédas. Electronic Polarization Effects upon Charge Injection in Oligoacene Molecular Crystals: Description via a Polarizable Force Field. *The Journal of Physical Chemistry C*, 117(27):13853–13860, 2013.

[23] K Broch, U Heinemeyer, A Hinderhofer, F Anger, R Scholz, A Gerlach, and F Schreiber. Optical evidence for intermolecular coupling in mixed films of pentacene and perfluoropentacene. *Physical Review B - Condensed Matter and Materials Physics*, 83(24):245307, 2011.

[24] Tobias Breuer and Gregor Witte. Controlling nanostructures by Templated templates: Inheriting molecular orientation in binary heterostructures. *ACS Applied Materials and Interfaces*, 7(36):20485–20492, 2015.

[25] Wolfgang Brütting and Chihaya Adachi. *Physics of Organic Semiconductors*. John Wiley & Sons, New York, 2 edition, 2012.

[26] Markus Schwoerer and Hans Christoph Wolf. *Organic Molecular Solids*. Wiley-VCH, Weinheim, 1 edition, 2005.

[27] Claus Klingshirn. *Semiconductor Optics*. Springer, 3 edition, 2007.

[28] Hermann Haken and Hans Christoph Wolf. *Molekülphysik und Quantenchemie*. Springer, New York, 5 edition, 2006.

[29] Hartmut Haug and Stephan W. Koch. *Quantum Theory of the Optical and Electronic Properties of Semiconductors*. World Scientific Publishing, Singapore, 1 edition, 2004.

[30] Slawomir Braun, William R. Salaneck, and Mats Fahlman. Energy-Level Alignment at Organic/Metal and Organic/Organic Interfaces. *Advanced Materials*, 21(14-15):1450–1472, 2009.

[31] Slawomir Braun, William R Salaneck, and Mats Fahlman. Energy-Level Alignment at Organic/Metal and Organic/Organic Interfaces. *Advanced Materials*, 21(14-15):1450–1472, 2009.

[32] Wikipedia. Aromaticity.

[33] J. Frenkel. On the Transformation of light into Heat in Solids. I. *Physical Review*, 37(1):17–44, 1931.

[34] J. Frenkel. On the Transformation of Light into Heat in Solids. II. *Physical Review*, 37(10):1276–1294, 1931.

[35] Koen Vandewal, Steve Albrecht, Eric T. Hoke, Kenneth R. Graham, Johannes Widmer, Jessica D. Douglas, Marcel Schubert, William R. Mateker, Jason T. Bloking, George F. Burkhard, Alan Sellinger, Jean M. J. Fréchet, Aram Amassian, Moritz K. Riede, Michael D. McGehee, Dieter Neher, and Alberto Salleo. Efficient charge generation by relaxed charge-transfer states at organic interfaces. *Nature Materials*, 13(1):63–68, 2013.

[36] Michael Graetzel, René A. J. Janssen, David B. Mitzi, and Edward H. Sargent. Materials interface engineering for solution-processed photovoltaics. *Nature*, 488(7411):304–312, 2012.

[37] Kenneth R Graham, Guy O Ngongang Ndjawa, Sarah M Conron, Rahim Munir, Koen Vandewal, John J Chen, Sean Sweetnam, Mark E Thompson, Alberto Salleo, Michael D. McGehee, and Aram Amassian. The Roles of Structural Order and Intermolecular Interactions in Determining Ionization Energies and

Charge-Transfer State Energies in Organic Semiconductors. *Advanced Energy Materials*, 6(22):1601211, 2016.

[38] Jean-Luc Brédas, Joseph E Norton, Jérôme Cornil, and Veaceslav Coropceanu. Molecular Understanding of Organic Solar Cells: The Challenges. *Accounts of Chemical Research*, 42(11):1691–1699, 2009.

[39] Myeong H. Lee, Eitan Geva, and Barry D. Dunietz. The Effect of Interfacial Geometry on Charge-Transfer States in the Phthalocyanine/Fullerene Organic Photovoltaic System. *Journal of Physical Chemistry A*, 120(19):2970–2975, 2016.

[40] M R Philpott. Optical Reflection Spectroscopy of Organic Solids. *Annual Review of Physical Chemistry*, 31(1):97–129, 1980.

[41] Millicent B Smith and Josef Michl. Recent Advances in Singlet Fission. *Annual Review of Physical Chemistry*, 64(1):361–386, 2013.

[42] Chandrasekhara V. Raman and Kariamanickam S. Krishnan. A New Type of Secondary Radiation. *Nature*, 121(3048):501–502, 1928.

[43] Charles Kittel. *Einführung in die Festkörperphysik*. Oldenbourg Wissenschaftsverlag, München, 14 edition, 2006.

[44] A. S. Davydov. The Theory of Molecular Excitons. *Soviet Physics Uspekhi*, 7(2):145–178, 1964.

[45] M Kasha, H. R. Rawls, and M. Ashraf El-Bayoumi. The exciton model in molecular spectroscopy. *Pure and Applied Chemistry*, 11(3-4):371–392, 1965.

[46] D. Beljonne, H. Yamagata, J. L. Brédas, F C Spano, and Y Olivier. Charge-Transfer Excitations Steer the Davydov Splitting and Mediate Singlet Exciton Fission in Pentacene. *Physical Review Letters*, 110(22):226402, 2013.

[47] Xiaoyang Zhu and Antoine Kahn. Electronic Structure and Dynamics at Organic Donor/Acceptor Interfaces. *MRS Bulletin*, 35(06):443–448, 2010.

[48] Feng Gao and Olle Inganäs. Charge generation in polymer–fullerene bulk-heterojunction solar cells. *Phys. Chem. Chem. Phys.*, 16(38):20291–20304, 2014.

[49] F. Grein and S. D. Peyerimhoff. Theoretical studies on excited states of Ne 2 . II. Potential curves for states dissociating to Ne+Ne*(3 s) with semiempirical spin–orbit interaction, and comparison with spectroscopic results. *The Journal of Chemical Physics*, 87(8):4684–4692, 1987.

[50] R. T. Williams and K. S. Song. The self-trapped exciton. *Journal of Physics and Chemistry of Solids*, 51(7):679–716, 1990.

[51] B. STEVENS and E. HUTTON. Radiative Life-time of the Pyrene Dimer and the Possible Role of Excited Dimers in Energy Transfer Processes. *Nature*, 186(4730):1045–1046, 1960.

[52] H. Auweter, D. Ramer, B. Kunze, and H.C. Wolf. The dynamics of excimer formation in perylene crystals. *Chemical Physics Letters*, 85(3):325–329, 1982.

[53] J. B. Birks and A. A. Kazzaz. Excimer Fluorescence. XII. The Pyrene Crystal Excimer Interaction Potential. *Proceedings of the Royal Society A: Mathematical, Physical and Engineering Sciences*, 304(1478):291–301, 1968.

[54] N.G. Basov, V.A. Danilychev, Yu.M Popov, and D.D. Khodkevich. Laser Operating in the Vacuum Region of the Spectrum by Excitation of Liquid Xenon with an Electron Beam. *JETP Lett.*, 12:329–331, 1970.

[55] Millicent B Smith and Josef Michl. Singlet Fission. *Chemical Reviews*, 110(11):6891–6936, 2010.

[56] G. G. Stokes. On the Change of Refrangibility of Light. *Philosophical Transactions of the Royal Society of London*, 142:463–562, 1852.

[57] Charles Darwin. *Journal of researches into the natural history and geology of the countries visited during the voyage of H.M.S. Beagle round the world, under the command of Capt. Fitz Roy, R.N.* J. Murray, London, 1860.

[58] S. Singh, W. J. Jones, W. Siebrand, B. P. Stoicheff, and W. G. Schneider. Laser Generation of Excitons and Fluorescence in Anthracene Crystals. *The Journal of Chemical Physics*, 42(1):330–342, 1965.

[59] William Shockley and Hans J. Queisser. Detailed Balance Limit of Efficiency of p-n Junction Solar Cells. *Journal of Applied Physics*, 32(3):510–519, 1961.

[60] Kolja Kolata, Tobias Breuer, Gregor Witte, and Sangam Chatterjee. Molecular packing determines singlet exciton fission in organic semiconductors. *ACS Nano*, 8(7):7377–7383, 2014.

[61] Yan-Ju Luo, Zhi-Yun Lu, and Yan Huang. Triplet fusion delayed fluorescence materials for OLEDs. *Chinese Chemical Letters*, 27(8):1223–1230, 2016.

[62] Chien Jung Chiang, Alpay Kimyonok, Marc K Etherington, Gareth C. Griffiths, Vygintas Jankus, Figen Turksoy, and Andy P Monkman. Ultrahigh efficiency fluorescent single and bi-layer organic light emitting diodes: The key role of triplet fusion. *Advanced Functional Materials*, 23(6):739–746, 2013.

[63] Christian Schneider, Arash Rahimi-Iman, Na Young Kim, Julian Fischer, Ivan G. Savenko, Matthias Amthor, Matthias Lermer, Adriana Wolf, Lukas Worschech, Vladimir D. Kulakovskii, Ivan A. Shelykh, Martin Kamp, Stephan Reitzenstein, Alfred Forchel, Yoshihisa Yamamoto, and Sven Höfling. An electrically pumped polariton laser. *Nature*, 497(7449):348–352, 2013.

[64] Alexey Kavokin. Polaritons: The rise of the bosonic laser. *Nature Photonics*, 7(8):591–592, 2013.

[65] B. Hönerlage, R. Lévy, J.B. Grun, C. Klingshirn, and K. Bohnert. The dispersion of excitons, polaritons and biexcitons in direct-gap semiconductors. *Physics Reports*, 124(3):161–253, 1985.

[66] Michael R. Philpott. Theory of Molecular Polaritons. Application to the Reflection Spectra of Anthracene, 1,5-Bis(dimethylamino)pentamethinium Perchlorate, and Some Other Cationic Dye Crystals. *The Journal of Chemical Physics*, 54(5):2120–2129, 1971.

[67] Marianus Czerny. Über eine neue Form der Rubenssehen Reststrahlenmethode. *Zeitschrift für Physik*, 16(1):321–331, 1923.

[68] Spectra Physics. Tsunami-Mode Locked Ti:sapphire Laser Manual, 2002.

[69] John Kerr. A new relation between electricity and light: Dielectrified media birefringent. *Philosophical Magazine Series 4*, 50(333):337–348, 1875.

[70] Alexey Chernikov. *Time-Resolved Photoluminescence Spectroscopy of Semiconductors for Optical Applications Beyond the Visible Spectral Range*. Phd thesis, Philipss Universität Marburg, 2011.

[71] NKT Photonics. FemtoWHITE 800 Supercontinuum Device Datasheet.

[72] Xin Zhang, Zhenhuan Lu, Long Ye, Chuanlang Zhan, Jianhui Hou, Shaoqing Zhang, Bo Jiang, Yan Zhao, Jianhua Huang, Shanlin Zhang, Yang Liu, Qiang Shi, Yunqi Liu, and Jiannian Yao. A potential perylene diimide dimer-based acceptor material for highly efficient solution-processed non-fullerene organic solar cells with 4.03% efficiency. *Advanced Materials*, 25(40):5791–5797, 2013.

[73] Yuze Lin, Yifan Wang, Jiayu Wang, Jianhui Hou, Yongfang Li, Daoben Zhu, and Xiaowei Zhan. A star-shaped perylene diimide electron acceptor for high-performance organic solar cells. *Advanced Materials*, 26(30):5137–5142, 2014.

[74] M.I. Alonso, M. Garriga, N. Karl, J.O. Ossó, and F. Schreiber. Anisotropic optical properties of single crystalline PTCDA studied by spectroscopic ellipsometry. *Organic Electronics*, 3(1):23–31, 2002.

[75] V. Bulović, P.E. Burrows, S.R. Forrest, J.A. Cronin, and M.E. Thompson. Study of localized and extended excitons in 3,4,9,10-perylenetetracarboxylic dianhydride (PTCDA) I. Spectroscopic properties of thin films and solutions. *Chemical Physics*, 210(1-2):1–12, 1996.

[76] M.H. Hennessy, Z.G. Soos, R.A. Pascal, and A. Girlando. Vibronic structure of PTCDA stacks: the exciton–phonon-charge-transfer dimer. *Chemical Physics*, 245(1-3):199–212, 1999.

[77] M. Wewer and F. Stienkemeier. Molecular versus excitonic transitions in PTCDA dimers and oligomers studied by helium nanodroplet isolation spectroscopy. *Physical Review B*, 67(12):125201, 2003.

[78] Linus Gisslén and Reinhard Scholz. Crystallochromy of perylene pigments: Interference between Frenkel excitons and charge-transfer states. *Physical Review B*, 80(11):115309, 2009.

[79] C. Joblin, F. Salama, and L. Allamandola. Absorption and emission spectroscopy of perylene (C20H12) isolated in Ne, Ar, and N2 matrices. *The Journal of Chemical Physics*, 110(15):7287–7297, 1999.

[80] S. J. Cyvin, B N Cyvin, and P Klaeboe. Condensed Aromatics. Part XIX Perylene. *Spectroscopy Letters*, 16(4):239–248, 1983.

[81] Xiaofeng Tan and Farid Salama. Cavity ring-down spectroscopy and theoretical calculations of the S1(B3u1)←S0(Ag1) transition of jet-cooled perylene. *The Journal of Chemical Physics*, 122(8):084318, 2005.

[82] Masahiro Kotani, Koji Kakinuma, Masafumi Yoshimura, Kouta Ishii, Saori Yamazaki, Toshifumi Kobori, Hiroyuki Okuyama, Hiroyuki Kobayashi, and Hirokazu Tada. Charge carrier transport in high purity perylene single crystal studied by time-of-flight measurements and through field effect transistor characteristics. *Chemical Physics*, 325(1):160–169, 2006.

[83] Robin M. Hochstrasser. Spectral Effects of Strong Exciton Coupling in the Lowest Electronic Transition of Perylene. *The Journal of Chemical Physics*, 40(9):2559, 1964.

[84] Mark Botoshansky, Frank H. Herbstein, and Moshe Kapon. Towards a Complete Description of a Polymorphic Crystal: The Example of Perylene. *Helvetica Chimica Acta*, 86(4):1113–1128, 2003.

[85] Kiyokazu Fuke, Koji Kaya, Takashi Kajiwara, and Saburo Nagakura. The polarized reflection and absorption spectra of perylene crystals in monomeric and dimeric forms. *Journal of Molecular Spectroscopy*, 63(1):98–107, 1976.

[86] Roman Forker, Marco Gruenewald, and Torsten Fritz. Optical differential reflectance spectroscopy on thin molecular films. *Annual Reports Section "C" (Physical Chemistry)*, 108:34, 2012.

[87] W. Kohn and L. J. Sham. Self-Consistent Equations Including Exchange and Correlation Effects. *Physical Review*, 140(4A):A1133–A1138, 1965.

[88] Mark S. Hybertsen and Steven G. Louie. First-Principles Theory of Quasiparticles: Calculation of Band Gaps in Semiconductors and Insulators. *Physical Review Letters*, 55(13):1418–1421, 1985.

[89] Mark S. Hybertsen and Steven G. Louie. Electron correlation in semiconductors and insulators: Band gaps and quasiparticle energies. *Physical Review B*, 34(8):5390–5413, 1986.

[90] Lars Hedin. New Method for Calculating the One-Particle Green's Function with Application to the Electron-Gas Problem. *Physical Review*, 139(3A):A796–A823, 1965.

[91] Michael Rohlfing and Steven G. Louie. Electron-hole excitations and optical spectra from first principles. *Physical Review B*, 62(8):4927–4944, 2000.

[92] Giovanni Onida, Lucia Reining, and Angel Rubio. Electronic excitations: Density-functional versus many-body Green's-function approaches. *Reviews of Modern Physics*, 74(2):601–659, 2002.

[93] Thomas J. Kosic, Claire L. Schosser, and Dana D. Dlott. Vibrational spectroscopy of solid state molecular dimers. *Chemical Physics Letters*, 96(1):57–64, 1983.

[94] C. R. Fincher, M. Ozaki, M. Tanaka, D. Peebles, L. Lauchlan, A. J. Heeger, and A. G. MacDiarmid. Electronic structure of polyacetylene: Optical and infrared studies of undoped semiconducting (CH)x and heavily doped metallic (CH)x. *Physical Review B*, 20(4):1589–1602, 1979.

[95] Atsushi Watanabe, Masashi Tanaka, and Jiro Tanaka. Electrical and Optical Properties of a Stable Synthetic Metallic Polymer: Polypyrrole. *Bulletin of the Chemical Society of Japan*, 54(8):2278–2281, 1981.

[96] R.R. Pennelly and C.J. Eckhardt. Quasi-metallic reflection spectra of TCNQ single crystals. *Chemical Physics*, 12(1):89–105, 1976.

[97] F. Wudl. From organic metals to superconductors: managing conduction electrons in organic solids. *Accounts of Chemical Research*, 17(6):227–232, 1984.

[98] M Carmen Ruiz Delgado, Kathryn R Pigg, Demetrio A. da Silva Filho, Nadine E Gruhn, Youichi Sakamoto, Toshiyasu Suzuki, Reyes Malave Osuna, Juan Casado, Victor Hernandez, Juan Teodomiro Lopez Navarrete, Nicolas G. Martinelli, Jérôme Cornil, Roel S. Sanchez-Carrera, Veaceslav Coropceanu, and Jean-Luc Bredas. Impact of Perfluorination on the Charge-Transport Parameters of Oligoacene Crystals. *Journal of the American Chemical Society*, 131(4):1502–1512, 2009.

[99] Pierluigi Cudazzo, Francesco Sottile, Angel Rubio, and Matteo Gatti. Exciton dispersion in molecular solids. *Journal of Physics: Condensed Matter*, 27(11):113204, 2015.

[100] B. Walker, H. Port, and H.C. Wolf. The two-step excimer formation in perylene crystals. *Chemical Physics*, 92(2-3):177–185, 1985.

[101] I. P M Bouchoms, W. A. Schoonveld, J. Vrijmoeth, and T. M. Klapwijk. Morphology identification of the thin film phases of vacuum evaporated pentacene on SIO2 substrates. *Synthetic Metals*, 104(3):175–178, 1999.

[102] Theo Siegrist, Christian Kloc, Jan H. Schön, Bertram Batlogg, Robert C. Haddon, Steffen Berg, and Gordon A. Thomas. Enhanced Physical Properties in a Pentacene Polymorph. *Angewandte Chemie International Edition*, 40(9):1732–1736, 2001.

[103] Jan Götzen, Daniel Käfer, Christof Wöll, and Gregor Witte. Growth and structure of pentacene films on graphite: Weak adhesion as a key for epitaxial film growth. *Physical Review B*, 81(8):085440, 2010.

[104] Stefan Kowarik, Alexander Gerlach, Alexander Hinderhofer, Silvia Milita, Francesco Borgatti, Federico Zontone, Toshiyasu Suzuki, Fabio Biscarini, and Frank Schreiber. Structure, morphology, and growth dynamics of perfluoropentacene thin films. *physica status solidi (RRL) – Rapid Research Letters*, 2(3):120–122, 2008.

[105] Ingo Salzmann, Armin Moser, Martin Oehzelt, Tobias Breuer, Xinliang Feng, Zhen-yu Juang, Dmitrii Nabok, Raffaele G. Della Valle, Steffen Duhm, Georg Heimel, Aldo Brillante, Elisabetta Venuti, Ivano Bilotti, Christos Christodoulou,

Johannes Frisch, Peter Puschnig, Claudia Draxl, Gregor Witte, Klaus Müllen, and Norbert Koch. Epitaxial Growth of π-Stacked Perfluoropentacene on Graphene-Coated Quartz. *ACS Nano*, 6(12):10874–10883, 2012.

[106] T. Aoki-Matsumoto, K. Furata, T. Yamada, H. Moriya, K. Mizuno, and A. H. Matsui. Excitonic Photoluminescence in Pentacene Single Crystal. *International Journal of Modern Physics B*, 15(28n30):3753–3756, 2001.

[107] Ingo Meyenburg, Tobias Breuer, Andrea Karthäuser, Sangam Chatterjee, Gregor Witte, and Wolfram Heimbrodt. Temperature-resolved optical spectroscopy of pentacene polymorphs: variation of herringbone angles in single-crystals and interface-controlled thin films. *Physical chemistry chemical physics : PCCP*, 18(5):3825–31, 2016.

[108] Alexander Hinderhofer, Ute Heinemeyer, Alexander Gerlach, Stefan Kowarik, Robert M J Jacobs, Youichi Sakamoto, Toshiyasu Suzuki, and Frank Schreiber. Optical properties of pentacene and perfluoropentacene thin films. *The Journal of Chemical Physics*, 127(19):194705, 2007.

[109] Tobias Breuer and Gregor Witte. Epitaxial growth of perfluoropentacene films with predefined molecular orientation: A route for single-crystal optical studies. *Physical Review B*, 83(15):155428, 2011.

[110] Linjun Wang, Yoann Olivier, Oleg V. Prezhdo, and David Beljonne. Maximizing singlet fission by intermolecular packing. *Journal of Physical Chemistry Letters*, 5(19):3345–3353, 2014.

[111] F Anger, J. O. Oss, U Heinemeyer, K Broch, R Scholz, A Gerlach, and F. Schreiber. Photoluminescence spectroscopy of pure pentacene, perfluoropentacene, and mixed thin films. *Journal of Chemical Physics*, 136(5):054701, 2012.

[112] Tobias Breuer and Gregor Witte. Thermally activated intermixture in pentacene-perfluoropentacene heterostructures. *Journal of Chemical Physics*, 138:114901, 2013.

[113] Rui He, X. Chi, Aron Pinczuk, D. V. Lang, and A. P. Ramirez. Extrinsic optical recombination in pentacene single crystals: Evidence of gap states. *Applied Physics Letters*, 87(21):211117, 2005.

[114] Steffen Duhm, Ingo Salzmann, Georg Heimel, Martin Oehzelt, Anja Haase, Robert L Johnson, Jürgen P. Rabe, and Norbert Koch. Controlling energy level offsets in organic/organic heterostructures using intramolecular polar bonds. *Applied Physics Letters*, 94(3):033304, 2009.

[115] J. Burgos, M Pope, Ch. E. Swenberg, and R. R. Alfano. Heterofission in pentacene-doped tetracene single crystals. *Physica Status Solidi (b)*, 83(1):249–256, 1977.

[116] Xiuhui Zhang, Qian-Shu Li, Yaoming Xie, and Henry F. Schaefer. The lowest triplet electronic states of polyacenes and perfluoropolyacenes. *Molecular Physics*, 105(19-22):2743–2752, 2007.

Abstract

Perylene microcrystals have been grown by continuous resublimation of a perylene layer originally grown by organic molecular beam deposition. Under the correct growth condition, virtually defect free single-crystalline platelets of both the α-and β-phase with molecular smooth surfaces were achievable. Both polymorphs are easily distinguishable by their characteristic rhombic and rectangular shape and their distinct emission spectra, appearing orange and green to the eye for the α-and β-phase, respectively. Their diameter of up to 100 μm allows for high-resolution polarization-resolved optical spectroscopy, directly linking the crystalline axis to the anisotropic optical response of each crystalline phase. To this end, we addressed the in plane crystalline b and c-axis of both species in absorption spectroscopy at cryogenic temperature. We obtained information on the excitonic system with unprecedented accuracy. This enables a comprehensive comparison of the experimental spectra and state of the art *ab initio* calculations. Indications for a polaritonic stopband where found by analyzing the differences between both spectra. The calculated electronic bandstructure and excitonic wavefunction could be correlated to the measured emission lifetimes of both perylene polymorphs: Strong dispersion and spatial delocalization translate to shorter PL lifetimes. The more localized wavefunction of the α-phase could be linked to the strong intermolecular interaction of the perylene dimers that make up the crystal. PEN-PFP heterostructures with different molecular alignment at the heterointerface where grown exploiting templating effects mediated by the substrat and the previously deposited layer: one intermixed 1:1 molecular blend and two layered heterostructures with edge-on and face-on molecular alignment at the interface. Comparing the optical properties of those samples with the corresponding unitary films revealed the interface specific response of the system. We could show that the interface does not influence the emission spectra and dynamics of the constituent layers not directly at the interface.

However, completely new interface related emission signal where observed at lower energies, displaying long lifetimes when compared to the free excitonic emission observed from the unitary materials. We assign those emission lines to CT-excitons. They form with great efficiency in the intermixed heterostructure, completely replacing any signal of the unitary molecules at low temperatures. In the heterostacks, a strong increase of CT-emission was observable for face-on stacking on the interface, which is linked to an increase in intermolecular interaction across the interafce due to π-π stacking between PEN and PFP molecules. Previous studies, especially on the frontier orbitals of the constituting molecules at the interface, reveals significant deviation from the commonly discussed discription of CT-excitons.

To gain additional insight into the formation pathways of those CT-states, PLE spectra of the heterostructures where compared with their respective absorption spectra. The differences observed in both spectra reveal absorption channels which do not relax into the CT-subsystem. While all excitons excited in the PEN layer and directly into the CT-state contribute to CT-emission, any excitation into the PFP layer does not. This further raises questions about the exact nature of the CT state, as a simple relaxation scheme based on the frontier orbitals of all involved states does not hold up to the experiments.

Zusammenfassung (Abstract in German)

Perylene Microkristallite wurden durch wiederholtes Resublimieren aus einer per organischer Molekülarstrahlepitaxy erzeugten Perylenschicht gewachsen. Unter den richtigen Wachstumsparametern konnten somit nahezu defektfreie Einkristalle beider kristalliner Phasen, der dimerischen α-Phase und der monomerischen β-Phase, mit molekular glatter Oberfläche gewonnen werden. Diese ließen sich durch ihre characteristische rechteckige beziehungsweise rombische Form und ihre ausgeprägten Emissionsspektren unterscheiden, wobei die Luminescence der α-Phase orange und die der β-Phase grün erscheint. Ihr Durchmesser von bis zu einigen 100 μm ermöglichte polarisationsaufgelöste optische Spektroskopy mit hoher Qualität, wodurch die Kristallinen Achsen direkt mit der anisotropischen optischen Antwort der Kristalle korreliert werden konnte. Zu diesem Zwecke wurden Absorptionsspektren polarisiert entlang beider addresierbaren Kristallinen Achsen bei cryogenen Temperaturen gemessen. Dabei wurden Informationen über das exzitonische System beider Kristalle mit vorher unerreichter Präzision gewonnen. Diese konnten für einen ausführlichen Theorievergleich basierend auf *ab initio* DFT-BSE Rechnungen verwended werden. Dabei wurde eine sehr gute Übereinstimmung beobachtet. Die einzigen signifikanten Abweichungen weisen auf die Existenz eines Polaritonischen Stopbandes hin. Darüber hinaus konnte ein Zusammenhang zwischen der berechneten Bandstruktur und exzitonische Wellenfunktion und der Lebensdauer der gemessenen Photolumineszenz hergestellt werden: Dispersivere Bänder und ein höheres Maß an Delokalisation führen zu kürzeren PL Lebensdauern in der β-Phase, wärend die stärkere Lokalisation in der α-Phase im Zusammenhang mit seiner dimerischen Struktur zu stehen scheint.

PEN-PFP Heterostrukturen mit unterschiedlicher molekülarer Ausrichtung an der internen Grenzfläche wurden gewachsen: Eine 1:1 durchmischte Probe und zwei gestapelte Proben, jeweils mit paraleller und senkrechter Ausrichtung der Moleküle zur Grenzfläche. Die Emissionsspektren dieser Systeme wurde mit den Spektren iherer jeweiligen Bestandteile verglichen, um den Einfluß der Grenzfläche selbst zu bestimmen. Es konnte gezeigt werden, dass die Grenzfläche lediglich einen kurzreichweitigen Einfluß auf die optischen Eigenschaften der Heterostrukturen hat. Es konnten jedoch neue Grenzflächen PL gemessen werden, die wir CT-Exzitonen zuschreiben. Diese verdrängen in der durchmischten Probe bei niedrigen Temperaturen alle Signale die dem reinen PEN und PFP zugeordnet werden können. In den gestapelten Strukturen konnte eine starke Zunahme der CT-Emission für die Probe mit paraleller Ausrichtung der Moleküle zur Grenzfläche festgestellt werden, die wir einer Erhöhung der intermolekularen Wechselwirckung durch π-π Stapellung zuschreiben. Ein Abgleich mit der vorhandenen Literatur, besonders über energetische Position der HOMO und LUMO beider Materialien an der Grenzfläche, zeigt deutliche Abweichungen vom vorherschenden Bild eines CT-Exzitons.
Um weitere Einsicht in die Formationsmechanismen des CT-Exzitons zu Erlangen wurden die Absorptionsspektren der oben genannten Heterostrukturen mit den zugehörigen PLE-Spektren verglichen. Unterschiede zwischen beiden zeigen die Absorptionskanäle auf, die nicht an das CT-Exziton koppeln. Es stellte sich heraus, das jede direkte Anregung des CT-Exzitons und Anregung in die PEN schicht zur CT-Emission beitragen, nicht aber Anregung in die PFP Schicht. Dies steht ebenfalls im Gegensatz zur üblichen Theory der CT-Exzitonen.

Scientific Curriculum Vitae

07/2007	Highschool Diploma at the 'Herderschule Gießen'.
10/2008-12/2013	Student at the 'Philipps-Universität Marburg' in physics.
08/2011	Bachelor Degree under Prof. Dr. Macillo Kira. Title of the thesis: Excitonic effects in Microcavities.
08/2012-12/2012	Semester at the university of Gothenburg.
12/2013	Master degree under Prof. Dr. Sangam Chatterjee. Title of the thesis: Excitonic and Excimeric Features in Monomeric and Dimeric Perylene Crystals.
01/2014-06/2017	PhD student and scientist at the 'Philipps-Universität Marburg' in the group of Prof. Dr. Sangam Chatterjee.

Wissenschaftlicher Lebenslauf

07/2007	Abitur an der Herderschule Gießen.
10/2008-12/2013	Studium der Physik an der Philipps-Universität Marburg.
08/2011	Abschluß zum B. Sc. in Physik unter Prof. Dr. Macillo Kira. Titel der Bachelorarbeit: Excitonic effects in Microcavities.
08/2012-12/2012	Auslandssemester an der Universität Göteborg.
12/2013	Abschluß zum M. Sc. in Physik unter Prof. Dr. Sangam Chatterjee. Titel der Masterarbeit: Excitonic and Excimeric Features in Monomeric and Dimeric Perylene Crystals.
01/2014-06/2017	Doktorand und wissenschaftlicher Mitarbeiter an der Philipps-Universität Marburg in der Arbeitsgruppe von Prof. Dr. Sangam Chatterjee.

Acknowledgements

All cheesy clichés hold a portion of truth, so does the post-thesis acknowledgment: I could not have done it alone. My sincere gratitude goes out to everyone who supported me during the last four years of my life, inside and outside the lab.
The former category has to be headed by my adviser, Sangam Chatterjee, for creating the best working environment I will most likely ever work in. His open door policy made my transition from the computer to the lab very easy and helped me grow tremendously as a scientist and as a person. The only person who taught me more about the in and outs of the lab and optical spectroscopy was Kolja Kolata, who supervised me during my master thesis. We will always have the nights together in the lab. Speaking about the lab, we head on to my 'partners in crime': Robin Döring, Nils Roseman and Florian Dobener. You all made the daily ups and downs bearable, Robin by his incredible friendliness, humor and fake temper tantrums, Florian by proving we can all surpass our past and falling from things in a funny way and Nils by simply being the most amazing person in the universe. You all helped me out with issues inside and outside university, and for that I will be forever thankful. To all the undergraduates I worked with through the years: it has been your pleasure to work for me.
Science is never something a spectroscopy group can do alone. I want to thank Michael Oestreich and Julia Wiegand for their contribution to my scientific work. However, when it comes to creating and writing down scientific content, my biggest thanks go out to Gregor Witte and Tobias Breuer. I always value the easy communication pathways, incredibly fast sample design on demand with exceptional quality and fruitful discussions. If not for you and what you taught me about scientific writing, this thesis would be a lot more unreadable than it already is.
Now for the people who actually work: a big thank you to everyone in the mechanical and electronic workshop and technical staff of the faculty, especially Rainer Täubner

and Peter Osswald. When inexperienced hands try to experiment, thinks break and they break often and yours was the job of picking up the shards and keep the show running. A special place in my heart will always be reserved for the crew at the Klingelhöfer bakery in the Oberstadt, providing me with cake of glory when things went well and consoling cake of shame when they did not.
But life is more than work and science. My family, especially my parents and grandparents deserve my eternal gratitude. I would not be there without you and you would have less gray hair without me. Thank you for always being there. Thank you Jörg Matzner and everyone I shared the mat with over the last years. And off course, honor and glory to the GCS, we had great years and will have better ones. Shall the cards fall always in our favor.
But no one deserves more gratitude than the most important person in my life. In eternal love and respect I want to thank my wife for her unwavering support and for every minute, even the turbulent ones, we spent and will spend together.